Master Thesis, Department of Geosciences

Sedimentology, petrology, and diagenesis of core 16/1-13 from the Edvard Grieg Field, Utsira High, Norwegian North Sea

Emilie Asbjørnsen

UNIVERSITY OF OSLO

FACULTY OF MATHEMATICS AND NATURAL SCIENCES

Sedimentology, petrology, and diagenesis of core 16/1-13 from the Edvard Grieg Field, Utsira High, Norwegian North Sea

Emilie Asbjørnsen

Master Thesis in Geosciences

Discipline: Petroleum geology and Petroleum geophysics

Department of Geosciences

Faculty of Mathematics and Natural Sciences

University of Oslo

1 st June

Tutor(s): Henning Dypvik, (UiO) Orhan Mahmic (UiO) and Erik Hammer (Lundin Norway)

This work is published digitally through DUO – Digitale Utgivelser ved UiO

http://www.duo.uio.no

It is also catalogued in BIBSYS (http://www.bibsys.no/english)

Acknowledgment

First I would like to thank my supervisor Henning Dypvik at the Department of Geoscience at the University of Oslo. Thank you for always being supportive and available for questions and discussions. You have been a great inspiration for many years now. Thank you for giving me a chance to be part of this, your helpful guidance, support, and understanding throughout this past year.

I would also thank my co-supervisor and PhD student, Orhan Mahmic, who have helped me and supported me throughout the year, and always being available for questions and discussions. Thanks are also needed for PhD students Lars Riber and Katrine Fossum, for helpful guidance during my thesis.

I would also like to express my gratitude to Lundin Norway for their financial support during this project. Thanks to Erik Hammer and Ronald Sørlie for great assistance and helpful guidance during the logging at Weatherford Laboratories.

Thanks to Berit Løken Berg, for assisting me during SEM analysis, and Muriel Erambert for assisting during electron microprobe analysis. A big thanks is given to Maarten Aerts for running my XRD and very helpful guidance during the interpretation. Salahalladin Akhavan at UiO and Lars Kirksæther at IFE Petrosec need a thank you for excellent preparation work for my thin sections. Thanks to John Andrew Knell-Brew for proofreading my thesis.

To my supporting and loving family, who have helped and encouraged me throughout my academic years. Thank you for always being supportive. I want to express my gratitude to my beloved Magnus, who has put out with me being stressed about my master thesis. Your support and encouragement have been much appreciated throughout the past year. You always help me believe in myself, and encourage me to continue and don't give up. Thank you for your love and patience.

I would also like to thank my fellow students for helpful discussions and fun times throughout the year. Lunch breaks have been highly appreciated.

Abstract

Sedimentary successions of Permo-Triassic to Early Cretaceous age have been studied in core 16/1-13 from the Edvard Grieg Field, located on the Utsira High, in the North Sea. Sedimentary field data combined with petrographical and mineralogical studies (XRD, thin sections, SEM and EMP) have been used to interpret the depositional environment and to gain knowledge about the diagenetic history of the sediments. The results obtained from this master thesis, will provide information about the properties of the sediments, and can be used in later work on the porosity and permeability history in the Edvard Grieg Field. It is important to point out that the results obtained in this master thesis, only derive from the study of one core, and that the results are derived from the data obtained during this half-year thesis. Further studies, from the same core and adjacent cores, should be conducted for a quality check of the results found during this study.

The studied section, core 16/1-13 consists of sediments from the Permo-Triassic and the Early Cretaceous, displaying depositional environments within different alluvial and marine regimes. An alluvial fan and an aeolian depositional environment represent the Permo-Triassic sedimentary succession, while marine carbonates represent the sediments deriving from the Early Cretaceous. Emphasis has been on the sediments of Permo-Triassic age, where the diagenetic history contains several phases of authigenic clay mineral formation, Fe-oxide precipitation, authigenic overgrowths and the precipitation of carbonate cement. The sediments from the alluvial fan and the aeolian regimes are found to carry similar diagenetic histories.

The alluvial fan section contains debris flow successions, represented by conglomerates, displaying eroded basement clasts and matrixes originating from reworked paleo-weathering profiles located on the Utsira High. The study reveals that the basement clasts have experienced both sub-aerial weathering and alteration connected to diagenesis. The clay minerals present in the conglomeratic matrixes, are all found to have a diagenetic origin, deriving from the alteration and degradation of feldspars and micas during burial (neoformation), or from recrystallization of detrital clay (regeneration). Multiple layers of clay coating and pore filling clays are found. Differences in degree of weathering and original mineralogy of basement clasts, together with varying alteration of feldspars, points to at least

two provenance areas for the alluvial fan sediments. The sediments from the alluvial fan, are in thin section, found to display relatively low porosity values.

The aeolian sediments display higher porosities, compared to the alluvial fan sediments, but the aeolian sandstones are found to have a higher content of authigenic kaolinite and sparitic carbonate cement. These authigenic minerals are found to reduce the porosities, especially in the medium grained sandstones.

The study reveals that the sediments of core 16/1-13, have been affected by early diagenetic processes related to the sedimentary facies in alluvial environments. The diagenetic influence has to some extent reduced the porosity, and may have influenced the present day reservoir quality. The sediments from the aeolian regime are found to have the highest porosity values, giving these sandstones good reservoir quality.

Table of Contents

1. Introduction

1.1 Purpose of the study and project description

This master thesis is based on sedimentological and petrographical analysis of Permo-Triassic and Early Cretaceous sedimentary strata from the Edvard Grieg Field located on the Utsira High, Norwegian North Sea. The data for this master thesis derive from well 16/1-13, which is owned and operated by Lundin Norway (50%), in corporation with OMV AS (20%), Statoil Petroleum AS (15%) and Wintershall Norge AS (15%) (NPD, 2015 a). In this master thesis the aim will be to create and analyse sedimentary logs and mineralogical data (thin sections, XRD, EMP and SEM). Based on this, the thesis will give a description of the sedimentary succession, and there will be a discussion of the depositional environment and the diagenetic history of core 16/1-13.

This thesis is part of a four year (2014-2018) joint project between the University of Oslo, FEI Trondheim (Lithicon Norway) and Lundin Norway. The goal of the project is to analyse (sedimentological logging and sedimentpetrographical investigations) sedimentary cores from the reservoir of the Edvard Grieg Field. The focus will be on the lithofacies variations of the core, and to reconstruct the related geological evolution. With regards to the facies variations, emphasis will be on the porosity evolution with time and space. The project is aiming at improving our understanding of the petroleum system at the Edvard Grieg Field, and to hopefully increase the success rate of the field.

1.1.1 Study area

Being part of the northwest European continental shelf, the North Sea region has experienced a complex and varied geological evolution. The area has experienced different tectonic regimes, ranging from compressional to extensional tectonics, resulting in orogeny events, faulting, crustal extension and thermal subsidence. These different tectonic events have created structures and features that reflect the different stages of structural development through the geological history of the North Sea. The most prominent features are the graben structures; the Viking Graben to the north, the Moray Firth Basin to the west and the Central Graben to the south (Figure 1.1). Together they represent the North Sea failed rift system, created during the extensional tectonics occurring in the Permian-Triassic transition and Middle to Late Jurassic (Ziegler, 1992).

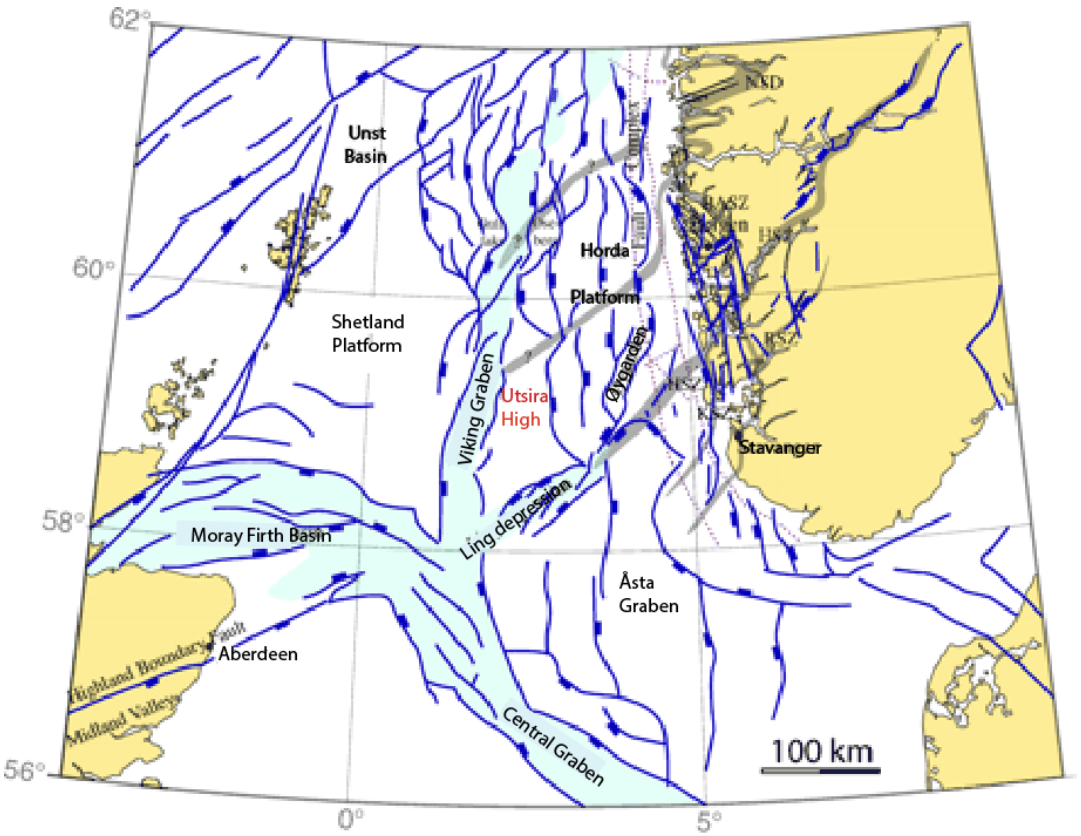

Figure 1.1: A regional map of the North Sea, showing the main fault trends and the main graben structures. The Utsira High is highlighted in red, and is located between approximately 60-58°N. Modified from Fossen and Hurich, 2005.

The Utsira High is located in the Norwegian North Sea region (Figure 1.2). Utsira High is a large basement high, which is flanked by the Viking Graben to the west, the Ling Depression to the south, and the Stord Basin to the east (Figure 1.3) (Isaksen and Ledje, 2001). The structural configuration found on the Utsira High at present time, is the result of extensional tectonics occurring in the Late Paleozoic and Mesozoic (Isaksen and Ledje, 2001).

The Edvard Grieg Field (formerly known as the Luno Field) is located in a small graben in the southern part of the Utsira High, known as the Haugaland High (Figure 1.2). The field is part of licence PL338, and is located approximately 45 km south of the Grane – and Balder Fields, and 180 km west of the city of Stavanger (Lundin Norway, 2015).

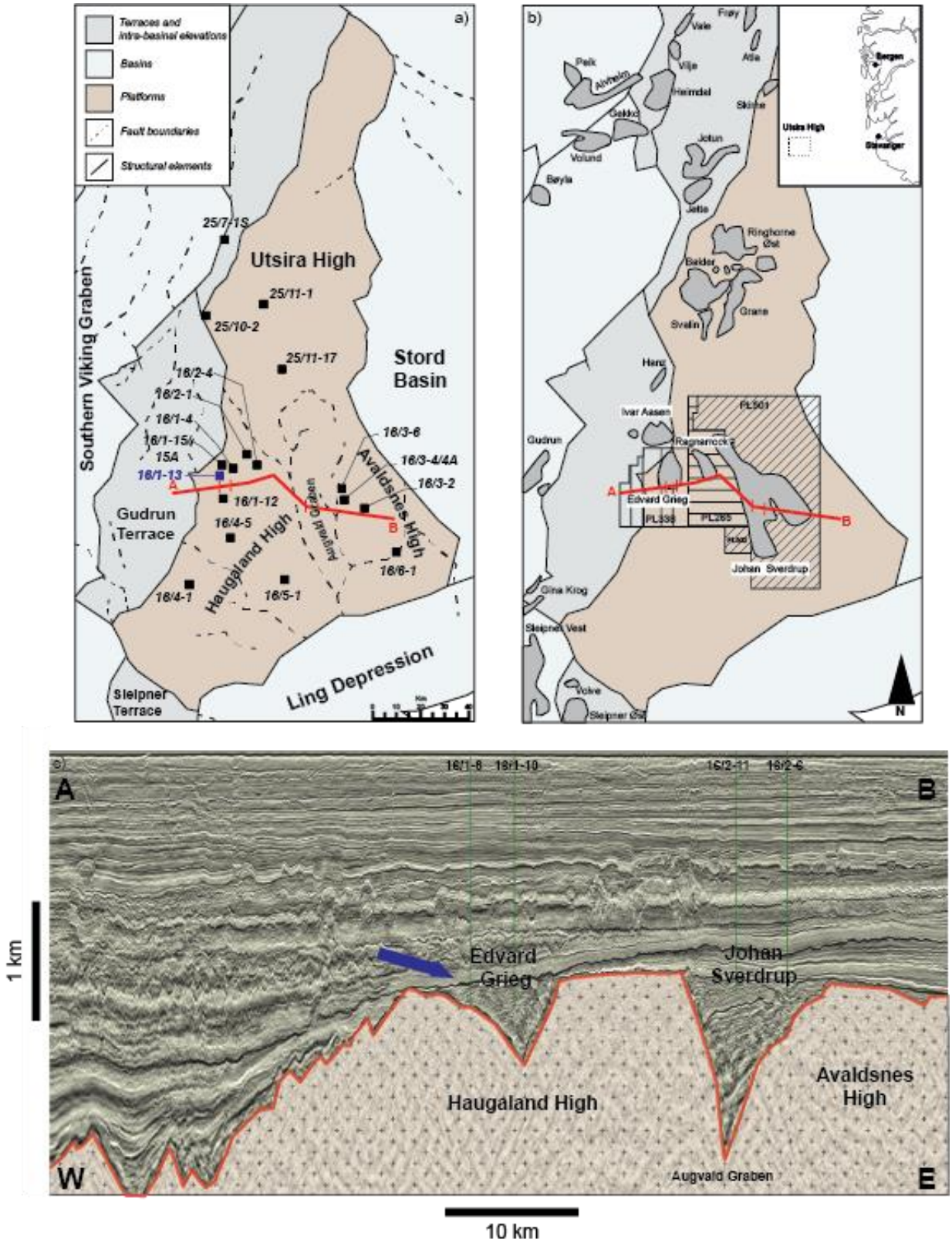

Figure 1.2: Figure a) shows the location of the wells drilled on the Utsira High, well 16/1-13 is highlighted with blue. Figure b) shows the location of the fields located on the Utsira High. The Edvard Grieg Field lies in license PL338. Figures a) and b) are modified from Riber et al. (in prep.). The cross section marked in a and b, are shown as a seismic profile in Figure c). The blue arrow points to the approximately position of well 16/1-13. The seismic section is provided by Lundin Norway.

1.1.2 Previous studies

The southern part of the Utsira High has not been studied in great detail since the 70's and until 2007. Then the area became of interest, when Lundin Norway found oil in well 16/1-8, and confirmed the presence of petroleum in the area (Riber et al., in prep.). The petroleum was discovered in weathered basement rocks, which has never been observed before on the Norwegian continental shelf. Early exploration, before 2007, on the southern part of the Utsira High, revealed minor oil and gas findings, but the discoveries were decided to be non-commercial, and no further interest was shown in the area. It was not until the discovery of the Edvard Grieg Field in 2007, that the interest for the southern part of the Utsira High increased, and the discovery itself led to increased understanding of the geological setting in this area. After the Edvard Grieg discovery, additional five more discoveries (Apollo, Tellus, Luno South, Luno II and Johan Sverdrup) have been found in the area by Lundin Norway (Lundin Norway, 2015).

At present time there are several projects and studies conducted in the southern part of the Utsira High, where the main goal is to understand the weathering of basement rocks and the variation in porosity and permeability in time and space. PhD student Lars Riber, at the University of Oslo, studies sediment and basement cores in order to determine the degree of weathering, relating this to weathering profiles found at other localities around the world and to increase knowledge about palaeoclimate and migration. PhD student Orhan Mahmic, at the University of Oslo, will further study cores from the Edvard Grieg Field, and try to model porosity and permeability in the area in both time and space. These two projects will certainly increase the knowledge about weathering profiles and reservoir differences in time and space, results which will increase the knowledge about relevant petroleum systems. Selvikvåg (2012) wrote a master thesis in cooperation with Lundin Norway, about the Luno Conglomerate Member of the Skagerrak Formation. Her main focus was on sedimentology and facies analyses.

1.2 Regional geology

1.2.1 Tectonostratigraphic development

The tectonic framework of the North Sea area was highly developed during the Caledonian to the Variscan tectonic events. The accretion of earlier deposited continental fragments and newer magmatic arcs onto the Laurentian-North Atlantic craton had a major influence (Zanella and Coward, 2003). In the Early Ordovician, the Iapetus Ocean began to close due to subduction along both margins, initiating the development of the Caledonian orogeny; the

result of the collision between the Laurentia and Baltica continents (Gee et al., 2008). The collision between the two continents started in the Mid Silurian to Early Devonian and was dominated by several hundred kilometres of south-easterly directed thin-skinned overthrusting (Coward et al., 2003). The orogeny is known for its well-developed thrust system, and the mountain chain had a width of at least 700-800 km, prior to the opening of the Atlantic Ocean in the Cenozoic (Gee et al., 2008).

Early in the Devonian, the mountain chain was at its most impressive, but the closure of the Iapetus Ocean led to a shift, from compressional to extensional tectonic regime. This shift resulted in the Early Devonian collapse of the orogeny. Tectonic thinning, exhumation, and denudation of the Caledonian orogeny were rapid during the Devonian (Gee et al., 2008), leading to a change from a very deep-rooted crust to a more normal crustal thickness. This resulted in a low relief desert like landscape towards the end of the Carboniferous (Gee et al., 2008).

During the Devonian, grabens could be found both onshore and offshore southern Norway, and a large, possible Devonian, basin developed in the northern North Sea. The evolution of the basin was a combination of gravitational collapse of thickened crust (McClay et al., 1986), and pull-apart development (Coward et al., 2003). The pull-apart basin found in the northern North Sea was deep, and formed a proto-Viking Graben structure. The basin likely carried the initiation of faults and sub-basins that were later reactivated during the Mesozoic (Coward, 1993).

The North Sea region drifted northwards from 20°S to 15°S during the Devonian, and the sedimentation at this time, took place in a hot, arid and continental setting (Downie, 1998). The sediments deposited during this time period are today known as the Old Red Sandstone, and are present on the British Isles and in basins in western Norway. Well data from the North Sea area has not yet confirmed a continuous belt of the Old Red Sandstone across the North Sea (Downie, 1998). Færseth (1996) has proposed that the Utsira High, at this time, were exposed to extensive erosion.

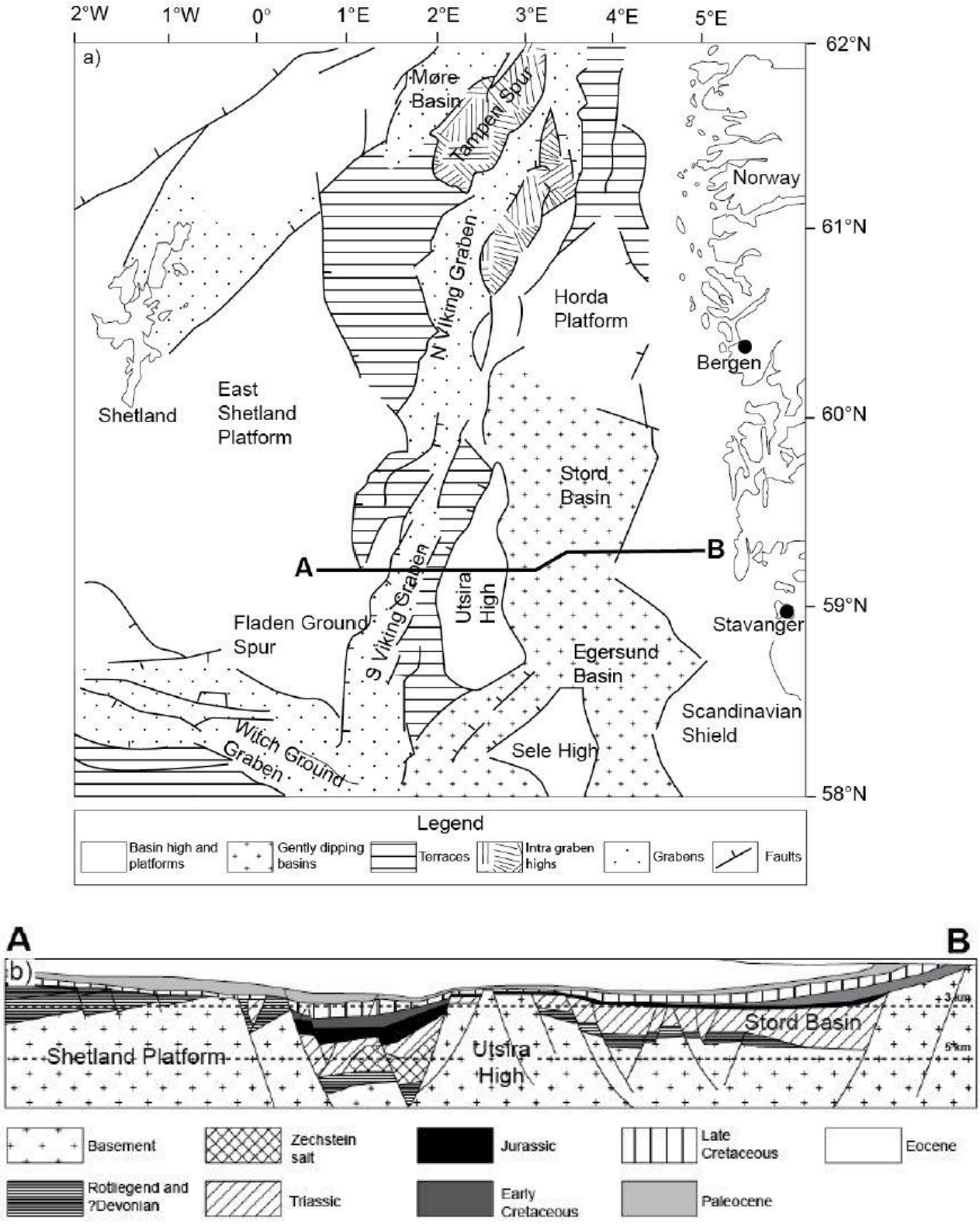

Figure 1.3: a) A regional map showing the location of the Utsira High and the structural elements found in the North Sea area (modified from Gregersen, 1997). The cross section A-B is marked. b) Cross section (A-B) of the southern Viking Graben, crossing the Utsira High (modified from Ziegler, 1992). The Figures are modified by Riber et al. (in prep.).

The North Sea area continued to drift northwards during the Devonian, and by Early Carboniferous the area had drifted into equatorial latitudes, and the climate changed from arid to more warm and humid conditions (Glennie and Underhill, 1998). During the Early Carboniferous, the proto-Viking Graben system was reactivated. Faults of Devonian and Early Carboniferous age experienced a reversal of their displacement, leading to tectonic inversion across north-western Europe (Coward, 1993). During the Carboniferous, Baltica and Laurentia (Laurussia) drifted slowly northwards. Further south, the continent of Gondwana also drifted northwards, at a higher speed than Laurussia. In the Late Visean, the final closure of the Rheic Ocean occurred, leading to the collision of Laurussia and Gondwana, resulting in the Variscan Orogeny. At this time, the supercontinent Pangea was forming (Glennie and Underhill, 1998).

A change in the climate occurred from the Carboniferous to the Permian. Due to the northward drift of Laurasia, the climate changed from humid equatorial conditions in Carboniferous to arid climate in the Permian (Glennie, 1998). At this time, the North Sea region was located at a latitude position north of the equator, similar to present day North African and Arabian deserts, at about 20-30°N (Glennie, 1998).

In the North Sea region, Rotliegend sands were filling in the topography created during the Late Carboniferous to Early Permian inversion (Zanella and Coward, 2003). The Permian basins were the site of rapid subsidence (Glennie, 1998), and the accumulating Rotliegend sandstone consisted of fluvial (wadi), aeolian, sabkha, and lacustrine facies, indicating that the area experienced a desert climate (Brekke et al., 2001). During the following phase of thermal subsidence, the sandstone continued to fill up the basins (Zanella and Coward, 2003).

The Late Permian suffered a glacio-eustatic rise in sea level, reflecting the melting of Permo-Carboniferous ice on Gondwana. At the same time, rifting in the Faeroe-East Greenland and in the northern North Sea regions, opened a seaway from the southern North Sea to the Arctic Ocean. The resulting marine transgression from the north led to the deposition of the Zechstein Sea, which covered much of the northern and central Europe (Coward et al., 2003). The transgression resulted in deposition of 2-3 km of Zechstein Group sediments, which includes shales, carbonates, and evaporites of the Permian basins (Ziegler, 1992) (Figure 1.4).

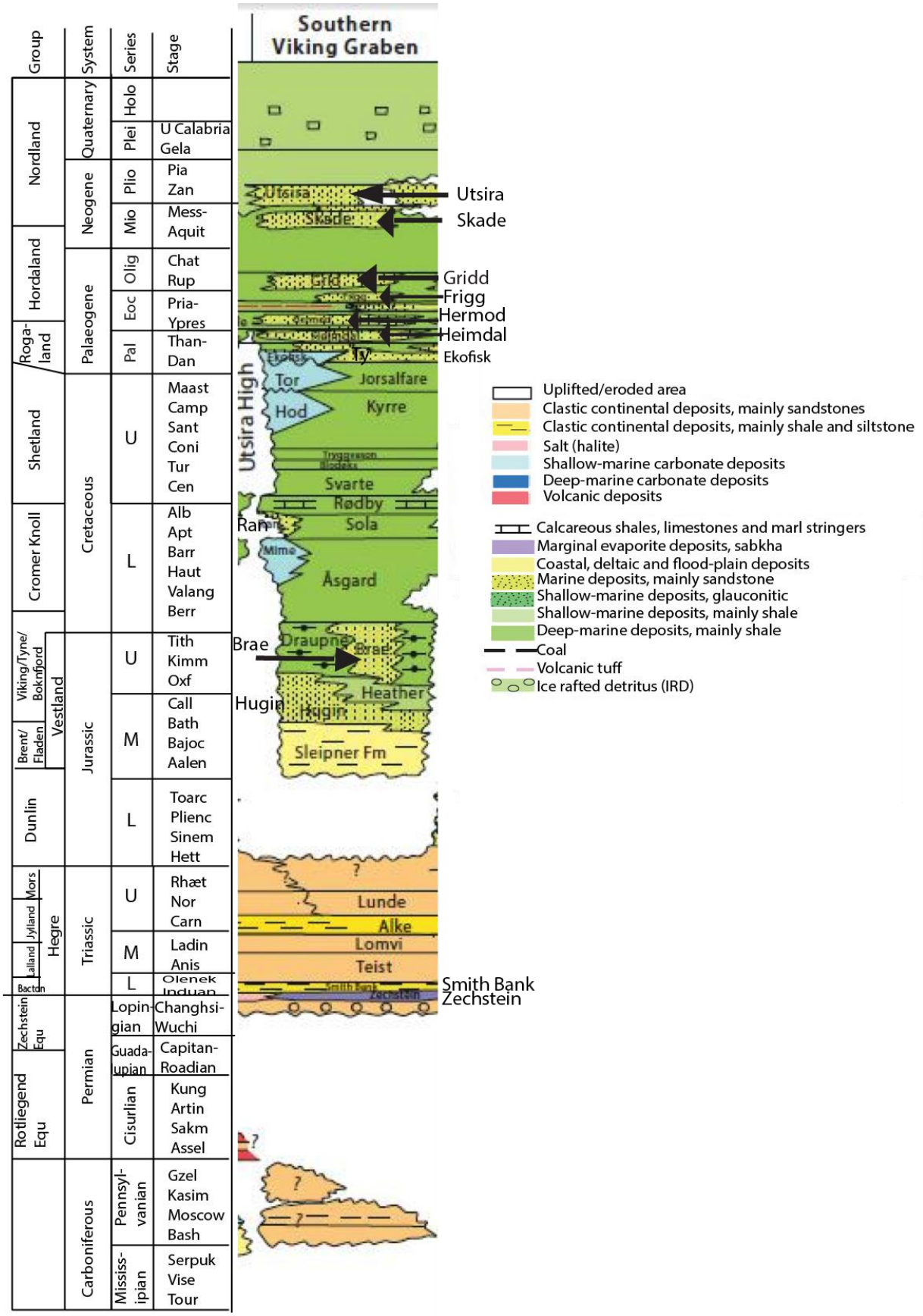

Figure 1.4: A lithostratigraphic column of the southern Viking Graben. (Modified from NPD, 2015 b).

At the transition from the Permian to the Triassic, the North Sea experienced extension. According to Ziegler (1992), the Late Permian-Early Triassic rift phase in the North Sea region was a consequence of the Norwegian-Greenland Sea rift propagating into the North Sea area. This rift phase is also considered as the first rift phase in the North Sea. The tectonics developing at the transition from the Permian to the Triassic, were part of a larger rift system covering the entire northern North Sea, reflecting the break-up of Pangea (Ziegler, 1992; Brekke et al., 2001). The tectonic activity enhanced the development of the graben structures located in the North Sea, consisting of the Viking Graben, the Moray Firth Basin and the Central Graben (Spencer and Larsen, 1990) (Figure 1.1). The Viking Graben, created by the extensional tectonics, cross-cut Caledonian structural elements, as well as the axes of the pre-rift sedimentary basins developing through the Devonian, the Carboniferous and the Permian times (Ziegler, 1992). The first rift event had a dominantly north-south orientation, but due to the interaction with Palaeozoic sediments and structural elements, multidirectional basins were created in the northern North Sea (Fisher and Mudge, 1998).

In the Early Mesozoic, the Zechstein Sea regressed and there was a return to continental deposition conditions in the North Sea area (Fisher and Mudge, 1998; Nøttvedt et al., 2008; McKie and Williams, 2009; Nystuen et al., 2014). As a result of the first rifting event (Late Permian-Early Triassic), the depositional environments now became restricted to a major basin (the Viking Graben) along the present coast of Norway (Lervik, 2006), which are unlike the Late Permian basins in the same area; being wider and with no restrictions for the depositional environments. The Permian salt deposition was followed by silicate clastic sedimentation, derived from the Fennoscandian Shield, the Scottish Highlands and Greenland (Lervik, 2006; McKie and Williams, 2009) (Figure 1.4). Throughout the entire North Sea region, Triassic sediments are dominantly red beds, due to the sub-aerial oxidation of iron; several continental facies are represented. There are observations of Triassic alluvial fans, fluvial, lacustrine, aeolian, and flood basin facies in the area. The conditions were not equal throughout all the basins in the North Sea, and variations in the dominating facies have been observed (Fisher and Mudge, 1998; Goldsmith et al., 2003). The change in plate position (from 20° to 50° N (Doré, 1991)) during the Triassic, linked with the northwards drift of Eurasia, gave rise to a gradual change in climate from arid/semi-arid to humid in the North Sea region (Goldsmith et al., 2003; Nystuen et al., 2014).

After the Early Triassic period of active rifting, the northern North Sea area continued to

subside, a result of thermal subsidence. This period lasted until the Bathonian (168 Ma), and was followed by a new period of active rifting (Badley et al., 1988).

In Early Jurassic, the North Sea was flooded, due to a narrow connection between the northern Boreal Sea and the southern Tethys Ocean. The connection was the result of a rise in sea level in the North Atlantic region (Nøttvedt et al., 2008). The developing transgression is mirrored in the deposition of marine sandstones and shales, making up the Dunlin Group (Figure 1.4), which are still preserved in the western part of the Viking Graben and on the northern part of the Utsira High (Vollset and Doré, 1984).

During the Early Jurassic, the development of the Mid-North Sea Dome, led to uplift and erosion of the southern Viking Graben (Ziegler, 1992), creating the Mid-Cimmerian Unconformity. As a consequence, no sediments from the Early Jurassic have been found on the southern part of the Utsira High, marked by the unconformity, separating Triassic and overlying Middle Jurassic strata (Jackson et al., 2010) (Figure 1.4).

In the Middle Jurassic, Baltica had further drifted to between 45° and 60°N, but in the Late Jurassic there was a change in pole of rotation, leading to a rotation of Baltica southwards, giving it a location between 40° and 55°N. The climate at this time in the North Sea was warm and humid (Nøttvedt et al., 2008).

The second North Sea rift phase, initiated in the late Middle Jurassic (Bathonian), and the rifting intensified in the Late Jurassic (Callovian to Early Kimmeridgian) (Coward et al., 2003; Nøttvedt et al., 2008). This rift event is responsible for the main structural setting in the Viking Graben, and the rift event would eventually cause the break-up of the central Atlantic (Brekke et al., 2001). In the Late Jurassic, Artic rifting propagated into the North Sea and formed north to north-easterly trending normal faults in the Viking Graben (Coward et al., 2003) (Figure 1.1). The rifting resulted in deeper subsidence, and was localized in a narrower zone than the Permo-Triassic rift event. Mid- and the Late Jurassic rifting thinned the crust, resulting in subsidence of the rift below sea level (Nøttvedt et al., 2008).

In Early Cretaceous, the rifting continued, and normal faults were still active. There was deposition of clastic wedges against the fault scarps (Coward et al., 2003). The second North Sea rift phase ceased during the Early Cretaceous, and the rest of the Cretaceous period in the

North Sea region was dominated by thermal subsidence (Coward et al., 2003; Nøttvedt et al., 2008). The syn-rift topography in the North Sea area, was covered by succeeding transgressive sands (Coward et al., 2003). During the Cretaceous, Baltica continued its northwards drift, towards 50° to 65°N, in the temperate climatic zone (Nøttvedt et al., 2008). During the Cretaceous, there was a continuous global rise in sea level. Lowlands were submerged, and in the Late Cretaceous the sea level was, probably at its highest ever in the North Sea history. At this time more than half the continental landmasses were covered by sea, including large parts of mainland Scandinavia (Nøttvedt et al., 2008). The high sea level and the low topographic relief in the area gave rise to extensive, shallow epicontinental shelf seas (Nøttvedt et al., 2008) (Figure 1.4). Since Early Cretaceous the Utsira High has gradually subsided (Riber et al., in prep.).

In Palaeogene, the North Sea region, was uplifted and eroded both along the western and eastern edges of the North Sea, resulting in the deposition of submarine-fan systems (Zanella and Coward, 2003; Coward et al., 2003) (Figure 1.4). In Eocene and Oligocene times, the North Atlantic Ocean further developed between Greenland and Scotland (Zanella and Coward, 2003). In the North Sea area the opening of the North Atlantic Ocean, together with the closing of the Tethys Ocean to the south-east, highly influenced basin development. The region underwent steady subsidence, and supply of sediments from the uplifted margins, presently seen as massive accumulations of Upper Cenozoic deposits (Coward et al., 2003). The Pliocene sequence in the northern North Sea, reflect the deposition of major Late Pliocene clastic wedges, building out from mainland Norway (Zanella and Coward, 2003). The Neogen is recognized by numerous glaciations, and climatic cooling. Massive amounts of sediments were created during these glaciations, and the sediments were transported from land and supplied out to the shelf areas in the Late Pliocene and Pleistocene times (Brekke et al., 2001).

1.2.2 Lithostratigraphy in the southern Viking Graben

Rotliegend Group: the sediments present in the group, was deposited in Early Permian times, and consist of continental red beds, of aeolian, fluvial, lacustrine and sabkha facies. The lithologies consist of sequences of clay, shales, sandstones and conglomerates. Volcanic tuffs are common in the lower part of the group (Deegan and Scull, 1977) (Figure 1.4).

Zechstein Group: the group was deposited in a marine environment in the Late Permian. The lithologies found in the group, consist of evaporites, and carbonates, with some local clastic rocks (Figure 1.4). The sediments making up the Zechstein Group are widespread over the Norwegian-Danish Basin, but absent on the eastern and northern part of the Utsira High (Deegan and Scull, 1977).

Hegre Group: was deposited in the Triassic, and consists of intervals of interbedded continental sandstones, claystones and shales (Vollset and Doré, 1984) (Figure 1.4). The group represent sediments deposited from the Induan (252 Ma) to the Rhaetian (210 Ma) (Lervik, 2006).

Statfjord Group: was deposited from Rhaetian (210 Ma) to Sinemurian (199 Ma). The group consists of sediments marking the transition from a continental to shallow marine environments. The group consists, in the lower parts, of continental shale interbedded with thin siltstones, sandstones and dolomitic limestones. The middle part of the group consists of sandstones interbedded with shales. The upper part of the group consists of sandstones with the presence of marine fossils and glauconite, suggesting a shallow marine environment (Deegan and Scull, 1977; Vollset and Doré, 1984; Lervik, 2006) (Figure 1.4).

Dunlin Group: consists mainly of dark marine sediments, but marine sandstones can be found at the basin margins. The group was deposited from the Hettangian (201 Ma) to Bajocian (170 Ma) (Vollset and Doré, 1984) (Figure 1.4).

Vestland Group: the lower part of the group consists of sandy deltaic sequences, with shaly and silty layers and coal horizons (Figure 1.4). The upper parts of the group consist of more marine sands with minor shale interbeds. The group appears in the southern Viking Graben, but is thin or absent over structural highs. The sediments were deposited from Bajocaian (170 Ma) to Volgian (145 Ma), or possibly Ryazanian (142 Ma) times (Vollset and Doré, 1984).

Viking Group: consists of marine mudstones, claystones and shales. Locally, sandstones and conglomerates are replacing these sediments (Figure 1.4). The sediments were deposited in a marine environment, mainly below wave base. In the North Sea, the group ranges from Bathonian (168 Ma) to Ryazanian (142 Ma) in age (Vollset and Doré, 1984).

Cromer Knoll Group: was built up of fine-grained marine material with a varying degree of calcareous material. Calcareous claystones, siltstones and marlstone are the dominating lithologies, but there are also layers of limestone and sandstones (Figure 1.4). The group was deposited in the Ryazanian (142 Ma) to Albian/Early Cenomanian (113/100 Ma) in the North Sea, and the depositional environment was low energy open marine (Dalland et al., 1988; Isaksen and Tonstad, 1989).

Shetland Group: consists of chalk facies including limestones, marls and calcareous shales and mudstones (Figure 1.4). There are also silisiclastic facies present, in the form of mudstones and shales. In the North Sea, the group was deposited from Cenomanian (100 Ma) to Danian (66 Ma) times. The sediments were deposited in an open marine environment during a general rise in sea level (Dalland et al., 1988; Isaksen and Tonstad, 1989).

Rogaland Group: the dominating sediments are sandstones interbedded with shales (Figure 1.4). The sediments were deposited in the Paleocene-Early Eocene in the North Sea, and the depositional environment was deep marine, characterized by submarine fans (Dalland et al., 1988; Isaksen and Tonstad, 1989).

Hordaland Group: is built up of marine claystones with minor sandstones (Figure 1.4). The group was deposited in the Eocene to Early Miocene in the North Sea. The sediments were deposited in marine environments, mainly deep water (Dalland et al., 1988; Isaksen and Tonstad, 1989).

Nordland Group: the dominating lithology is marine claystones (Figure 1.4). In the Viking Graben area, the Utsira Formation makes up the lower part of the group. The sediments were deposited in the Middle Miocene to recent. The depositional environment was open marine, with glacial influence (Dalland et al., 1988; Isaksen and Tonstad, 1989).

2. Methodology

2.1 Sedimentological logging

The logging of core 16/1-13 was carried out from 24 to 26 September 2014 and 5 March 2015, at Weatherford Laboratory in Sandnes, under the supervision of Professor Henning Dypvik, Phd-student Lars Riber (UiO), and Erik Hammer from Lundin Norway. During the three days in September, the author and Orhan Mahmic (Phd, UiO) logged approximately 84 m (2001-1917 m core depth). At the 5th of March 2015, the author, Orhan Mahmic, and Professor Henning Dypvik, collected some more samples and performed further studies of the core.

The core was divided into equal sections, measuring one meter in length and had a diameter of 10 cm. The logging was executed on the B-cut section of the core (Figure 2.1 display example of core and Figure 2.2 for location of B-cut). The core cuts were sprayed with water to get a clearer image, before they were studied closely with a hand lens. The entire core was logged on logging sheets, in the scale of 1:20. The core was logged from the deepest section and upwards, following the geological evolution in time. The Wentworth (1922) grain size classes were used during logging (Table 2.1).

Figure 2.1: The photo shows the B-cut of core 16/1-13. The section shows sediments from 1967-1970 m.

Table 2.1: The table shows the classification of grain sizes according to Wentworth (1922).

Wentworth size class	Phi (φ) units	Size in mm
Boulder	- 8	> 256 mm
Cobble	- 6	64-256 mm
Pebble	- 4	4-64 mm
Granule	- 2	2-4 mm
Very coarse sand	- 1	1-2 mm
Coarse sand	0	0.5-1 mm
Medium sand	1	0.25-0.5 mm
Fine sand	2	0.125-0.25 mm
Very fine sand	3	0.063-0.125 mm
Silt	4	0.004-0.063 mm
Clay	8	< 0.004 mm

In addition to the core logging, samples were taken at chosen locations on the core and photos were taken of the entire core.

Sampling

During the four days at Weatherfords locations in Sandnes, samples were extracted from the A cut (Figure 2.2). The writer and Orhan Mahmic decided which samples to collect and at what depth, and the staff from Weatherford cut the samples, under careful observation of Lars Riber. The samples were named according to the respective core and depth, e.g. 16/1-13 1999.90. A total of 21 samples were collected.

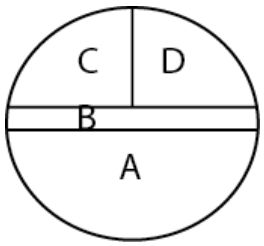

Figure 2.2: The Figure displays how the core was cut, and the location of the respective cuts. Logging on the B-cut and sampling from the A-cut.

Table 2.2: An overview of the collected samples

Sample	Depth	Description
1	2000.85	Clast 1
2	2000.30	Clast 2
3	1999.45	Clast 4
4	1998.30	Red, green and grey matrix
5	1996.60	Clast 5
6	1995.65	Grey matrix
7	1995.40	Clast 6
8	1994.90	Clast 9b
9	1991.55	Clast 8

10	1983.40	Grey sandstone
11	1983.20	Red and green matrix
12	1982.90	Red matrix
13	1979.25	Green, sandy matrix
14	1976.30	Clast 9a
15	1974.80	Green matrix
16	1967.95	Grey matrix
17	1965.70	Claystone
18	1959.65	Medium sandstone
19	1959.20	Fine sandstone
20	1952.50	Medium sandstone
21	1924.75	Medium sandstone

2.2 Facies description and facies associations

Facies definitions are based on core logs, pictures and thin sections. By determining lithology, texture and structure, one can divide into respective sedimentary facies. The facies is the sum of total features that reflect the environmental conditions under which the given rock was deposited. A facies association is made up of facies that are genetically related to one another, reflecting a specific sedimentary environment. The facies are grouped together in facies associations.

2.3 Mineralogical and petrographical analysis

Petrological analysis of the collected samples was performed by the use of optical thin-section observations, scanning electron microscopy (SEM), and electron microprobe (EMP) analyses on selected thin sections and stubs, and by X-ray diffractometry (XRD) on the bulk composition of the rock samples.

2.3.1 Thin section analyses

16 samples were prepared by Salahalladin Akhavan of the petro-technical department at the department of Geoscience at UiO, and Lars Kirksæther at IFE Petrosec prepared four samples. The rock samples were impregnated by blue epoxy and glued after drying, onto a 2.5 cm x 4.5 cm glass slide. Then the samples were polished down to a thickness of 30 μm.

A *Nikon Optiphot-Pol* petrographic microscope was used during the study of the thin sections, in order to give information on rock texture and mineralogy. During the optical microscopy, all thin sections were studied under plane polarized light (ppl) and cross polarized light (xpl), to observe mineral characteristics in detail. The thin sections gave information about mineralogy, lithology, structures, average grain size, grain shape and sorting.

The degree of rounding of detrital grains were decided by the use of Powers' (1953) terminology (Figure 2.3), while the degree of sorting was decided based on the classification scheme developed by Compton (1962) (Figure 2.4).

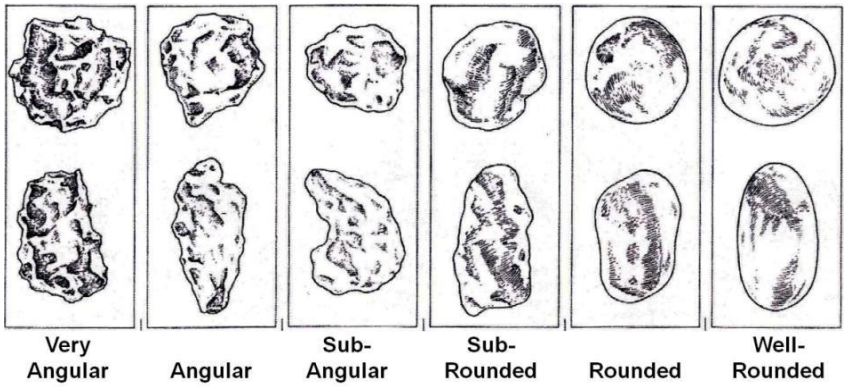

Figure 2.3: Terminology of degree of rounding of detrital grains (Powers, 1953).

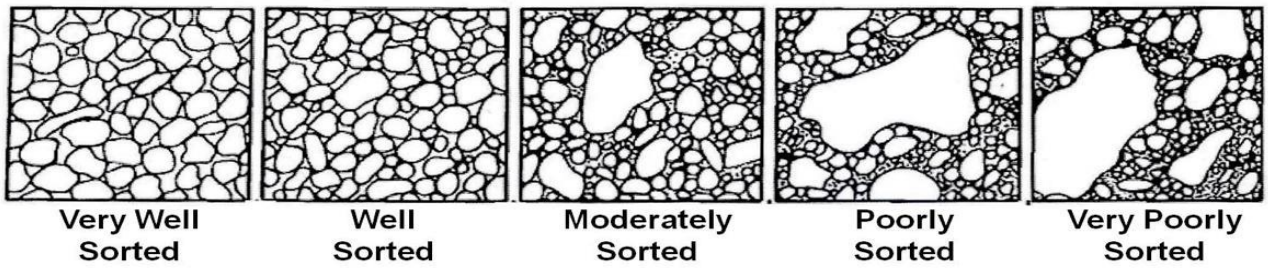

Figure 2.4: Classification regarding the degree of sorting (Compton, 1962).

Preservation of feldspar, ranging from visual categories I to V are displayed and described (Table 2.3 and Figure 2.5). Identified feldspar grains were, based on the degree of weathering, assigned to one of five categories. The categories represent a specific preservation of feldspar, where category I being "fresh" with perfect preservation, and category V, represent the end member and is the lowest degree of preservation (Table 2.3 and Figure 2.5). The feldspar grain of category V has been dissolved, and is barely recognisable (Table 2.3).

Table 2.3: Description of the criteria for the preservation of feldspar, ranging from category I to V.

Category	I	II	III	IV	V
Description	Fresh, has not been subjected to weathering	Subjected to some weathering. Twins are almost fully preserved	Twins starts to look blurry. Grain surface shows evidence of etching and sericitization	Very rough surface. Twins are difficult to recognise and substantial etching and sericitization is visible	Twins are absent. Only parts of the grain are preserved. Difficult to distinguish plagioclase from K-feldspar

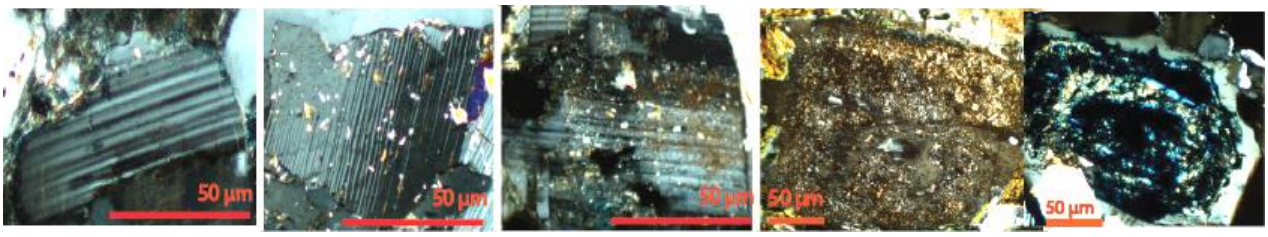

Figure 2.5: A Figure illustrating the different feldspar preservation categories. Category I is located to the left, and the preservation categories increases towards the right. Category V is located to the right.

The granitic basement clasts were classified using a modified version of the proposed scale given by the International Society for Rock Mechanics (ISRM). This classification uses a scale from 1-5, where 1 (fresh): no visible signs of material alteration, 2 (slightly altered): discolouration of surfaces, 3 (moderately altered): less than half of the rock material is decomposed, 4 (highly altered): more than half of the rock material is decomposed, and 5 (completely altered): all rock is decomposed, but original rock structure is still largely intact (ISRM, 1978).

2.3.2 Point counting

Point counting was performed on 13 thin sections (Appendix C). Four hundred points were counted by using a *Swift* point counter installed on a standard petrographic microscope. During the point counting, quartz grains were divided into monocrystalline and polycrystalline grains. Feldspar grains were separated into plagioclase and K-feldspar, and classified with the category of preservation. Other visible characteristics phases e.g. rock fragments, pore filling clay, cement, overgrowth, Fe-oxides, and pores in the thin sections, were counted. The basement clasts were classified in a standard Quartz-Plagioclase-Alkali feldspar (Q-P-A) diagram after point counting (Figure 2.6).

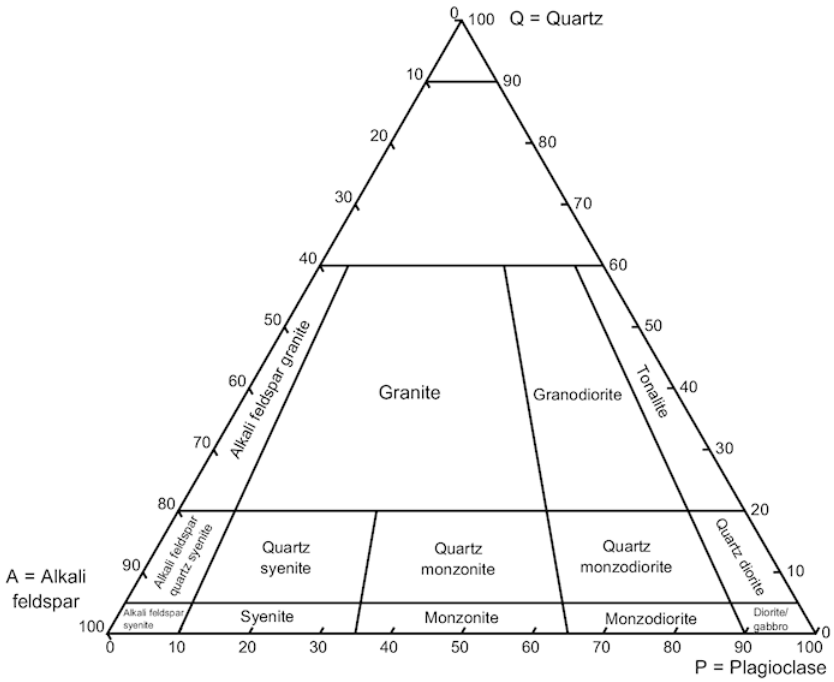

Figure 2.6: The standard Q-P-A diagram used for plotting the basement clast after point counting. Diagram after Streckeisen, 1967.

2.3.3 X-ray diffractometry (XRD)

XRD analysis was carried out at the Department of Geoscience at UiO, being a tool giving the mineralogical composition of rocks. It is especially applicable in quantitative studies and when phases are too small to be observed under microscopic analyses, like clays. The X-ray diffraction techniques are excellent for crystal structure analysis, due to the fact that minerals have characteristic crystal properties. Each mineral has a specific unit cell and a characteristic *d-spacing*. The *d-spacing* is the distance between the atomic planes in the mineral lattice. When bombarded with x-ray beams, each mineral give a specific signature, a diffraction pattern, in the form of d-spacing and 2θ angles, which will work as a function of the unit cell (Moore and Reynolds, 1997). The detection limit for XRD analyses is difficult to decide, since multiple factors may affect the results, but the detection limit is in the order of 1-2% in multiphase mixtures. However, the detection limit is highly dependent on the mixture itself. The detection limit will be different considering which phase you are looking for. It is easier to detect a phase with a clear peak, than to detect a phase located where several peaks are blending. A multiphase mixture can have many diffraction peaks that overlap, which will influence the detection limit (pers.com. M. Aerts, 2015).

17 samples were prepared for XRD analysis, where the main goal was to get an overview of the composition of all the samples. The XRD analyses were carried out on a *Bruker D8 advanced (40kV and 40mA)* diffractometer with *Lynxeye XE High-Resolution Energy Dispersive 1D Detector,* using *CuK*α radiation.

Bulk analysis preparation

All the samples were first ground to rock powder by a slinging mill. In this process the grain size is reduced to less than 500 μm, but most grains in the sample are reduced to 100-200 μm. The slinging mill was carefully cleaned with ethanol between every sample, to avoid contamination.

The next step in preparing the samples for XRD analysis was to run the rock powder in a *McCrone* micronizer machine. This machine further reduced the grain size down to 10 μm. In this process, 3.0-3.5 g of the rock powder from one sample and 8 ml of ethanol is mixed in a small container filled with 48 pieces of agate. The container is then put into the micronizer machine, and is run for 12 minutes. Afterwards, the micronized dispersion was put into an oven with a temperature of 40-50°C, where they were left for drying.

The final step of preparation for XRD-analysis was to place the very fine-grained rock powder on to small, plastic holders by the use of front-loading technique. The process of putting the rock powder onto the small holders had to be carried out with care, to omit artificial grain orientation.

Diffrac Eva program

The diffrac Eva software is used to evaluate and analyse X-ray diffraction data. The software helps to evaluate peaks, and identify the different mineral phases present in the diffractograms. The identification of the different mineral phases was utilized by using the d-space value and the two-theta values at the respective peaks (Bruker, 2011). The minerals chosen were extracted from the PDF (Powder Diffraction File) 2002 database published by the International Center for Diffraction Data (ICDD), which is used by the Eva software. The mineral phases were identified by the use of the values listed below:

- Clay minerals

    - Chlorite: the 001 reflection is present at 14.2 Å. The 002 reflection is present at 7.10 Å. The 003 reflection is located at 4.54 Å. The 004 reflection is present at 3.55 Å.
    - Kaolinite: the 001 reflection is present at 7.16 Å. The 002 reflection is located at 3.58 Å.

The presence of high-Fe chlorites in the sample can make it difficult to separate chlorite and kaolinite. The reason being, that the presence of high-Fe chlorite reduces the intensity of weak odd-order reflections (Moore and Reynolds, 1997).

- Quartz: the 002 reflection at 4.26 Å was used instead of the 001 reflection.
- Feldspars
    - Plagioclase: the 001 reflection at around 3.19 Å was used.
    - K-feldspar: the 001 reflection at around 3.24 Å was used.
- Carbonates:
    - Calcite: the 3.03 Å reflection was used.
- Other minerals
    - Hematite: the reflection at 2.70 Å and the reflection at 2.51 Å was used.
    - Halite: the reflection at 2.81 Å was used
    - Sylvite: the reflection at 3.14 Å and the reflection at 2.22 Å was used,
    - Mica/Biotite/illite: the 10 Å reflection was used.

The Siroquant version 4 software were supposed to be used during this master thesis, but due to technical problems with the software, the author, in agreement with Maarten Aerts and Henning Dypvik, chose to run the XRD quantification in the Profex version 3.3.1 software instead.

Profex version 3.3.1 software

Profex is a graphical software that uses Rietveld refinement on powder X-ray diffraction data, to extract more information. The program reads and displays the diffraction pattern imported, and will when mineral phases are chosen, set up control files with databases for crystal structures and instrument configurations. These control files takes into account unit cell dimensions, phase quantities and crystallite sizes and shapes. The program does not identify mineral phases, so that was done in the Eva software, before the profex quantification. When all mineral phases observed were chosen, the profex program summarised the quantities for every chosen mineral phase (Profex, 2015).

2.3.4 Scanning electron microscope (SEM)

SEM was used to identify minerals that could not be identified in the optical microscope. Thin sections and stubs were studied in greater detail in an electron microscope, with focus on detecting authigenic minerals and study the preservation of grains. SEM analysis was performed on a *JEOL JSM-6460LV*, with a *LINK INCA Energy 300 (EDS)*, at the Department of Geoscience at UiO, by the author under the supervision of Berit Løken Berg. The thin sections were coated with carbon, while the stubs were coated with gold, before placed in the machine. Backscatter electron image (BEI) was used during the study of the thin sections, while secondary electron image (SEI) was used during the study of stubs. Only samples from 16/1-13 were studied during SEM.

2.3.5 Electron microprobe (EMP)

Electron microprobe (EMP) analysis was performed using a *Cameca SX 100* instrument fitted with 10 nA beam current and 15 KV accelerating voltage. The electron microprobe was used to study the K-feldspars composition. The electron microprobe analysis was performed at the Department of Geoscience, UiO, with assistance from Muriel Marie Laure Erambert. Samples from well 16/1-13 and one sample from 16/1-15 were studied during EMP. See Figure 1.2 for location of the wells.

3. Results

3.1 Facies description and facies association

Well 16/1-13 is part of the Edvard Grieg Field, located at the Haugaland High in the southern part of the Utsira High (Figure 1.2). The core section was logged in the scale of 1:20 and the samples and observations were noted in the log. The sedimentological logs of the entire core are displayed in Figures 3.1 and 3.2, while the more detailed logs can be found in appendix A. Figure 3.1 displays the lower part of the core, in a scale of 1:50. This section covers the depths from 2001.10 m to 1967 m, and constitutes facies association 1 (FA 1). Figure 3.2 displays the middle and upper part of core 16/1-13, and cover depths ranging from 1967 m to 1917 m, constituting facies association 2 and 3 (FA 2 and FA 3). The middle and upper part of the core are presented in a scale of 1:100. Core 16/1-13 consists mainly of silisiclastic material, in the form of conglomerates, silt-, mud- and sandstones. Carbonates are observed at the top of the section, mainly as marls, calcareous sandstone and calcareous siltstone. 10 different facies, and 3 different facies associations have been identified in the logged section (Table 3.1).

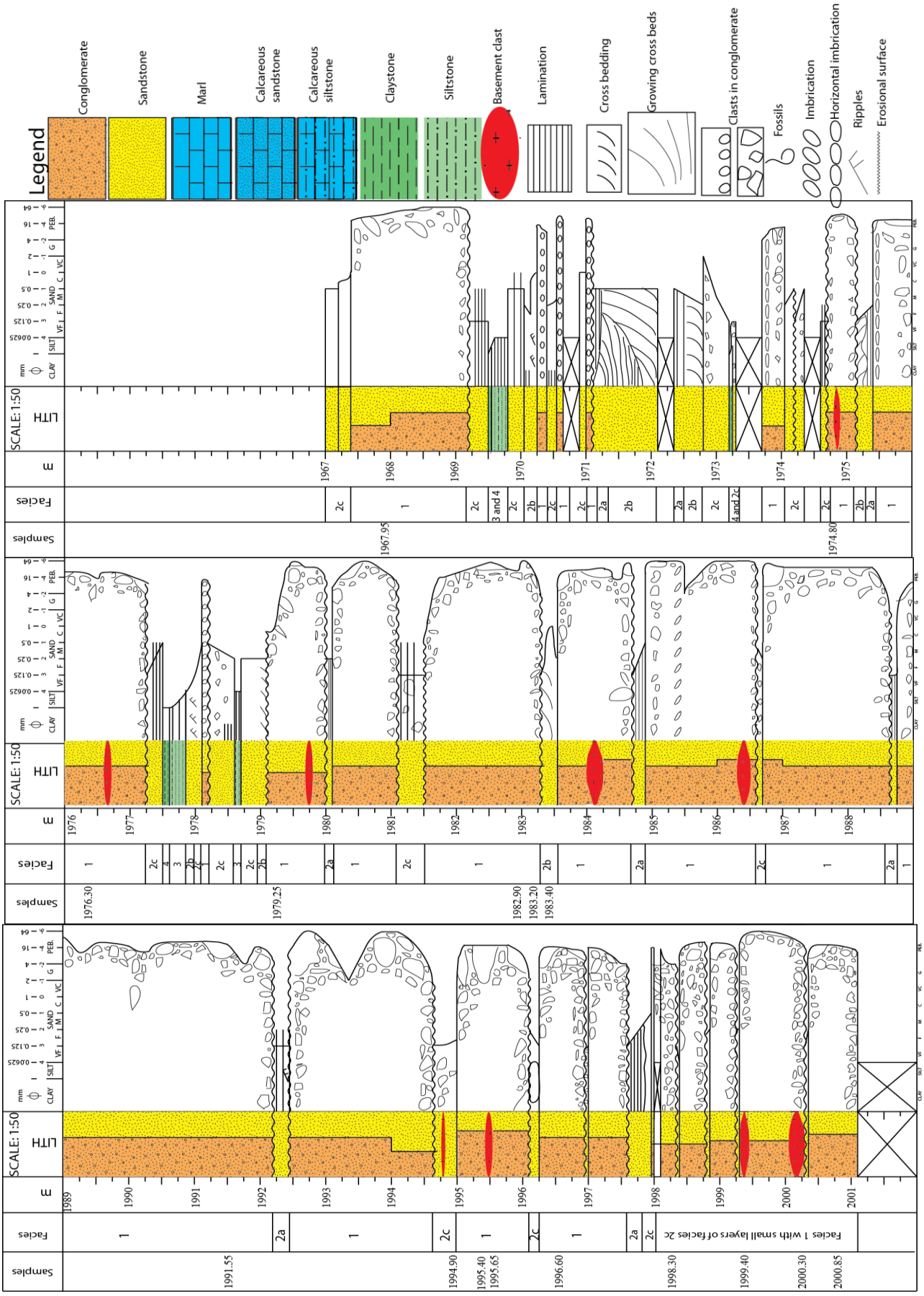

Figure 3.1: Sedimentological log from core 16/1-13. The log is in the scale of 1:50, and ranges from a depth of 2001.10 m to 1967.00 m, with corresponding legend. This section constitutes FA 1.

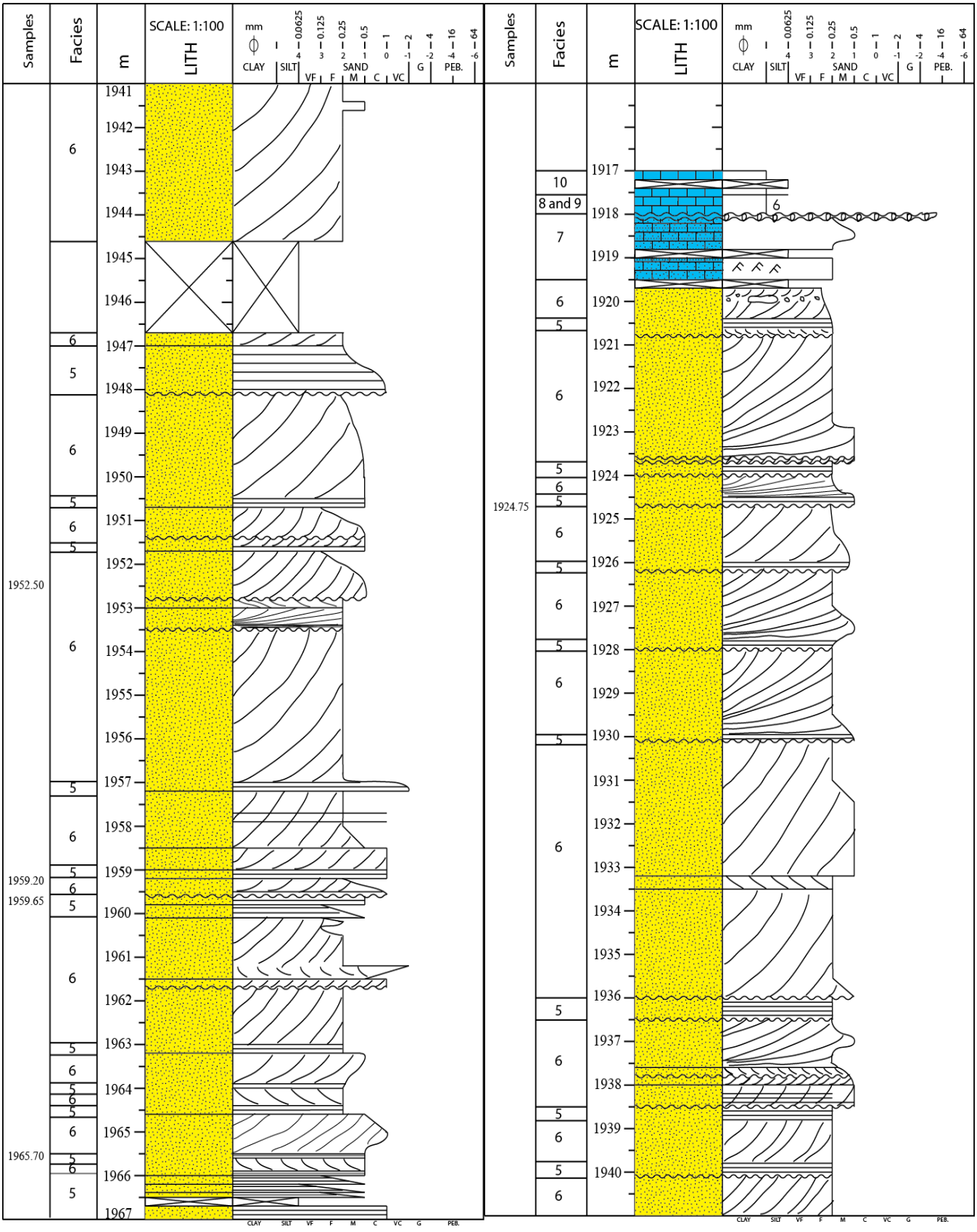

Figure 3.2: Sedimentological log from core 16/1-13. The log is in the scale of 1:100, and ranges from a depth of 1967.00 m to 1917.00 m. Legend can be observed in Figure 3.1. FA 2 range from 1967-1917.70 m, and FA 3 range from 1919.43-1917.00 m.

Table 3.1: Sedimentological facies found in core 16/1-13

Facies nr.	Facies	Grain size	Physical appearance	Samples
1	Conglomerate	Ranging from granule to cobble	Grain supported, but a lot of matrix in between grains. The conglomerate is dominated by basement fragments. Grains are angular to sub-rounded.	1, 2, 3, 5, 7, 8, 9 and 14
1a	Grey matrix		The dominating matrix. Contains clasts in the range from pebble-cobble.	4, 6 and 16
1b	Red matrix		Contains clast in size equal to granule. Have a high abundance of clasts.	4, 11 and 12
1c	Green matrix		Grain size similar to red matrix, but with a higher abundance of larger clasts. The frequency of clasts is reduced, compared to the red matrix.	4, 11, 13 and 15
2	Sandstone	Very fine – coarse sand	Strings of clays, ripples, climbing ripples and varves.	10
2a	Laminated	Very fine - coarse sand	Prograding ripples can be observed. Small basement clasts can be observed in some of the laminated sandstone layers.	
2b	Cross-bedded	Very fine - coarse sand	Weak cross bedding can be observed. Dominating direction on cross beds is from "right to left" in the core section.	
2c	Structureless	Very fine – coarse sand	Small basement clasts can be observed in the sand layers. No sedimentary structures are visible. Clay strings can also be observed in certain layers.	
3	Siltstone	Silt	Laminated. Light grey.	
4	Claystone	Under 4 μm	Dark grey colour. No structures.	17
5	Parallel laminated sandstone	Fine-coarse sand	Dark to light brown. Carbonate cemented. Oil staining observed.	18, 20 and 21
6	Cross-bedded sandstone	Fine – medium sand	Dark to light brown. Fractured and carbonate cemented. Oil staining observed.	19
7	Calcareous sandstone	Fine – coarse sand	Contains shell fragments and belemnites. Observation of ripples. Dark brown.	
8	Green marl	Under 4 μm	Contains shell fragments and belemnites are present.	
9	Calcareous siltstone	Silt	Dark brown. Fossils in the form of shell fragments and belemnites.	
10	Red marl	Under 4 μm	Contains few fossil fragments, represented by shell fragments and belemnites.	

3.1.1 Facies description

1. Conglomerate:

This facies is present in the lower most part of the core (2001.10-1967.35 m) (Figure 3.1), represented by multiple layers. The base of the unit was not present in the core. These

conglomerates are clearly grain supported, classifying them as ortho conglomerates, but they are rich in matrix, and polymict. The conglomerates contain angular to sub-rounded clasts, ranging in size from granule to cobble, with varying composition. The clasts were mostly igneous in origin. The conglomerates display different types of matrixes, grey, red, and green. Sandstone layers from facies 2 separate the conglomeratic layers.

The conglomerates contain various basement clasts. The clasts are of different shape and size. During logging, a classification scheme was made, in order to separate the different clasts. A total of nine classes were identified, based on colour, the amount of dark minerals (biotite) and size of crystals. Samples were only taken of seven clasts, since the other two classes were not present in the A-cut. Photos of the different basement clasts and the following classification scheme can be observed in Figure 3.3 and the respective figure caption, and in Table 3.2.

Table 3.2: The classification scheme used during logging, to separate basement clasts present in the conglomerates

Class	Representative sample	Description
1	2000.85	Red, fine-grained granite with the presence of some dark minerals (Figure 3.3 A)
2	2000.30	Fine-grained, dark red granite with lots of dark minerals (Figure 3.3 B)
3	NA	Fine-grained, pink granite, with a few light minerals (Figure 3.3 A)
4	1999.40	Coarse-grained, red granite (Figure 3.3 C)
5	1996.60	Fine-grained, red granite with no dark minerals (Figure 3.3 D)
6	1995.40	Grey, coarse-grained granite (Figure 3.3 F)
7	NA	Orange, coarse-grained granite (Figure 3.3 E)
8	1991.55	Black and white, coarse-grained granite (Figure 3.3 G)
9	1994.90 (9b) and 1976.30 (9a)	Coarse-grained, green granite (Figure 3.3 H and I)

Figure 3.3: Photos taken of the different basement clasts found during logging. Scale and respective clast class is marked on photos. A: Class 1 is a red, fine-grained granite, with the presence of some dark minerals (from 1999.70 m). Class 3 is a fine-grained, pink granite, with a few light minerals (from 1999.70 m). B: Class 2 is a fine-grained, dark red granite with lots of dark minerals (from 2000.30 m). C: Class 4 is a coarse grained, red granite (from 1999.45 m). D: Class 5 is a fine-grained, red granite with no dark minerals (from 1996.60 m). E: Class 7 is a orange, coarse-grained granite (from 1986.65 m). F: Class 6 is grey, coarse-grained granite (from 1996.60 m). G: Class 8 is a black and white, coarse-grained granite (from 1991.55 m). H: Class 9a is a green, coarse-grained granite without visible weathering (from1976.30 m). I: Class 9b is a green, coarse-grained granite with visual signs of weathering (from 1994.90 m).

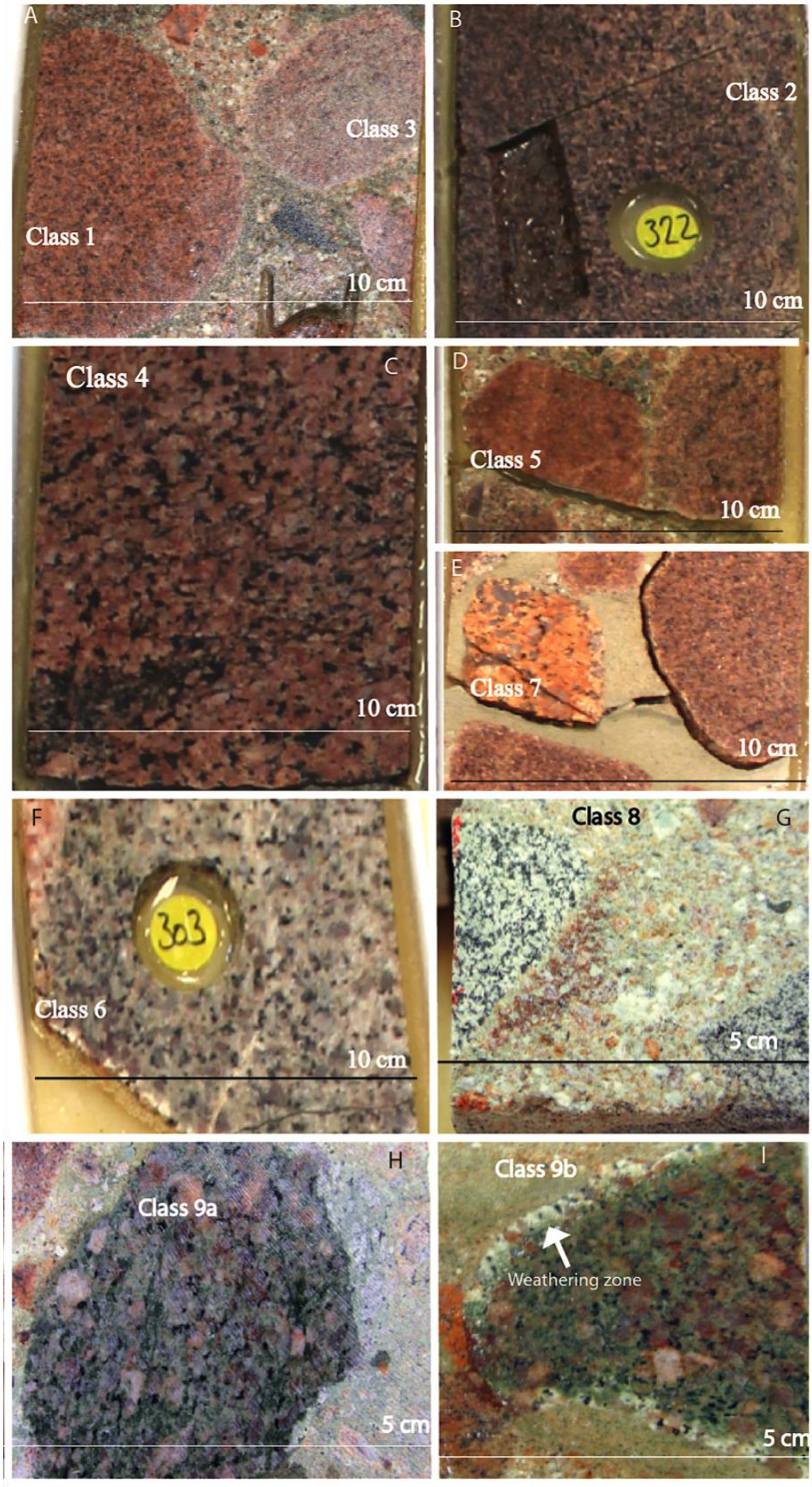
A
Class 3
Class 1
10 cm
B
Class 2
322
10 cm
Class 4
C
10 cm
D
Class 5
10 cm
E
Class 7
10 cm
F
303
Class 6
10 cm
Class 8
G
5 cm
H
Class 9a
5 cm
Class 9b
I
Weathering zone
5 cm

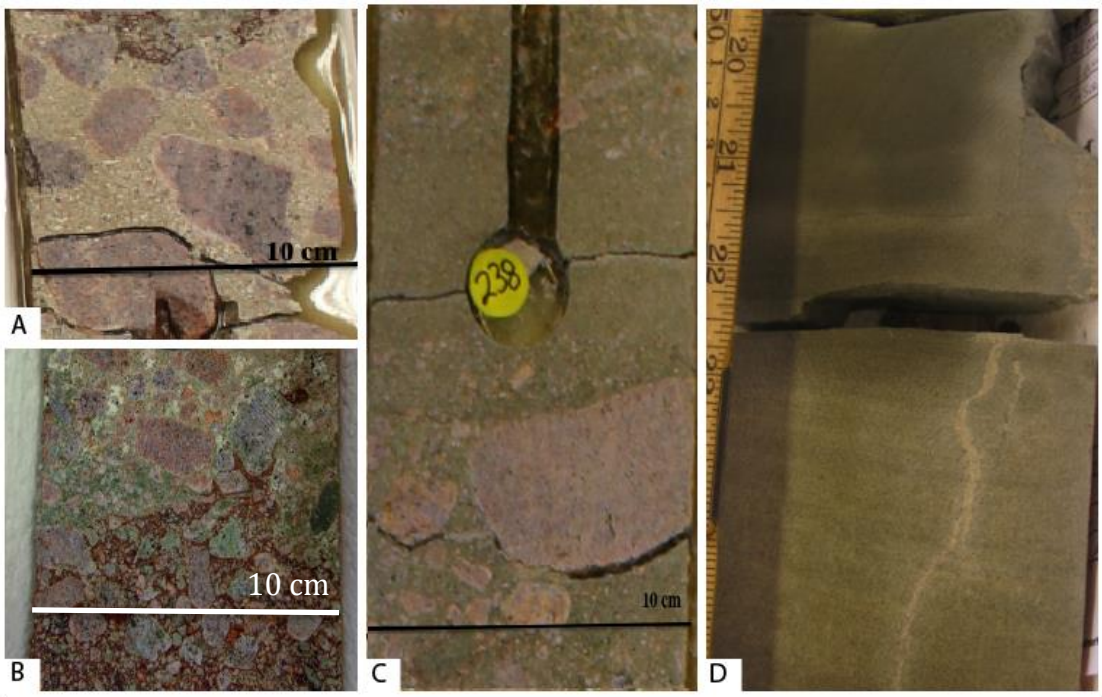

Figure 3.4: Figure A represents the grey matrix, which generally contains the largest basement clasts. Taken from a depth of 1992.60 m. Figure B shows the red matrix. Notice the high abundance of basement clasts present in the red matrix, and notice also the flame structure present at the top boundary. Green matrix can be observed at the top of the red matrix, and notice how the frequency of clasts decreases from red to green matrix. Taken from a depth of 1981.70 m. Figure C shows the green matrix taken from a depth interval ranging from 1979.15 to 1979.30 m. Note how the clast abundance is reduced compared to the red (Figure B), but the clast size is quite similar. There is also a higher abundance of larger clasts. Figure D shows the presence of the laminated siltstone in the lower part of the Figure and the claystone is present in the upper part of the Figure. Taken from depth interval 1969.50-1969.75 m.

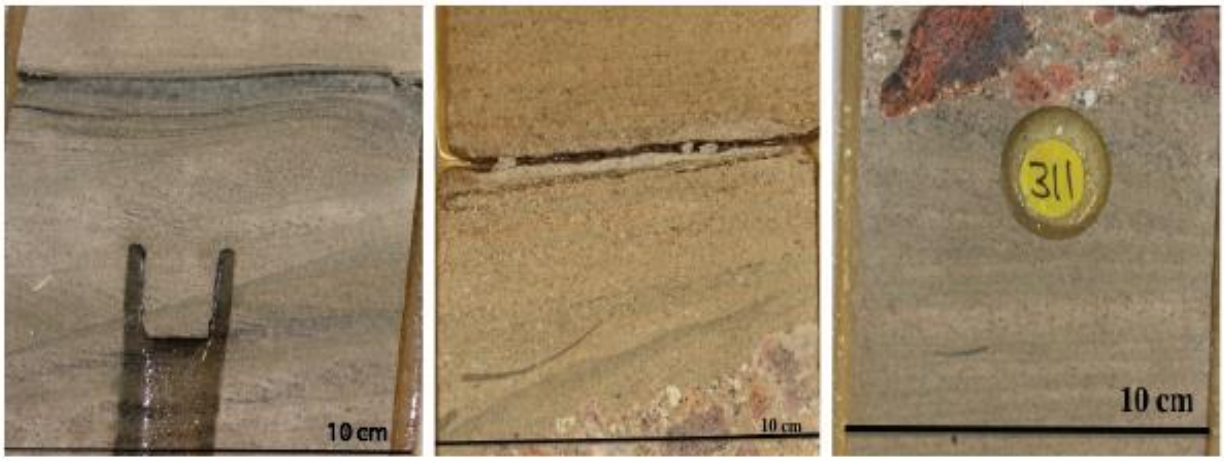

Figure 3.5: Structures observed in sandstones. To the left, climbing ripples can be observed. Taken from a depth interval ranging from 1970.10-1970.20 m. The middle Figure shows the presence of a prograding dune and a clay string. Taken from a depth of 1992.40 m. To the right, varves can be observed. Notice how the grey matrix erodes the top of the sandstone. Taken from a depth interval ranging from 1997.60-1997.80 m. Scale can be found in the bottom right in every Figure.

1a. Grey matrix

The grey matrix (Figure 3.4 A) is the most dominant matrix type in the conglomerates. It contains the largest clasts (pebble-cobble), and the matrix is the most common. The intervals of grey matrix are generally thicker than the two other matrix types. The grey matrix represents the most matrix rich sections found in the conglomerates, where the conglomerates contain less basement clasts, but the conglomerates are still grain supported.

1b. Red matrix

The red matrix (Figure 3.4 B) is the second most frequent matrix of the conglomerates. In the sections where the red matrix can be observed, one can clearly observe a decrease in clast size (granule), compared to the grey matrix. The red matrix displays a well-developed grain supported structure, reflecting a high clast frequency.

1c. Green matrix

The green matrix (Figure 3.4 C) is the least prominent matrix of the conglomerates. The clast size in the green matrix is quite similar to those of the red matrix, but there is a higher abundance of larger clasts, and the frequency of clasts is lower in the green compared to the red matrix. The green matrix appears, in some parts of the core, to be more matrix supported.

2. Sandstone

Sandstones of facies 2 can be observed in the lowermost part (2001-1967 m) of the core section (Figure 3.1), between the conglomeratic units. The sandstones can be divided into three separate units, based on their sedimentological structures observed. Unit 2a consists of parallel laminated sandstones, unit 2b consists of cross-bedded

Figure 3.6: The Figure shows the presence of a cross-bedded sandstone from facies 2. The transition from conglomerate to sandstone is marked by a decrease in grain size. The transition is marked with a black arrow. The red arrow, points to an erosional surface found at the transition from sandstone to conglomerate. Taken from a depth interval ranging from 1979.15-1979.40 m.

sandstones, and unit 2c consists of homogeneous sandstones without any clear sedimentological structures. The transition from conglomerates to sandstone is often sharp, but the transitions from sandstone to conglomerate are often found to be an erosional surface (Figure 3.6). Unit 2a and 2c is the most prominent types, and the sandstones are mostly light grey, but in some intervals, dark grey layers are present. Clay strings, climbing ripples, prograding ripples, and varves have also been observed in the sandstones (Figure 3.5). Basement clasts of granule size can be observed in a few of the sandstone units. In some of the sandstone units, one can observe tiny laminations, often a few millimetres thick, with varying grain size, which are found to be upwards fining, and upwards coarsening.

3. Siltstone

The siltstones are found in the lower part of core 16/1-13, at depth intervals ranging from 1979 m to 1977 m and 1970 m to 1969 m (Figure 3.1). The siltstones are parallel laminated, and not frequent in the studied core section. The siltstones are light grey in colour. See Figure 3.4 D for photo.

4. Claystone

The claystones are found in the lower part of the core, at depth intervals ranging from 1979 m to 1977 m and 1970 m to 1969 m (Figure 3.1). The claystone appears to be massive, with no clear structures. The colour of the claystones is dark grey. See Figure 3.4 D for photo.

5. Parallel laminated sandstone

Sandstones of facies 5, have been observed in the middle section of the core (1967-1920 m) (Figure 3.2). The parallel laminated sandstones often succeed an erosional surface, where underlying cross-bedded sandstone is present. The parallel laminated sandstones are often found to be coarser than the cross-bedded sandstones of facies 6 (Figure 3.7). The grain size range from fine to coarse sand (grains up to one mm are observed), but the dominating grain size is medium sand

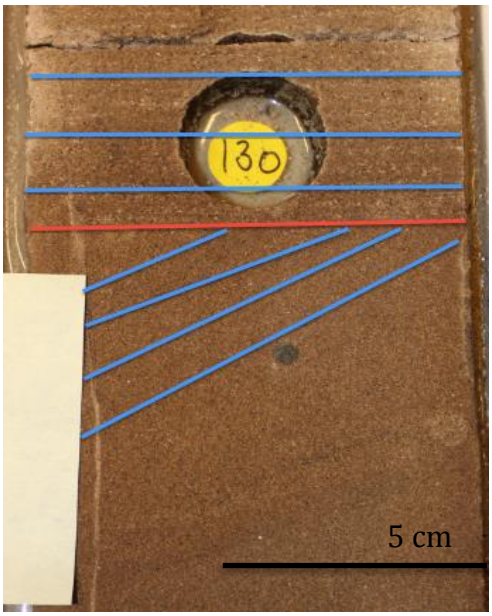

Figure 3.7: The Figure shows the laminated and the cross-bedded sandstone. The two sandstones are separated by an erosional surface (red line). Notice how the grain size increases in the parallel laminated sandstone.

(250-500 μm) (Table 2.1). The dominating colour is light brown, but some intervals show a darker brown colour, which is caused by oil staining, created by migrated hydrocarbons. The individual laminae of the parallel laminated sandstones, are too small to reveal internal grain size relation.

6. Cross-bedded sandstone

The sandstones of facies 6 can be observed in the middle section of the core from 1967 m to 1919.70 m depth (Figure 3.2). The cross-bedded sandstone is the most common facies in this part of the core, and both dip angle (20 degrees) and the direction of the cross bedding are quite stable. A few sandstone units show different direction of transport, but these sandstone units are not frequent or thick. The cross-bedded sandstones are often eroded at the top of the unit. There is often a gradual change from parallel lamination to cross bedding, by gradually growing cross-beds (Figure 3.8). The top of these sandstone units are often eroded, and followed by more medium to coarse grained, parallel laminated sandstones of facies 5 (Figure 3.7). The individual beds found in the cross-bedded sandstone were found to be upwards coarsening. The grain size is in the range from fine to medium sand (Table 2.1), where fine sand (0.125-0.25 mm) is the dominating grain size. The dominating colour is light brown, but some intervals show a darker brown colour, due to oil staining.

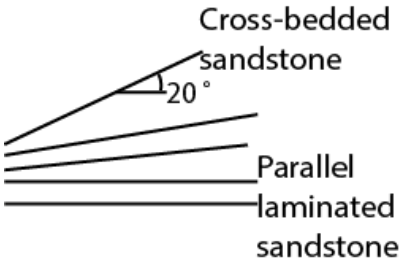

Figure 3.8: A schematic Figure showing the visual appearance of the growing cross beds, and their development from parallel laminated to cross-bedded sandstone. These structures are observed in the sandstones of FA 2.

7. Calcareous sandstone

The calcareous sandstones of facies 7 can be observed in the upper section of the core from level 1919.46 m to 1918.10 m depth (Figure 3.2). The calcareous sandstones are dark brown and consist of grain sizes ranging from medium to coarse sand (Table 2.1). Ripples have been observed. Fossils, mainly belemnites, are also present in the sandstones. The calcareous sandstone reacts with 10% HCl.

8. Green marl

The green marl of facies 8 can be observed in the interval ranging from 1918.00 m to 1917.74 m (Figure 3.2). The green marl contains stringers of white calcite, which reacts with 10% HCl. Fossil fragments, mostly belemnites and shell fragments, have been observed.

9. Calcareous siltstone

Calcareous siltstones of facies 9 are present at level 1917.74 m to 1917.60 m (Figure 3.2). This calcareous siltstone is very similar to the calcareous sandstone observed in level 1919.46 to 1918.10, in spite of the grain differences. It is dark brown and contains fossils, in the form of belemnites and shell fragments.

10. Red marl

The red marl of facies 10 is present from level 1917.60 m to 1917.00 m (Figure 3.2), characterized by less fossils. The red marl contains stringers of white calcite, which reacted with 10% HCl.

3.1.2 Facies association

FA 1: Conglomerate, sandstone, siltstone and claystone

FA 2: Parallel laminated sandstone and cross-bedded sandstone

FA 3: Calcareous sandstone, green marl, calcareous siltstone and red marl

FA 1 (2001.10 – 1967 meters)

The lower most facies association (FA 1) of the studied core, is composed of sequences of conglomerates (1), sandstones (2), siltstones (3) and claystones (4) (Figure 3.1 and Table 3.1). The conglomerates contain three different matrix types (1a, 1b and 1c). The grey matrix is by far the most dominating matrix in the conglomerates, and can be found throughout the entire facies association. The red matrix has only been observed from the base of the core and up to a depth level of 1980.20 m. The contact zones between the different matrixes are most commonly sharp and follow grain contacts, but more diffuse transitions may occur. At the transition between lower intervals with red matrix to an upper interval with grey or green matrix, loading structures occur frequently, and also flame structures have been observed (Figure 3.4 B). The green matrix are only observed in small units in the lower part of FA 1, and are often found within red matrix dominated zones (Figure 3.4 B). From depth level 1979.40 m and upwards, the green matrix occurs in thick zones. These zones of green matrix towards the top of FA 1 contain smaller clasts and tend to be more matrix supported, than the green matrix zones found below 1979.40 m. It is observed that the red matrix contains the highest abundance of basement clasts, and that the size of the clasts generally is smaller compared to the clasts of the grey matrix.

The sandstone layers separate each sequence of conglomerate and show indication of erosion on the top, before a new layer of conglomerate appears (Figure 3.6). A few of the sandstone layers display parallel lamination and cross bedding, but generally the sandstone layers within FA 1 are structureless, and appear to be massive. FA 1 consists of alternating sequences of conglomerates and sandstones, where the conglomerates are found to show upward coarsening trends in the lower part of the sequence, before it gradually changes to an upwards fining trend, finally ending in fine sandstones at the top of the sequence. The sandstone layers found in between the conglomerates, become more frequent and thicker towards the top of FA 1 (Figure 3.1). Towards the top of FA 1 (from depth level 1970.60 to 1969 m), the sand units are found to have multiple layers of laminated beds (Figure 3.1). The individual laminated beds are a few millimetres in thickness and they consist of different grain sizes, but are too small for differentiation of e.g. upwards coarsening or upwards fining trends. Towards the end of FA 1, at a depth intervals ranging from 1979 m to 1977 m and 1970 m to 1969 m, silt- and claystones appear. There is a gradual change from sandstone to siltstone, continuing into claystone in parts of the core (1969.75-1969.50 m and 1977.75-1977.50 m). The transition from claystones back to sandstones is sharp, but the claystone does not appear to be eroded at the top.

From depth level 1979 to 1967 meters, there is a gradual change from conglomerate (1) dominated facies to more sandstone (2) dominated facies, where multiple units are represented (Figure 3.1). Some layers of conglomerate can still be found, but the frequency and thickness of the conglomerate units decrease. The thickness and frequency of the sandstone units of facies 2 increase during this depth interval (Figure 3.1).

FA 2 (depth 1967-1919.70 meters)

The middle facies association (FA 2) (1967-1919.70 m) is composed of alternating sequences of cross-bedded sandstone (6) and parallel laminated sandstone (5) (Figure 3.2). After level 1967 m, the conglomerate units disappear, and interfingering relations between the sandstones of facies 5 and 6 exist. The differences in grain size and sedimentological structures are what separate the two sandstones. The first type of sandstone, from facies 6, contains fine to medium sand (0.125-0.5 mm), often cross-bedded, while the other sandstone, from facies 5, often parallel laminated, contains grains that range from fine and up to coarse sand (0.125-1 mm). Sandstones from facies 5, contain small individual laminated beds that are a few millimetres thick, but are in the core too small to reveal internal grain size zonation. The

cross-bedded sandstone (6) is by far the dominating sandstone in FA 2, particularly above level 1944.70 m, while the coarse grained (grains up to 1 mm), parallel laminated sandstone, from facies 5, disappears above this depth level. The fine-medium grained, parallel laminated sandstone from facies 5, occur throughout the entire FA 2.

In the core a dominating direction of the cross bedding has been observed, going from right to left in the B-cut of the core. The parallel laminated sandstones are often observed along the base of a sequence, before gradually changing to cross-bedded sandstones. The angle of the cross-beds gets gradually steeper, before it stabilizes at around 20 degrees (Figure 3.8). The top of the sequences is often eroded, before the succeeding sequence with parallel laminated sandstone (Figure 3.7). Separate units of parallel laminated sandstone have been observed. Both the laminated sandstone and the cross-bedded sandstone display grain sizes in between fine-medium sand (0.125 – 0.5 mm), dominated by fine sand.

Parts of FA 2 show clear signs of being carbonate cemented. The cemented sandstone reacts with 10% HCl. No structures were observed in the cemented parts, and the colour changes from brown to white-grey.

FA 3 (1919.43-1917 meters)

The change from FA 2 and FA 3 is abrupt, and can be observed by a change in colour and sedimentological structures. There is a change from cross-bedded sandstone (6), to calcareous sandstone (7) containing ripples. The calcareous sandstone (7) at 1919.43 meters depth reacts strongly with 10% HCl, while the cross-bedded sandstone (6) at 1919.70 meters depth does not react with HCl. The colour also becomes darker brown in the calcareous sandstone above 1919.43 meter, but UV light does not indicate the presence of hydrocarbons. The calcareous sandstone is the first facies found in this facies association interval (1919.43-1917 m) (Figure 3.2). It contains fragments of fossils, mostly belemnites and shell fragments, and ripples can also be observed. A 10 cm thick grain-supported conglomerate, are found between the calcareous sandstone (7) and the green marl (8) (Figure 3.2). The green marl contains white shell fragments and belemnites. There is an abrupt change from green marl to calcareous siltstone (9) at 1917.74 m (Figure 3.2). The calcareous siltstone contains belemnites and shell fragments. The red marl of facies 10, is represented from depth level 1917.60 -1917.00 m (Figure 3.2). The red marl has fewer fossil fragments than the other facies present in FA 3. The red marl marks the top of core 16/1-13.

3.2 Petrographic and mineralogical description

3.2.1 Thin section analysis and point counting

FA 1

Facies association 1 is covered by 16 thin sections (Table 2.2); eight representing basement clasts from the conglomerates, one from a sandstone layer, and the remaining seven representing the different matrixes. All samples were taken from the lowermost part of core 16/1-13, from depth levels of 2001-1967 m. Results from optical, thin section analyses are found in appendices B and C.

The basement clasts

Clast 1 (2000.85) (Figure 3.3 A) has varied sizes of the phenocrystals, ranging from very coarse to medium (Table 2.1 and Table 2, Appendix B). The quartz grains are larger than the feldspar grains in this sample. The major part of the porosity in the sample, does clearly have a secondary origin, and is found near dissolved feldspars. There is no clear connection observed between the various pores, thus the clast most likely carry poor permeability. Fe-oxide has been observed along some of the grain contacts and in fractures. Biotites are partly replaced by chlorite. Pore filling clays and micas are seen associated with dissolved feldspar, especially the plagioclase. The clays observed in thin section were too few to be detected during point counting (Table 3, Appendix C). The micas are found to constitute 2% from point counting (Table 3, Appendix C). Myrmekite has been observed in the feldspars (Table 2, Appendix B). The degree of weathering implies a type 2 weathering (Table 2, Appendix B), and in the Q-P-A plot (Figure 3.9), the clast, 2000.85, plots as granite (red dot). With respectively 45 and 42 % of the counted feldspar phenocrystals, category II of feldspar

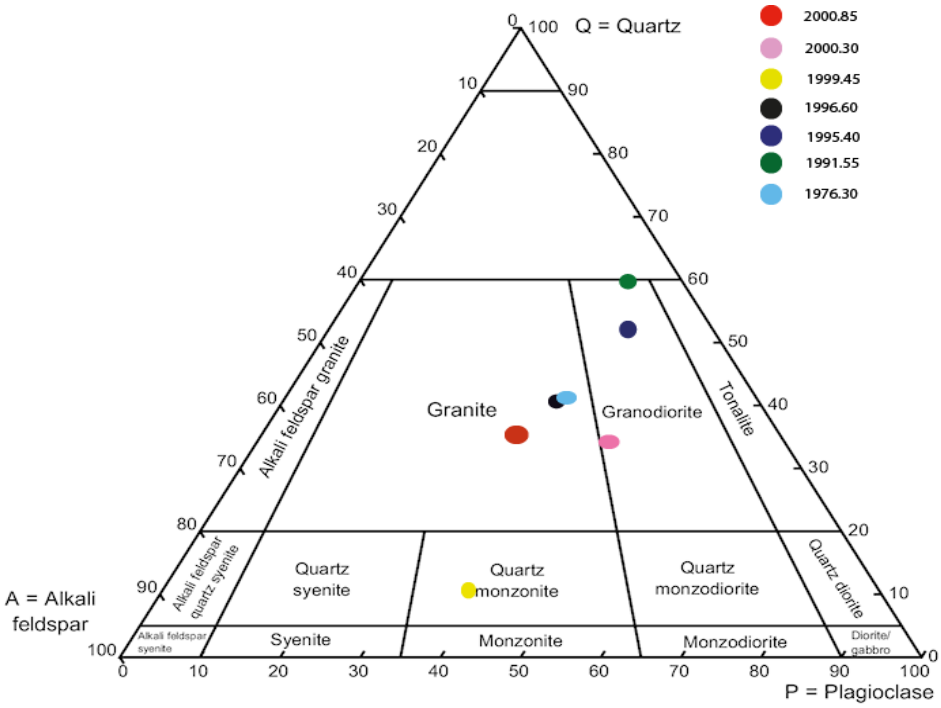

Figure 3.9: A Q-P-A diagram showing the plotted basement clast after results from point counting. Red=clast 1, pink=clast 2, yellow=clast 4, black= clast 5, purple=clast 6, green=clast 8, and light blue=clast 9a.

preservation dominates, both for K-feldspar and plagioclase (Tables 4 and 5, Appendix C). Point counting reveals a content of 32% quartz, where monocrystalline dominate. The feldspar content is found to be 60%, where the K-feldspar and plagioclase each make up 30% of the sample. The porosity in the clast is found to be around 1% (Table 3, Appendix C); all secondary porosity (Table 6, Appendix C).

Clast 2 (2000.30) (Figure 3.3 B) has phenocrystals ranging in size from medium to coarse (Table 2.1), with an average size of around 0.9 mm (Table 2, Appendix B). A fracture can be observed in the thin section, and this fracture, together with pores associated with dissolved feldspar, makes up the porosity in the sample, which is found to be 2% from point counting (Table 3, Appendix C). All counted porosity is found to be secondary in origin (Table 6, Appendix C). The permeability in the granite is most likely poor, due to low communication between pores. Even in the fracture zone, the permeability most likely is low, due to the occurrence of biotite grains within the fracture (Figure 3.10). These biotite grains show signs of degradation, due to the presence of clays in between, and moving out of the biotite cleavages (Figure 3.10). Biotite was found to make up 9% of the sample (Table 3, Appendix C). The feldspars show indication of dissolution, especially in the central parts of the crystals. The plagioclase shows a higher degree of alteration than the K-feldspar, where category II dominates in plagioclase and category I in the K-feldspar. All the feldspar preservation categories were observed for the plagioclase (Tables 4 and 5, Appendix C). This basement clast classifies as a type 3 (Table 2, Appendix B), and in the Q-P-A diagram it plots as granodiorite (pink dot) (Figure 3.9). Even though the clast classify as a type 3, the amount of clay is found to be only 2% (Table 3, Appendix C). Fe-oxides have been observed in between grain contacts (Figure 3.10). Myrmekite structures are also observed in association

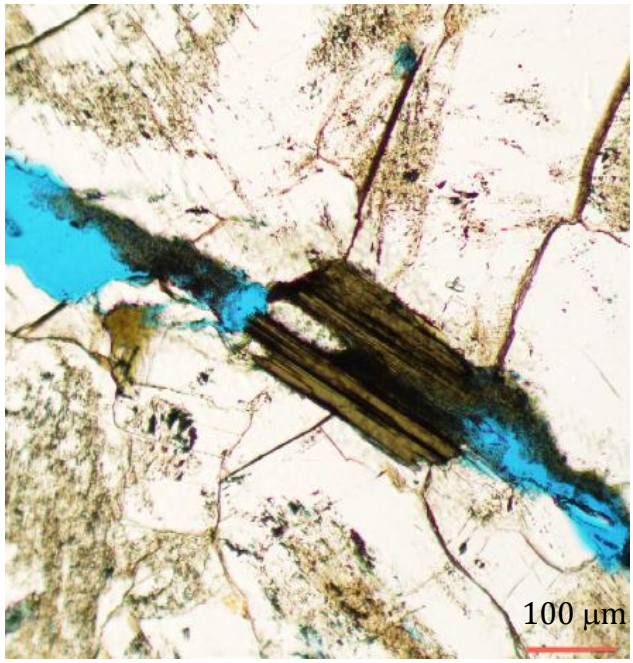

Figure 3.10: The photo shows the presence of biotite located within the fracture zone observed in clast 2. Notice how clay minerals appear to derive from the biotite, due to degradation and alteration. Optical analyses indicated that the clays flow out of the degraded biotite cleavages. Notice also the Fe-oxides present in grain contact areas.

with the feldspars (Table 2, Appendix B). Point counting showed an average quartz content at around 29%, where monocrystalline dominated. Regarding the feldspars, plagioclase constitutes 34%, while K-feldspar makes up 17% (Table 3, Appendix C).

Clast 4 (1999.45) (Figure 3.3 C) consists of phenocrystals with sizes ranging from very coarse to medium (Table 2.1 and Table 2, Appendix B). The feldspar crystals are larger than the quartz crystals, but there is also a difference in the feldspars; K-feldspars typically larger than plagioclases. The sample contains 17% chlorite (Table 3, Appendix C), displaying some deformation, with needle-like structure. Category II is the dominating class for both plagioclase and K-feldspar preservation (Tables 4 and 5, Appendix C). The porosity is counted to be 1%, and all is of secondary origin (Tables 3 and 6, Appendix C), associated with areas of feldspar dissolution. There is no communication between the pores, giving this clast likely low permeability. The degree of weathering can be classified as a type 2 (Table 2, Appendix B), and in the Q-P-A diagram it plots as quartz monzonite (yellow dot) (Figure 3.9). The thin section reveals fractures, but they seem to be randomly oriented. Myrmekite is observed. In clast 4, the quartz content is low, only making up 5% of the sample. K-feldspar is the dominating mineral in this sample, making up 38%, while plagioclase makes up 33%. The mica makes up 5%, and is found to be muscovite/illite in association with altered feldspar. The clay minerals make up only 1% (Table 3, Appendix C).

Clast 5 (1996.60) (Figure 3.3 D) consists of phenocrystals with an average size of 1 mm (Table 2, Appendix B). The biotite content has been drastically reduced in this sample, compared to clasts 1 and 2, and biotite was not detected during point counting (Table 3, Appendix C). Fe-oxides are observed in pores and along the crystal contact zones. The degree of weathering is low and can be classified as type 2 (Table 2, Appendix B), but the porosity reaching 2%, is secondary, and found in areas associated with feldspar dissolution (Tables 3 and 6, Appendix C). Category II dominates for both of the feldspars (Tables 4 and 5, Appendix C). The communication between the pores seems low, possibly giving the rock a low permeability. Micas, in the form of muscovite, are found to be partly dissolved and show signs of compression, but during point counting micas were almost not detected, and were found to be only 1% (Table 3, Appendix C). The clast, 1996.60, plots as granite in the Q-P-A diagram (black dot) (Figure 3.9). Point counting indicates a quartz content of 36%, where monocrystalline makes up 19%. The feldspars make up 58% of the sample, where plagioclase is the dominating with a content of 35% (Table 3, Appendix C).

Clast 6 (1995.40) (Figure 3.3 F) displays varied phenocrystal sizes; quartz and plagioclase have average very coarse (2 mm) sizes, while the K-feldspar has an average size of 0.25 mm (Table 2.1 and Table 2, Appendix B). The optical analysis reveals a low content of K-feldspar, only reaching 8% (Table 3, Appendix C). Dissolution can be observed especially in the plagioclase (category III dominated), but there are also indications of alteration of the K-feldspars, dominating category is I (Tables 4 and 5, Appendix C). Generally the degree of weathering is minimal, thus, this clast classifies as a type 2. Myrmekite, in association with the feldspars, have been observed (Table 2, Appendix B). The porosity is low in the sample, and was not detected during point counting, but optical analysis reveals only minor porosity, mostly associated with dissolved feldspars, making it secondary in origin. No communication has been observed between the pores, indicating very poor permeability in the clast. Fe-oxides can be observed in pores, constituting 1% of the sample (Table 3, Appendix C). Clast 6 plots as granodiorite in the Q-P-A diagram (purple dot) (Figure 3.9). 42% of the sample is found to be quartz by point counting, where polycrystalline dominates. The total feldspar content is found to be 39%, where plagioclase dominates. The micas make up 18% of the sample, where muscovite/illite dominates with 16%, and is found in association with altered feldspars (Table 3, Appendix C).

Clast 8 (1991.55) (Figure 3.3 G) consists of phenocrystals with an average crystal size between 1.1 mm to 1.3 mm (Table 2, Appendix B) (very coarse to coarse (Table 2.1)). There is a clear and sharp boundary in the thin section, separating the basement clast from the adjacent conglomeratic matrix. The feldspar in this sample is mostly plagioclase, reaching 17%, and the crystals have a larger average size than quartz. The clast is rich in biotite, reaching 19%, and clay minerals makes up 30% (Table 3, Appendix C). Biotites show signs of disintegration, and the clay minerals are often found together with the biotite. The clast displays a porosity of 2% (Table 3, Appendix C). The porosity is found inside the dissolved feldspars, thus giving it a secondary origin (Table 6, Appendix C), and there is observed little to no communication between the pores, the clast consequently most likely have low permeabilities. The large feldspar crystals are heavily dissolved, where category V dominates for both the feldspars (Tables 4 and 5, Appendix C), and sericite are found inside the feldspars. In the matrix part, the porosity increases, due to better connection and sorting between the grains. This basement clast stands out from the others, due to a higher content of clay minerals, as confirmed by point counting. It will be classified as a type 4 (Table 2,

Appendix B), and the clast plot as a granodiorite in the Q-P-A diagram (dark green dot) (Figure 3.9) The biotite shows no indication of a preferred orientation, and Fe-oxide coating has been observed on a few grains, but the amount of Fe-oxides is so small that it were not registered during point counting. The total quartz content is found to be 28 %, where monocrystalline makes up 15%. The total feldspar content is found to be 20%, and plagioclase dominates; making up 17% (Table 3, Appendix C).

Clast 9a (Figure 3.3 H) represents a green and coarse-grained basement clast. The clast, taken from a depth of 1976.30 m, shows indications of weathering, and it classifies as a type 3 (Table 2, Appendix B). Category II is the dominating feldspar preservation group for the feldspars, but high percentages can also be found in categories III and IV for plagioclase (Tables 4 and 5, Appendix C). The dissolution of feldspars seems to be occurring both in central parts of the crystals and randomly spread in the crystals, but the dissolution found in the central parts is the dominating type. Kaolinite and possibly illite, is found to be pore filling. Illite can be observed inside cracks, resembling sericitization. The clay mineral content is found to be 11% by point counting (Table 3, Appendix C), and was often found in association with altered feldspar. Chlorite, and biotite are making up 1 and 3% of the sample respectively (Table 3, Appendix C), and the biotite show indications of varying alteration. There was also observed Fe-oxide in relation with the biotite, but the content is so low, that point counting did not register it. Carbonate cement, making up 3% (Table 3, Appendix C), were found to be located inside the pores associated with the dissolved feldspar grains. The phenocrystals were quite large in this sample, ranging from 2.53–4.39 mm (granule-pebble (Table 2.1)) (Table 2, Appendix B), where K-feldspar crystals were found to be the largest. Clast 9a plot as granite in the Q-P-A diagram (light blue dot) (Figure 3.9). The quartz content was found to be 35%, where monocrystalline dominates and constitute 26%. The feldspar content is 49%, where plagioclase makes up 29%. The porosity is so low that point counting missed it (Table 3, Appendix C).

Clast 9b (Figure 3.3 I) with visual signs of weathering, was taken from a depth of 1994.90 m. The thin section does not only contain a basement clast, a sandstone from facies 2 is also present. The separation between the two is sharp and clear, even though the basement clast has a gradual change from phenocrystals to clays towards the edge of the basement clast, representing the weathering zone. The basement clast is coarse grained, where phenocrystals range between 2–3 mm (granule (Table 2.1)). The clast 9b from 1994.90 will classify as a

strong type 3 (Table 2, Appendix B). Nearly all phenocrystals show signs of alteration, compared to clast 9a where the feldspars show a lower alteration. The plagioclase crystals are heavily altered, and the twins are almost gone on all plagioclase phenocrystals found in clast 9b. A few K-feldspar and quartz crystals were not altered at all. Fe-oxides were found inside micro cracks, and sparry calcite cement, was observed. The calcite cement was observed to be located within the dissolved feldspars. Clay minerals were found to be pore filling, and the amount of clay increased towards the edge of the basement clast, where the weathering zone is visible.

The sandstone (2) was found to have an average grain size of medium sand (0.25-0.5 mm (Table 2.1)), and the grains ranged between angular to sub-rounded. The sandstone was moderately sorted, and the rock framework is grain supported (Table 1, Appendix B), dominated by straight contacts. The degree of compaction is minor, and quartz was found to be the dominating grain type. The degree of alteration on feldspars varied, from unaltered to slightly altered, and plagioclase showed the highest degree of alteration. The K-feldspar grains are larger and less rounded compared to the plagioclase grains. Clastic micas, biotite and muscovite, are observed. Clay is present in the sandstone as pore fill, likely reducing the porosity and permeability. Sparry calcite cement was observed in the sandstone, and the crystals were mostly euhedral, and fragments of clay could be observed at the edges of the calcite.

The conglomeratic matrixes

The conglomeratic matrixes contain mostly angular to sub-rounded grains, and the sorting ranges from poorly sorted to very poorly sorted. The grain size varies from very coarse sand to medium sand (2.0-0.25 mm (Table 2.1)); with coarse sand as the average grain size (Table 1, Appendix B). The average grain size is increased due to presence of rock fragments, and the rock fragments are responsible for the poorly sorting found in these samples. The red matrix has the highest abundance of rock fragments of igneous origin, which were by point counting, found to reach 23%, while the grey had 18% and the green 9% (Table 3, Appendix C). The matrixes are grain supported, but there are a high content of pore filling clays between the grains, reaching an average of 14% (Table 3, Appendix C). The porosity in the matrixes has by point counting, found to range between 2 and 4%, where the red and the green has been found to have the highest porosity (Table 3, Appendix C). The porosity is found to be dominantly primary in origin, but secondary porosity, associated with dissolved

feldspars, has been observed in the red and grey matrix (Table 6, Appendix C). The presence of clay minerals in the pore space, reduce the communication between pores, hence the permeability is expected to be poor. The grain contacts are mostly straight and tangential, and the matrixes show a low degree of compaction. The average quartz content is, by point counting, found to be approximately 34%. Monocrystalline quartz dominates in the green and grey matrix, while in the red matrix, polycrystalline dominates. The feldspar content was found to be 14% in the red matrix (Table 3, Appendix C), but a high content of feldspar were to be found in the rock fragments present in the sample (Table 7, Appendix C), and these feldspars were counted as rock fragments. Of the 93 counted rock fragments in the red matrix, 63% were found to be represented by feldspar (Table 7, Appendix C). The average plagioclase content in the matrixes was found to be 10%, while the average K-feldspar content was 10% (Table 3, Appendix C). The relationship between the two feldspars was almost 50/50 in all the matrix samples, which were counted.

Considering the preservation of feldspar in matrix samples studied, some differences were observed during point counting. The red matrix had the strongest altered feldspars, where the dominating K-feldspar category was II and plagioclase was dominated by categories III and IV (Tables 4 and 5, Appendix C). The grey and the green matrix showed the same trend, where K-feldspar was dominated by category I, while plagioclase by category II (Tables 4 and 5, Appendix C). The carbonate content was comparable, and the average content was found to be 7% (Table 3, Appendix C). Fe-oxides were only registered in the red matrix, making up 7%. The mica content was quite similar in the three matrixes, averaging 3% (Table 3, Appendix C). Rock fragments in the red matrix had a high feldspar content, and a quartz/total feldspar were calculated, with the results from point counting. This ratio will be compared to the quartz/total feldspar provided by XRD analyses, to observe if there are differences. The quartz/total feldspar from point counting was found to be 2. Polycrystalline quartz fragments were found in all three matrixes, but they were most abundant in the red matrix, where they constituted 11% of the counted quartz. In the grey and green, the same fragments only made up 1 and 2% respectively (Table 9, Appendix C). Overgrowths have been observed in all matrixes, with quartz overgrowth found in both the grey and the green, while K-feldspar overgrowth has been recognized in the red and green (Table 8, Appendix C) (Figure 3.12 C-D).

There are two types of clays present in the matrixes; one where feldspars have been dissolved, and the other as pore filling clays in between unaltered grains. The green matrix has a high content of clay in the pore space. Biotite grains found in the green matrix show signs of dissolution, and clays are filling up the pore space between the biotite cleavages. The grey matrix has pore filling kaolinite, while the red matrix seems to have the lowest content of clays, observed during optical microscopy. Clastic chlorite has been observed in all matrixes during optical analyses.

Three phases of Fe-oxides were observed in the red matrix, occurring as grain coating, pore fill and within micro cracks. In the red matrix (1982.90), the first Fe-oxide phase is recognized as grain coatings where small grains are fully coated, while larger grains are only partly coated (Figure 3.11 A). The second Fe-oxide phase is recognized in areas where no Fe-oxides can be observed along grain contacts (Figure 3.11 B), and the Fe-oxide act as pore fill and pore lining/rim. The third Fe-oxide phase is found to fill micro cracks present in the rock fragments. The grey and green matrixes are found to have micro cracks (third Fe-oxide phase), clearly oxidised by iron, while no Fe-oxide coating or pore fill have been observed within these matrixes. In the sample from 1998.30 m depth, the grey, red, and green matrix can be observed together. No clear boundary between the red matrix and the other two has been observed, and no Fe-oxide is found in the contact zone between grains. The Fe-oxides occur in better sorted zones in the red matrix compared to the grey and green matrix. It appears to be a lower clay content in the red matrix compared to the other two matrixes, where clay minerals are found as pore fill. The

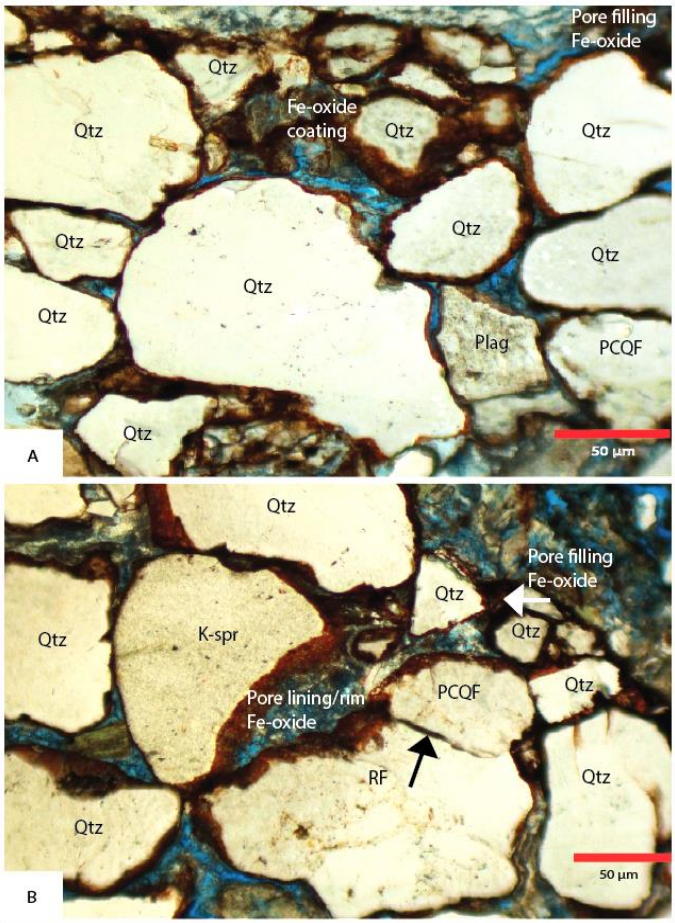

Figure 3.11: The Figure shows two of the Fe-oxide phases found in the red matrix. Figure A shows the first phase, where smaller grains are fully coated, while larger grains are only partly covered. Figure B shows the second phase, where the Fe-oxides are to be found as pore fill (white arrow) and as pore lining/rim, and as observed, the Fe-oxide is not found in grain contact zones (black arrow). Both Figures are from sample 1982.90. RF = rock fragment. Qtz = quartz. Plag = plagioclase. K-spr = K-feldspar. PCQF = polycrystalline quartz fragment.

analysed sample from 1983.20 m depth represents a transition zone between red and green matrix, and the transition is sharp and can easily be traced in the thin section. In the areas of red matrix, Fe-oxides are acting as coatings, pore fill, pore lining/rim and as fill in micro cracks. Fe-oxides are found to be present along grain contacts. The green matrix has a higher clay content between grains, and the red matrix appear to be better sorted at this depth interval.

Authigenic K-feldspar overgrowth has been observed on detrital K-feldspar grains. There is sparry carbonate cement in between the grains, which is observed in all the different matrixes. The carbonate cement is found to have euhedral shapes, and it was observed fragments of clay minerals at the carbonate grain edges (Figure 3.12 A-B). The carbonate cement was found to grow on the K-feldspar overgrowth (Figure 3.12 C-D).

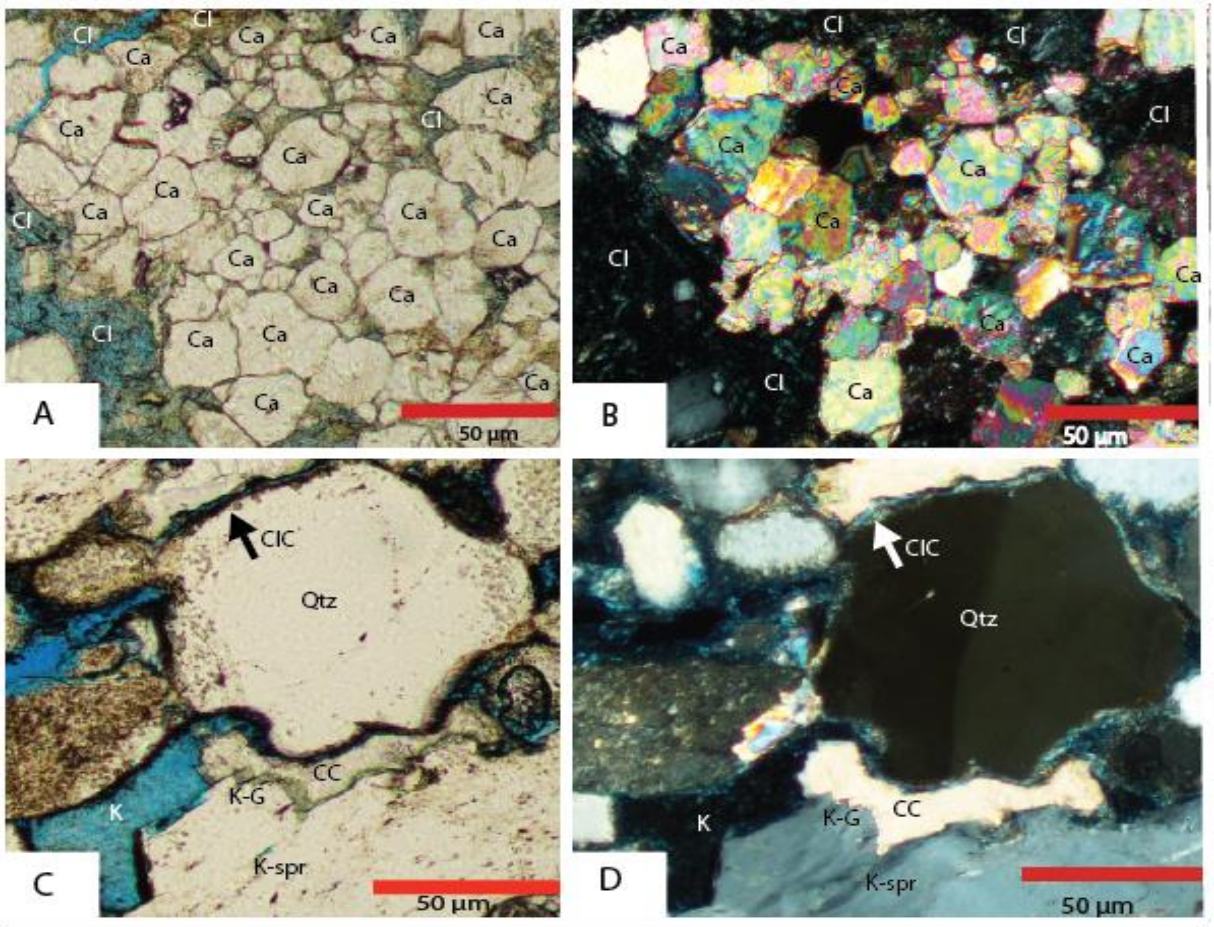

Figure 3.12: Figure A shows the common relationship between euhedral, sparry calcite (Ca) and clay (Cl) in plan polarized light. Figure B shows the same as in A, but in cross-polarized light. Figures A and B are taken from sample 1974.80. Figures C and D show the presence of a clay coating (ClC) around a quartz grain, pore filling kaolinite (K), calcite cement (CC), and a K-feldspar overgrowth (K-G) below the calcite cement. Figures C and D are taken from sample 1995.65.

Polycrystalline quartz fragments are observed in all the matrixes (Table 9, Appendix C), and these grains appear to be more rounded and have smaller grain size, compared to the other grains found in these samples.

Analyse of a sandstone representing facies 2

The sample, taken from a depth of 1983.40 m, represents the grain-supported sandstones (facies 2) found in between the conglomeratic sequences in the lowermost part of core 16/1-13 (Figure 3.1). Sand grains are sub-angular to sub-rounded, with an average size of fine to medium sand (0.125-0.5 mm (Table 2.1)). The sandstone is very well to well sorted (Table 1, Appendix B). The porosity is 10%, where all is found to be of primary origin (Tables 3 and 6, Appendix C), and there is relatively good contact between the pores. The clay mineral content is by point counting found to be 6% (Table 3, Appendix C). The porosity is higher in the sandstone, compared to the matrixes. The grain contacts are straight and tangential, reflecting a low degree of compaction. In addition to pore filling clays, there is also euhedral carbonate cement (up to 7% (Table 3, Appendix C)) found in between the grains. The plagioclase grains showed the highest degree of alteration, where categories II and III dominated, while the K-feldspar preservation was dominated by category I (Tables 4 and 5, Appendix C). The sandstone sample was, by point counting, found to have a quartz content of 63%, where monocrystalline quartz dominated. The sample was found to have a low feldspar content, constituting only 12% of the sample, where plagioclase was found to have the highest percentage (Table 3, Appendix C). Authigenic K-feldspar overgrowth was observed (Table 8, Appendix C).

FA 2

Four thin sections were studied from FA 2. Point counting was executed on samples 1959.65 and 1959.20 (Table 3, Appendix C). The thin sections represent parallel laminated (facies 5) and cross-bedded sandstones (facies 6). The sand grains are of sub-angular to sub-rounded shape, with an average size ranging from medium to fine sand. The sorting of the samples ranges from moderate to very well sorted (Table 1, Appendix B). The grain contacts are mostly straight and tangential, reflecting a low degree of compaction. The sandstone samples are grain supported, and framework grains, quartz and feldspar, made up on average 54 and 11% respectively (Table 3, Appendix C). The porosity ranges from around 19 to 9% (Table 3, Appendix C), and there is good communication between the open pore space. The porosity is found to be dominantly of primary origin, but in a few areas, a secondary origin is found,

often associated with dissolved feldspar and rock fragments (Table 6, Appendix C). Hence, these rocks likely have a good permeability. The secondary porosity, derived from the dissolution of feldspar grains and rock fragments, were mostly filled with authigenic kaolinite, which were large enough to be recognized during optical microscopy. In the medium grained sandstone (1959.65), pore filling kaolinite was found to reduce the porosity (Figure 3.13 C). The clay minerals were found to constitute 16% of the medium sandstone, while in the fine sandstone, only 3% clay minerals have been recognized (Table 3, Appendix C).

The alteration of feldspars is dominated by categories II and V, for plagioclase, in the fine and medium sandstone respectively (Table 4, Appendix C). Further, K-feldspar was found to be more altered in the fine sandstone, dominated by category II, while in the medium sandstone, category I dominated (Table 5, Appendix C). Polycrystalline quartz fragments are found in these sandstones, making up on average 12.5% of the counted quartz (Table 9, Appendix C). These polycrystalline quartz fragments are often found to be more rounded and have a smaller size than the other grains found in the samples. The polycrystalline quartz appears to be both of gneissic and volcanic origin, based on the grain configuration. Observation of

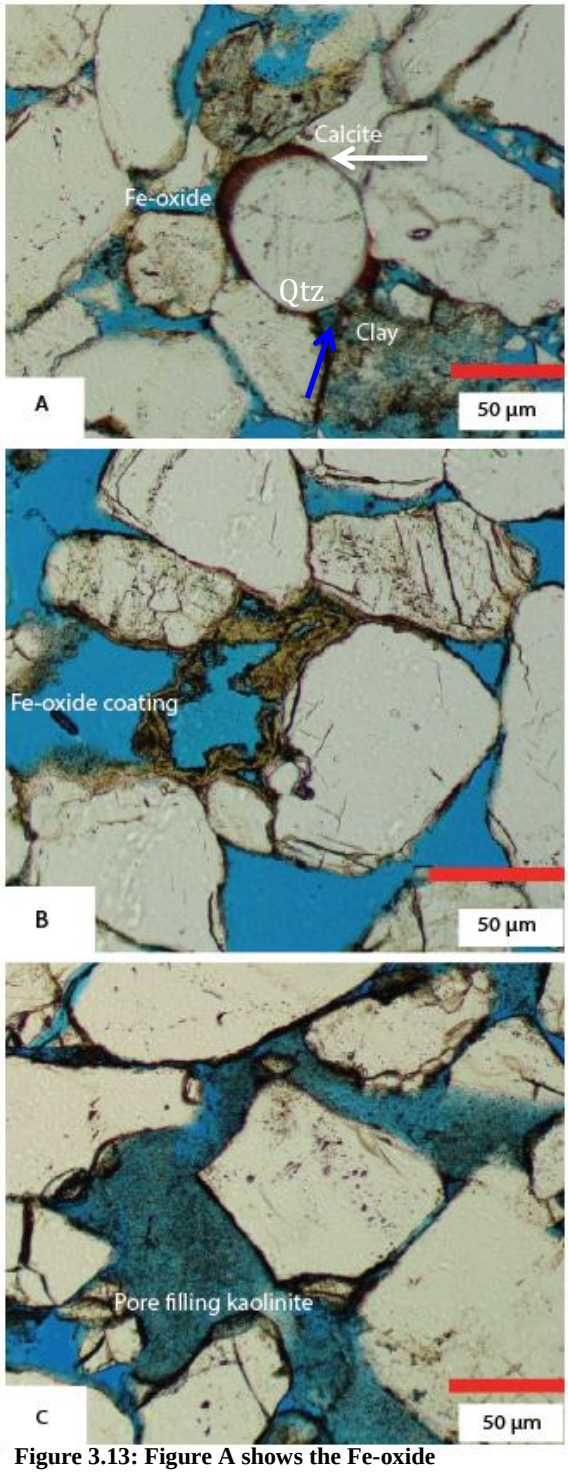

Figure 3.13: Figure A shows the Fe-oxide overgrowth observed in sample 1959.20. Notice the relationship between the overgrowth and the calcite cement and the pore filling clay, where the calcite grows onto the Fe- oxide overgrowth (marked with white arrow) and the Fe- oxide overgrowth does not grow in areas where pore-filling clay are present along the grain contact (marked with blue arrow). Figure B shows a Fe-oxide coating from sample 1959.20. The coated grain has been dissolved, and only the coating is remaining. Figure C displays the pore filling kaolinite found in the medium grained sandstones. Kaolinite has reduced the porosity in the sample (1959.65).

individual laminae found to be upwards coarsening, can be observed in three of the four thin sections, taken from medium grained (0.25-0.5 mm) sandstone intervals in the core. Fe-oxides have been observed in the thin sections, but the total amount reaches only 1% (Table 3, Appendix C). The Fe-oxides are found as coatings, appearing to have a yellowish colour (Figure 3.13 B). As Figure 3.13 B displays, the coated detrital grain has been dissolved, and only the Fe-oxide coating is remaining. Overgrowth of red Fe-oxides has also been observed (Figure 3.13 A), and K-feldspar overgrowth has been observed (Table 8, Appendix C). Euhedral sparry carbonate cement has been observed in all four thin sections, and constitute on average 10% (Table 3, Appendix C). No relation can be found between the Fe-oxide overgrowth and the K-feldspar overgrowth, since they have not been observed together. The sparry calcite has been found to grow onto both types of overgrowths e.g. Fe- oxide overgrowth in Figure 3.13 A (white arrow). As displayed in Figure 3.13 A, the Fe-oxide overgrowth does not grow on the detrital grain quartz grain where pore filling clay appears (blue arrow). Clastic biotite and muscovite have been observed in the medium grained sandstone, where they together constitute 3% (Table 3, Appendix C).

3.2.2 XRD results

A total of 17 XRD diffractograms were analysed. The results are plotted as XRD% in Figure 3.14. The detailed results from the XRD bulk analysis can be viewed in appendix D.

FA 1

The basement clasts

The basement clasts from FA 1 conglomerates are dominated by quartz, plagioclase and K-feldspar. These minerals constitute on average 23 XRD%, 42 XRD%, and 22 XRD% respectively (Table 10, Appendix D). When considering the clay minerals, chlorite and kaolinite make up on average 3 XRD% and 2 XRD% respectively (Table 10, Appendix D). Muscovite/illite and biotite, represent the micas in these samples, and both constitute on average 3 XRD% (Table 10, Appendix D). No chlorite was found in clast 5 (1996.60) and no kaolinite was found in clasts 4 (1999.45) and 5 (1996.60) respectively (Table 10, Appendix D). The remaining XRD% is made up by calcite, with an average value of 1 XRD%. Calcite was not detected in clast 6 (1995.40) (Table 10, Appendix D). Traces of hematite have been detected in all basement samples (Table 10, Appendix D).

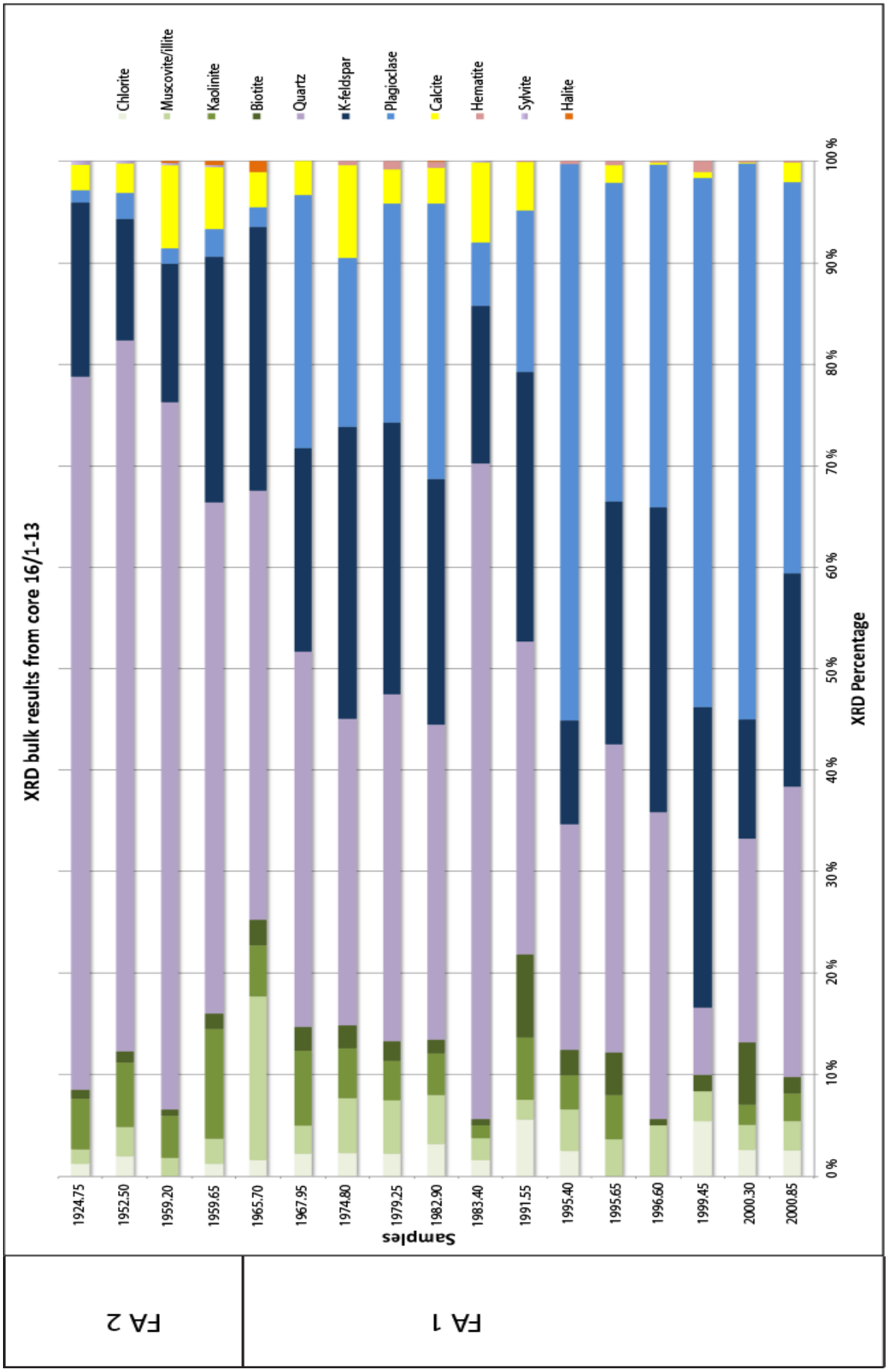

Figure 3.14: The XRD bulk results from core 16/1-13. With corresponding legend to the right, and the related facies association to the left

The conglomeratic matrixes

In the samples taken from the conglomeratic matrixes, quartz, plagioclase, and K-feldspar make up the most common mineral groups based on XRD% (Table 10, Appendix D). Quartz is the dominant mineral, and constitute on average 32 XRD% (Table 11, Appendix D). Plagioclase and K-feldspar both make up on average 24 XRD% (Table 11, Appendix D). The clay minerals chlorite and kaolinite, constitute on average 2 and 6 XRD% respectively (Table 11, Appendix D). Chlorite is not found in the grey matrix at a depth of 1995.65 m (Table 10, Appendix D). Muscovite/illite and biotite make up 4 and 2 XRD% (Table 11, Appendix D). Calcite is present in every sample analysed, and makes up an average of 4 XRD% (Table 11, Appendix D). Traces of halite and hematite are present (Table 10, Appendix D).

Sandstone of facies 2 and claystone of facies 4

The sandstone (1983.40) and claystone (1965.70) samples from FA 1, are rich in quartz, making up 65 and 42 XRD% respectively (Table 10, Appendix D). In the sandstone sample (1983.40), plagioclase and K-feldspar make up 6 and 16 XRD% (Table 10, Appendix D). In the claystone sample (1965.70) the same minerals constitute 2 and 26 XRD% respectively (Table 10, Appendix D). Kaolinite and chlorite are present in both samples, and make up 1 and 2 XRD% in the sandstone sample, and 5 and 2 XRD% in the claystone sample (Table 10, Appendix D). Biotite and muscovite/illite are found in both samples, and constitute 0.6 and 2 XRD% in the sandstone sample, and 3 and 16 XRD% in the claystone sample (Table 10, Appendix D). Calcite is present in both samples, and constitute 8 XRD% in the sandstone sample and 3 XRD% in the claystone sample (Table 10, Appendix D). Traces of sylvite is present in the sandstone, and makes up 0.1 XRD%, while halite is only found in the claystone, and makes up 1 XRD% (Table 10, Appendix D).

Quartz/total feldspar for FA 1 samples

The average quartz/total feldspar in the matrixes is 0.6. In the sandstone sample the ratio is 3.0 and in the claystone sample, the same ratio is calculated to be 1.5. The quartz/total feldspar for the individual samples can be observed in Figure 3.15.

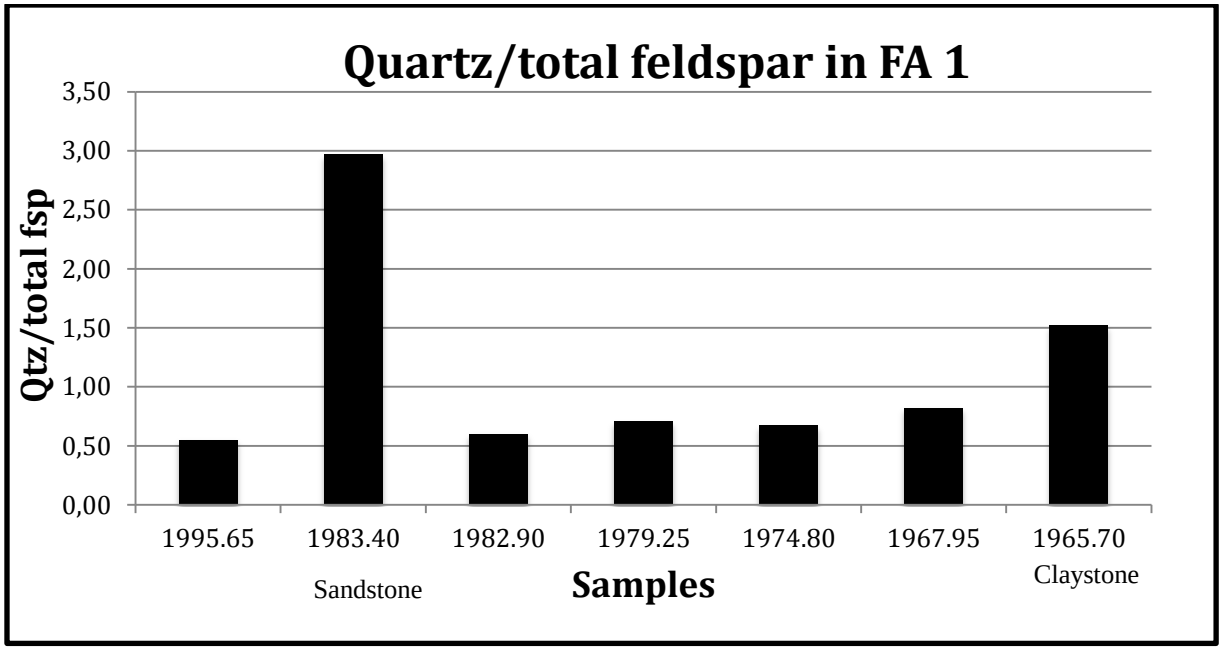

Figure 3.15: Quartz/total feldspar based on XRD analyses of the FA 1 samples of 16/1-13.

FA 2

The samples taken from this facies association is dominated by quartz. The average quartz content is 65 XRD%, and XRD results show a general upward increase in quartz content (Table 10, Appendix D). The plagioclase content is severely reduced in FA 2, compared to FA 1. There is also a gradual decrease in plagioclase content upwards in FA 2, where the percentage is reduced from 3 XRD% (1959.65 m) to 1 XRD% (1924.75 m) (Table 10, Appendix D). The average plagioclase content is 2 XRD% in FA 2 (Table 10, Appendix D). The K-feldspar shows variations, and the content is reduced going up stratigraphy, but the K-feldspar content is not as drastically reduced, as compared with the results found in FA 1. The average K-feldspar content is 17 XRD% (Table 10, Appendix D).

Clay minerals and phyllosilicates, such as chlorite, kaolinite, biotite, and muscovite/illite are found in all samples from FA 2, expect for chlorite, which is not found in sample 1959.20 m (Table 10, Appendix D). Kaolinite is the most abundant clay mineral present, with an average XRD% of 7 (Table 10, Appendix D). The kaolinite content is higher in the medium grained sandstones (Table 10, Appendix D). The chlorite content averages 1 XRD%, and appear to be quite stable (Table 10, Appendix D). The biotite and muscovite/illite content, constituting the micas, have an average XRD% of respectively 1 and 2 (Table 10, Appendix D). There is no clear trend observed in the biotite content, but the muscovite/illite content is reduced upwards.

Calcite constitute an average of 5 XRD% of the samples taken from FA 2 (Table 10, Appendix D). There is a gradual decrease in calcite content upwards. Traces of salts, in the form of sylvite (KCl) and halite (NaCl), are present in nearly all samples taken from FA 2 (Table 10, Appendix D). No hematite was to be found in FA 2.

The average quartz/total feldspar from all the samples found in FA 2, are 3.5. The quartz/total feldspar for the individual samples can be observed in Figure 3.16.

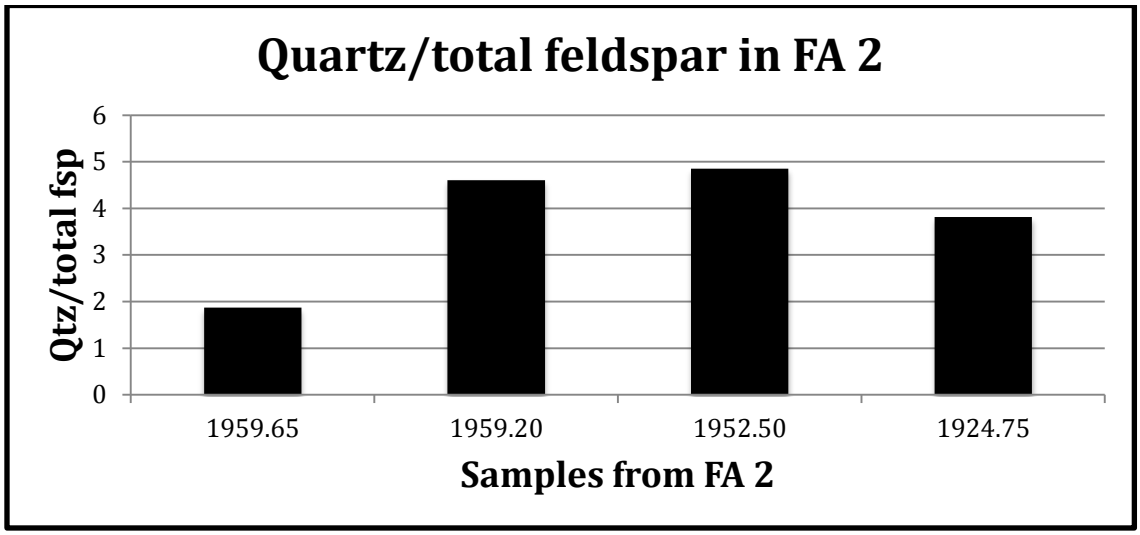

Figure 3.16: Quartz/total feldspar based on XRD analyses of the FA 2 samples of 16/1-13.

3.2.3 Scanning electron microscope (SEM) and electron microprobe (EMP) results

During the SEM studies, a total of 15 thin sections and 5 stubs were analysed. From the thin sections, seven basement clasts and five matrix samples from FA 1 were analysed and one sandstone sample from FA 2, representing the medium grained sandstone (1959.65) was analysed. Samples from the three different matrixes (FA 1), and two sandstone samples (FA 2) (1924.75 and 1959.20) were chosen for further SEM studies by using stubs.

Five thin sections were chosen for additional electron microprobe (EMP) analyses. Four of the thin sections were from core 16/1-13, but one additional sample was derived from core 16/1-15, a nearby core from the Edvard Grieg Field (Figure 1.2), containing basement. The basement sample (16/1-15) represents level 1974.35 meter. This thin section was kindly provided by PhD student Lars Riber (UiO). EMP results are to be found in appendix E.

SEM

FA 1

The basement clasts

Five of the seven basement clasts analysed by SEM, were found to have relatively low clay mineral content, while clasts 8 and 9b were enriched (Table 3.3). The clay minerals found in these samples were mostly kaolinite, located inside the voids in feldspars, especially in plagioclase grains. All the analysed basement clasts were found to contain euhedral, sparry calcite (Table 3.3). The kaolinite displayed booklet structures with varying sizes. Chlorite, illite-smectite, and smectite, were also found to be pore filling. Clast 8 (1991.55) have a higher clay mineral content than the other clasts, and showed the presence of two different types of kaolinites, one forming well-developed booklet structures and one appearing as a more dense homogenous mass, containing minor fragments of K-feldspar (Figure 3.18 A). During SEM analyses, clast 4 (1999.45) was found to contain rhombic dolomite crystals (Figure 3.17 and Table 3.3).

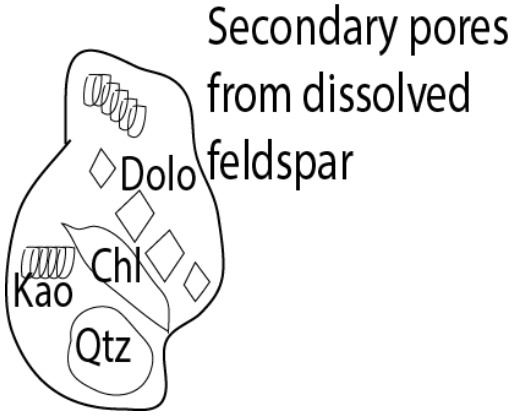

Figure 3.17: A schematic illustration of the rhombic dolomite (Dolo) observed in a secondary pore in sample 1999.45 during SEM. Kaolinite booklets (Kao), quartz fragments (Qtz), Chlorite fragments (Chl) were also observed in the same pore.

Sample 1994.90 show both clast 9b with visible weathering and a facies 2 sandstone. The sample was found to be rich in smectitic clay, with additional content of chlorite, illite and kaolinite. The smectite was found to have two types of appearances (Figure 3.18 B), but with SEM analyses, the only difference between the crystalline smectite and the massive smectite, were decreasing K and Al contents. Euhedral, sparry calcite was also observed (Table 3.3), where smectite remnants could be observed at the edges of the calcite. The kaolinite was found to appear as well-developed booklets. A higher content of clay minerals could be observed along the highly weathered part of the basement clast, but as the degree of weathering decreased towards the centre of the basement clast, the clay mineral content was reduced.

Table 3.3: Results from the SEM analyses of basement clasts, considering the amount of clay mineral content and presence of calcite and dolomite.

Sample	Depth level	Clay content	Euhedral, sparry calcite	Rhombic dolomite
1	2000.85	Low	Yes	No
2	2000.30	Low	Yes	No
4	1999.45	Low	Yes	Yes
5	1996.60	Low	Yes	No
6	1995.40	Low	Yes	No
8	1991.55	High	Yes	No
9b	1994.90	High	Yes	No

The conglomeratic matrixes

The matrix samples were all studied in the SEM. All five matrix samples from thin sections, and three matrixes were studied as stubs. The analyses preformed during SEM, reveal the presence of different clay minerals. Kaolinite, illite, illite-smectite, smectite, and chlorite were observed in the matrix samples. The clay minerals are present both as coatings and as pore fill (Figures 3.18 C-F). The kaolinites were found to have both well-developed booklet structures and non-booklet structures, showing sign of cracks and displacement of the hexagonal plates. The non-booklet kaolinite shaped kaolinites are observed to be remnants of earlier well-developed kaolinites booklets, since there is a presence of randomly distributed authigenic kaolinites in the same areas as the non-booklet kaolinites are observed. The kaolinites appeared to be related to dissolved feldspar grains, since they were often observed in voids found inside dissolved feldspar grains. The size of the kaolinites hexagonal plates varied and the diameter ranged from around 5 μm to 10 μm. The kaolinite was observed to displace smectitic clay (Figure 3.19 E). The authigenic chlorite clay observed during SEM, is found to contain both Mg and Fe.

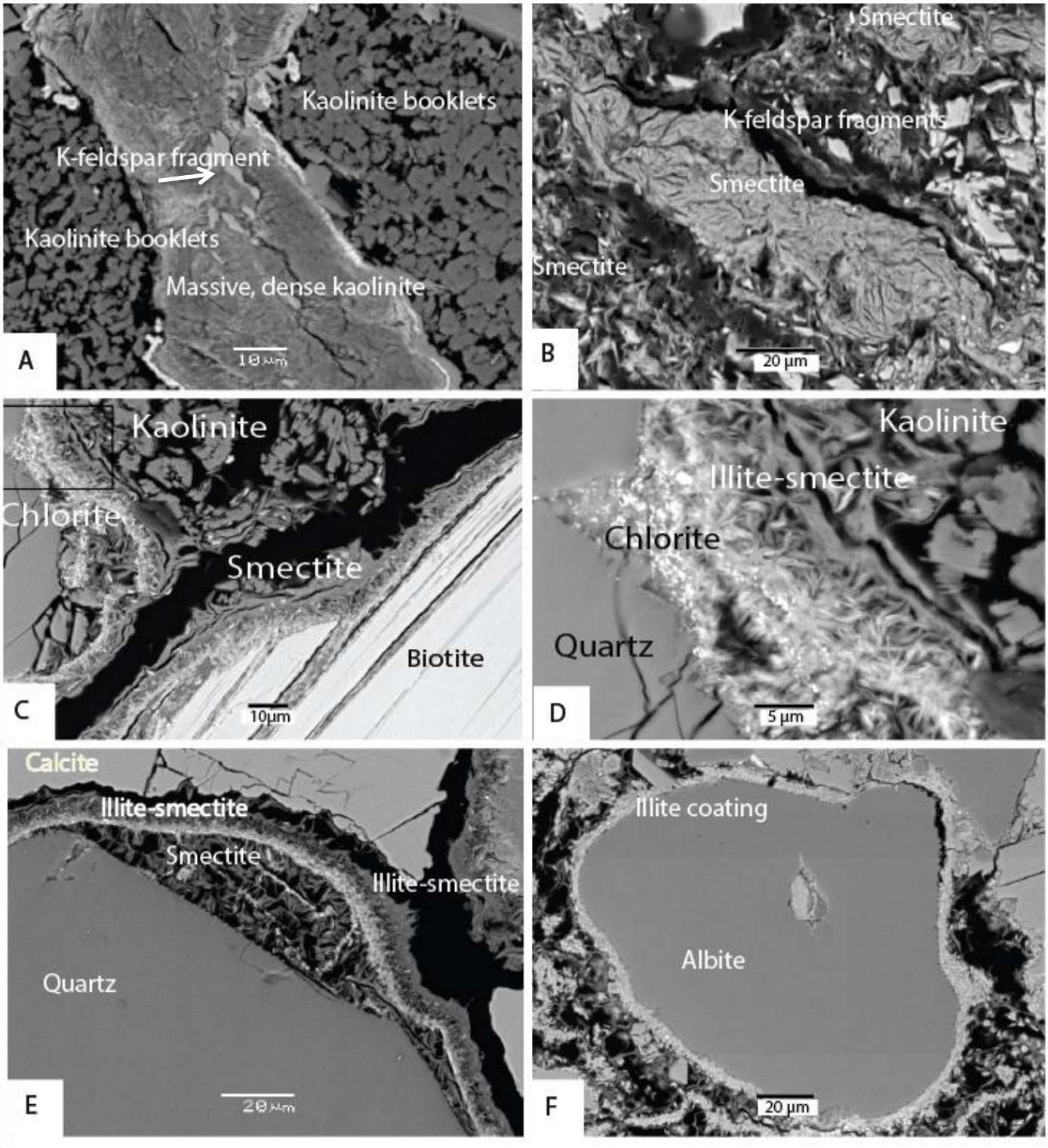

Figure 3.18: A) The two different types of kaolinites found in clast 8 (1991.55), one type forming well-developed booklets and one type appearing more as a solid mass, containing K-feldspar fragments (white arrow). B) shows the presence of two types of smectites, where analyses indicate that the only mineralogical difference is a reduction in Al and K content. Taken from sample 1994.90. C-D) the different coatings found during SEM analyses. Notice the presence of chlorite, smectite, illite-smectite and kaolinite. The square in Figure C, shows the location of Figure D. Figures C and D are taken from 1982.90. E-F) two different types of coating observed during SEM analyses. Figure E represents an illite-smectite coating together with smectite, while Figure F shows an excellent illite coating. Figure E derives from sample 1982.90, while Figure F derives from sample 1979.25.

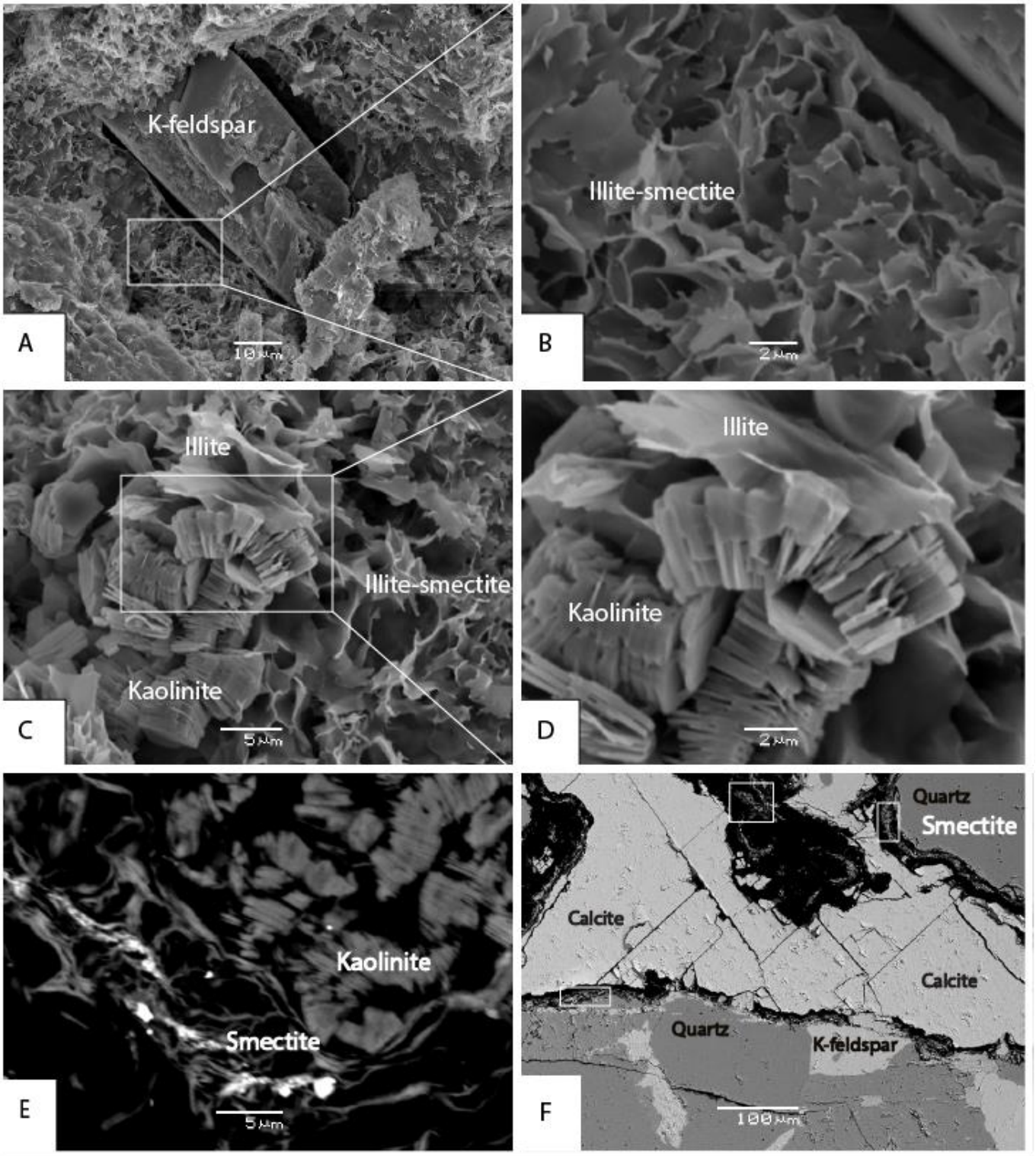

Figure 3.19: A–B) Mixed layer illite-smectite pore fill and coatings. Observe the honeycomb shaped crystals, with random orientation. Taken from sample 1995.65. C-D). Flaky illite draped around a kaolinite booklet. Taken from sample 1982.90. Figure E shows the presence of booklet kaolinites and smectite. The kaolinite booklets seem to have displaced the smectite, by growth in the open pore space, leading to bending of the smectite structures. The smectite structure has been deformed by the push from the growing kaolinite. Figure F shows the presence of smectite and calcite cement. The white squares indicate areas of smectite. Notice how the calcite grows outside the smectite rich areas. Both E and F are taken from sample 1998.30.

Smectite and illite-smectite were found to be, together with kaolinite, the dominating clay minerals in the matrix samples. Both clay minerals were found to have a honeycomb-like appearance, with a random orientation, often found to curl away from the detrital grain surface. Both clay minerals acted as coating and pore fill (Figure 3.19 A-B). During SEM analyses, flaky illite crystals were found to drape around kaolinite booklets (Figure 3.19 C-D). Chlorite appeared to have rosette like crystal shapes, with random orientation. The chlorite was often observed in association with dissolved biotite grains (Figure 3.20)

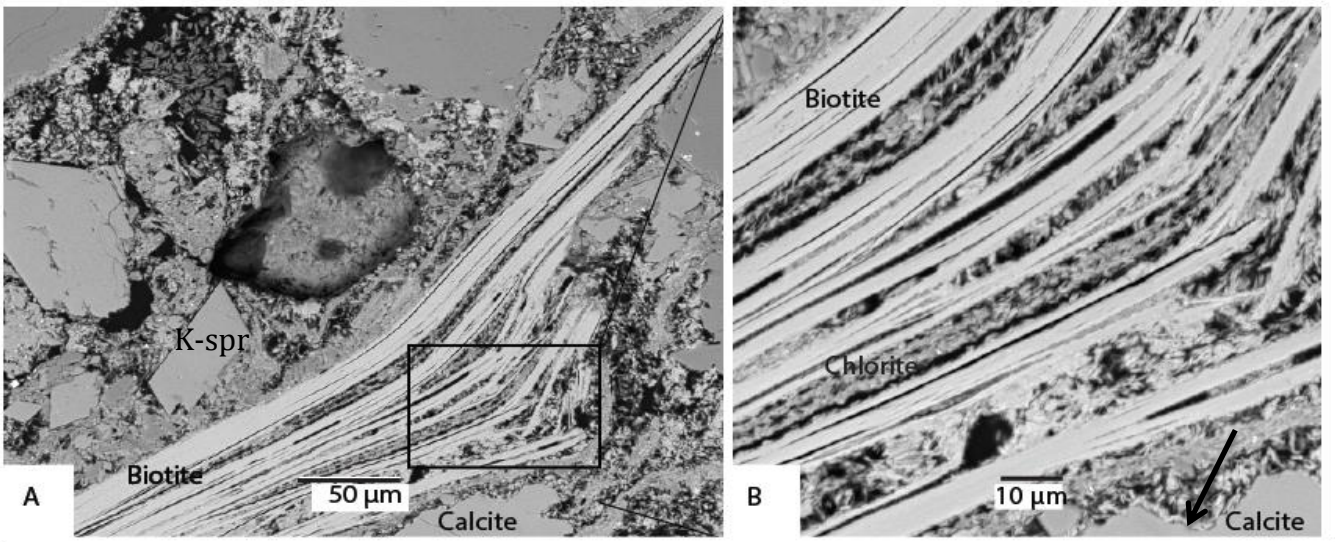

Figure 3.20: A) a dissolved clastic biotite where chlorite is precipitated between the dissolved biotite cleavages. The black square indicates the location of Figure B. B) Close-up SEM photo of the pore-filling chlorite. Notice also the euhedral shape of the calcite in the bottom right corner (marked by black arrow). Both Figures are taken from sample 1974.80.

The clay minerals found in the three different matrixes appear to be roughly the same, based on the mineralogical composition deriving from the SEM spectre during the analyses. Fe-oxide coatings, as observed in the red matrix, were found to be hematite. Euhedral sparry calcite cement is observed in all the matrix samples (Figure 3.19 F), but mostly during the thin section analyses. Rhombic dolomite cement has been observed in the sample representing a depth of 1998.30 m. The dolomite can be observed in association with authigenic chlorite, acting both as coating and as pore fill. Remnants of chlorite can be observed at the edge of the euhedral, rhombic dolomite.

Feldspar dissolution, especially plagioclase grains, has been observed in all of the samples. There has also been observed authigenic K-feldspar overgrowth on detrital K-feldspar grains.

FA 2

Three sandstone samples of FA 2 were studied in the SEM; 1924.75 and 1959.65 representing the medium grained sandstones, while 1959.20 represents the fine grained sandstone.

Only stubs were used for the study of the fine sandstone sample, and SEM reveals the presence of kaolinite and euhedral sparry calcite cement. The kaolinite found in this sample has well-developed booklet structure and they are pore filling (Figure 3.21).

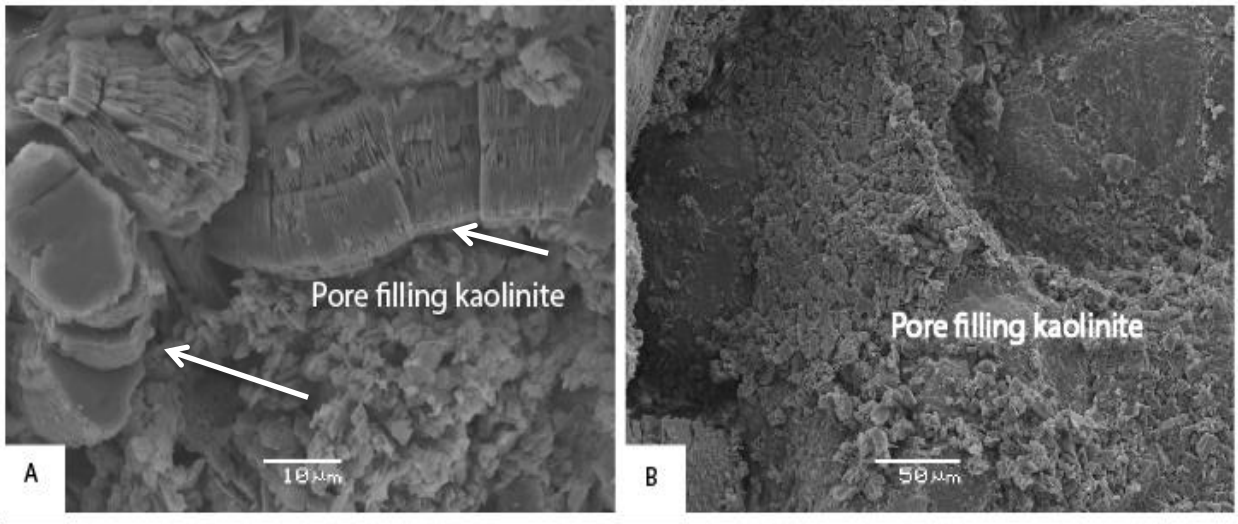

Figure 3.21: Figure A shows kaolinites with well-developed, pore filling booklets. Notice the influence from compaction by deformation of the kaolinite booklets (white arrows) in Figure A. The hexagonal plates are around 20 µm in diameter. Figure A is from sample 1924.75. Figure B shows the pore filling kaolinite present in the fine sandstone (1959.20). The kaolinite booklets also act as coating.

The edges of the kaolinite booklets are sharp and well developed, but some booklets are deformed (white arrows in Figure 3.21 A). Kaolinite acted both as coating on detrital grains and as pore fill in the fine sandstone (Figure 3.21 B). Kaolinite, chlorite (rosette structure), illite, and illite-smectite (honeycomb-like appearance), were observed in the medium sandstone. The clays appear both as coating and pore fill. There are detrital grains having multiple layers of coating. The kaolinites found in the medium sandstones consist of hexagonal plate up to 20 µm in diameter, while the kaolinites found in the fine sandstone, display diameters of roughly 5 µm. The booklets found in the medium sandstones show indication of deformation, and are a little rougher along the edges than the kaolinite found in the fine sandstone. The authigenic chlorite clay observed in the sandstone samples is found to contain both Mg and Fe. The stub analyses showed the presence of dissolved feldspar grains and sparry calcite cement. The presence of dissolved grains was found to be higher in the

medium sandstone compared to the fine sandstone. There has been observed authigenic K-feldspar overgrowth and quartz overgrowth on respectively K-feldspar and quartz detrital grains.

Electron microprobe (EMP)

Samples representing depth levels 1924.75, 1967.95, 1983.40, and 1995.65 were analysed by EMP. These samples represent varied lithologies and facies found in core 16/1-13, and they are taken from different depth intervals for the purpose of screening provenance analysis. Basement sample (1974.35) from core 16/1-15, was also studied by EMP. 53 points were analysed and these points revealed a stable mineralogical composition of the K-feldspar, only minor variations could be observed. Three different types of K-feldspars were present in the samples, as revealed by variations in the Na, Ca, K and Ba content (Appendix E).

The K-feldspar overgrowth found in the samples was tested with EMP, to disclose elemental differences between the detrital grain and the authigenic overgrowth. The K-feldspar overgrowths were found to have a lower content of Na and Ba, and higher content of K (Table 3.4). A few results from the EMP analysis can be found in Table 3.4, additional results in Appendix E.

Table 3.4: 13 representative EMP analyses of detrital K-feldspar grains and authigenic K-feldspar overgrowths in wt%, from three chosen samples from core 16/1-13.

Analysed	Sample	SiO_2	Na_2O	Al_2O_3	CaO	FeO	MnO	K_2O	BaO	Total
1. Detrital grain	1967.95	65,0	1,1	18,8	0,0	0,1	0,0	15,6	0,4	100,9
2. Overgrowth	1967.95	64,8	0,0	18,5	0,0	0,0	0,0	17,0	0,1	100,3
3. Overgrowth	1967.95	65,2	0,1	18,9	-0,1	0,0	0,0	17,0	0,0	101,1
4. Detrital grain	1967.95	64,9	1,0	18,8	0,0	0,1	0,0	15,7	0,4	100,8
5. Overgrowth	1967.95	64,8	0,0	18,5	-0,1	0,0	-0,1	17,4	0,0	100,6
6. Overgrowth	1995.65	64,5	0,8	18,8	-0,1	0,1	0,0	15,5	0,9	100,5
7. Detrital grain	1995.65	65,2	0,8	18,7	-0,1	0,1	0,0	15,9	0,2	100,9
8. Overgrowth	1995.65	65,1	0,0	18,7	-0,1	0,1	0,0	17,1	0,0	100,9
9. Detrital grain	1995.65	64,2	0,6	18,8	-0,1	0,0	-0,1	15,9	0,8	100,3
10. Detrital grain	1924.75	65,0	0,5	18,6	-0,1	0,0	0,1	16,5	0,1	100,7
11. Overgrowth	1924.75	64,7	0,1	18,2	0,0	0,1	0,0	17,1	0	100,1
12. Overgrowth	1924.75	64,9	0,0	18,3	-0,1	0,0	0,0	17,0	0,0	100,1
13. Detrital grain	1924.75	64,2	0,8	18,2	0,0	0,1	0,0	15,8	0,2	99,3

4. Discussion

4.1 Reconstruction of the depositional environment

The Edvard Grieg Field, in this master thesis is represented by core 16/1-13, containing Permo-Triassic and Early Cretaceous formations. The half graben, where the field is located, must have developed during the first rift phase that occurred in the northern North Sea, at the transition between the Permian and the Triassic. The climate at this time was arid to semi-arid (Goldsmith et al., 2003; Nystuen et al., 2014). The depositional systems described below are found to have similar characteristics to present day Death Valley, California, and a Death Valley model might be comparable.

4.1.1 Facies association 1

The base of the grain-supported conglomerates (1) has not been reached in core 16/1-13. The conglomerates are characterized by angular to sub-rounded basement clasts ranging in size from granule to cobble. The matrixes consist of medium to very coarse sand. The roundness of the clasts found in the matrix, appears without any grain size relations, since large clasts can be seen as both angular and sub-rounded. The degree of rounding is generally a function of grain size, composition of grain, type of transport mechanism and the distance of transportation (Boggs, 2011). The variation in the degree of rounding, consequently indicate that some of the grains have been subjected to longer transportation than others. The deposits of the conglomeratic facies are poorly sorted and poor in sedimentary structures, however, possible reverse graded bedding in the basal parts are occasionally observed. The conglomerates are chaotic, and consist of poorly sorted debris, mixed together, and are separated from each other by a finer grained matrix of sand. These characteristics all resemble debris flow deposits, as described by Bull (1972), Nilsen (1982), Nemec and Steel (1984), Blair and McPherson (2009) and Miall (2010).

There are distinct differences in the three matrixes; the grey matrix contains the largest clasts, while the percentage of clasts increases in the red matrix, but the clast size is smaller. The green matrix is intermediate between the two other matrix types, sharing similarities with both. It has clast sizes in the same range as the red matrix, but there is a higher abundance of larger clasts, and the percentage of clasts is more similar to the grey matrix. Changes in the supply and the transport distance from the provenance area, may have caused the differences in the percentage of clasts and of clast sizes, during the deposition of the different matrixes. The red and green matrix may contain different types of Fe-oxides, giving the different

colours, as described in Tomlinson (1916), Lobb (1949) and Potter et al. (1980). In the upper parts of the FA 1 interval, the conglomerates, represented by the green matrix, seem more matrix supported than grain supported, reflecting a reduced supply of basement clasts. The contact zones between the matrixes are often sharp and follow grain contacts, indicating that the difference between the matrixes is depositional, rather than diagenetic (Figure 4.1, left sketch). However, diffuse contact zones are observed in certain parts of the core, which appear to be of a more diagenetic origin. This observation applies especially for the red matrix, since it is found to cross-cut the other matrixes, and at these locations the red matrix does not follow the layering and grain contacts (Figure 4.1, right sketch). Thus, the red matrix can be found both as a depositional feature and a diagenetic feature in core 16/1-13. Loading and flame structures (Figure 3.4 B), are often disrupting the transition zones between the lower red matrix and upper grey or green matrix, indicating that the red matrix is less dense than the grey and the green matrix.

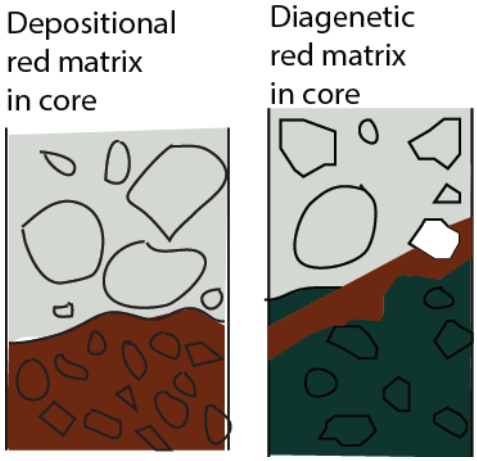

Figure 4.1: To the left: the depositional red matrix is found to have clear boundaries, and follows layering and grain contacts. To the right: the diagenetic red matrix is found to cross-cut the other matrixes, and do not follow the sedimentological layering.

The sandstone facies (2) found in FA 1, can be divided into three separate types of sandstone, based on the sedimentological structures found; laminated (2a), cross-bedded (2b) and structureless (homogeneous) (2c). The laminated and the structureless sandstones are the two dominating units, the structureless being more prominent in the lowermost parts, while the laminated dominate in the uppermost parts of FA 1 (Figure 3.1). Units with homogenous, structureless sandstone, may point to rapid deposition of a sediment rich suspension in the area at the time of deposition (Collinson et al., 2006). The laminated sandstones indicate fluctuations in the depositional conditions, since parallel lamination of different grain sizes reflect changes in flow velocity. Grains settling from suspension or traction transport of sand in water may have created the laminations (Collinson et al., 2006). Cross lamina/beds are created when ripples/dunes migrate (Collinson et al., 2006). The cross-beds found in the sandstones have a direction from right to left in the core, and are low angled. Ripples that appear to be upwards fining, are observed in the sandstones. These ripples imply that fluvial processes deposited the sandstones found in FA 1, since fluvial deposits generally display a fining upwards grain size, due to the helical nature of the stream (Collinson et al., 2006), but

the presence of upwards coarsening individual beds in the laminated sandstones points to an influence from the aeolian regime as well. Climbing ripples found in the sandstone facies, indicate a stream with a high content of sediments in suspension (Collinson et al., 2006). Strings of clay and varves observed, suggest fluctuations in the energy level in a fluvial stream. It is thought that the sandstone sequences located in between the different debris flow units may represent deposits deriving from streamflow processes, since these sediments constitute more sheet like deposits of gravel, sand, and silt that may be moderately to well sorted, cross-bedded, laminated, or massive (structureless) (Bull, 1972). The streamflow processes are those acting in any fluvial system and are the results of sediments deposited from suspension, saltation, and traction by flowing water. The flow may be channelized or non-channelized (Nilsen, 1982).

The siltstone facies (3) found in FA 1, is characterized by a greenish grey colour and is laminated. The high content of silt points to a low-energy environment. The lamination is created by the conditions described in the section above. The siltstone is gradually changing upwards to claystone facies (4) (Figure 3.4 D). The claystone is dark, greenish grey and contains no structures. The claystone indicates a low-energy environment, and the lack of laminated bedding, suggests that these sediments were continuously deposited from suspension, under non-changing conditions. There has been little or no fluctuation in depositional conditions and the sediment compositions (Collinson et al., 2006). These low-energy sediments may possibly be linked to overbank conditions, where the streamflow has overstepped its channel walls, due to increased water levels in the channel, probably linked to a period with increased humidity and rainfall. In overbank situations, the energy level is drastically reduced as the stream goes over its channel banks, and the sediments with the highest density will deposit first. In this case the siltstone constitutes the more dense sediments, and the claystone is most likely deposited from suspension, when the energy has been reduced to a minimum.

FA 1 is interpreted to be a possible alluvial fan characteristic, which may have developed along the fault margins in a half-graben setting. Alluvial fans are cone-shaped accumulations of sediments developing at the base of a mountain front or downslope from an active tectonic scarp. The sediments are supplied from mountainous catchments, by weathering and erosion of uplifted bedrock, to adjoining valleys, and the fan develop downslope from the area where the distributary channel emerges, known as the apex. The apex represents the most proximal

and highest part of the fan (Blair and McPherson, 2009). Sediments on alluvial fans are typically poorly sorted and contain a high abundance of gravel-size detritus (Blair and McPherson, 2009), which is represented by the debris flow sediments. The sandstone units, found between every conglomerate unit, represent fluvial streamflow activity, with influence from the aeolian regime, which is not uncommon on alluvial fans in dry climates (Blair and McPherson, 2009). Debris flows and streamflows are processes mainly triggered by intense precipitation and earthquakes, and thus are mostly infrequent and of short duration. But they have a high impact with respect to fan aggradation (Blair and McPherson, 2009). The fluctuation between the two facies indicates that there were regular changes in the supply from the hinterlands. According to Nemec and Steel (1984), deposits of debris flows in alluvial fan successions are often capped by upwards fining sandstones, resulting from turbulent fluid flow or heavily sediment-laden streamflows following the debris flow. The upwards coarsening trends found in the basal parts of the conglomeratic units, resemble what Collinson et al. (2006) describes to be caused by active fan progradation or outbuilding. These units were then deposited during periods of high activity on the alluvial fan and increase in energy regime, when the sediment supply was at its highest. It is not unrealistic to believe that the upwards fining sequences found at the top of every conglomeratic unit in FA 1, derive from periods when the fan were less active and experienced a decrease in energy regime. The sediment supply might also have decreased. The changes in sediment supply might reflect changes in relief, changes in tectonic movement, climate changes or changes in the provenance area (Collinson et al., 2006). The streamflow successions were deposited in periods with lower sediment supply from the provenance areas. At least five factors influence fan processes; catchment bedrock lithology, catchment shape, neighbouring environments, climate and tectonism (Blair and McPherson, 2009). The alternating layers of debris flows and streamflows may indicate that there were changes in these five factors, resulting in different processes transporting sediments to the fan area. The type of bedrock in the catchment area is the main control on the primary processes on the fan. Granitic to dioritic plutons and gneissic bedrocks split into particles ranging from sand to very coarse boulders due to the jointing, fracturing, exfoliation, and granular disintegration (Blair and McPherson, 2009). The granitic basement clasts found in the alluvial fan succession, may point to a granitic parent rock in the hinterlands.

Clay strings and varves are normally associated with changes in energy level, meaning that the streamflows had fluctuations in energy level. The silt- and claystones may be associated

with overbank deposits, and indicate that the streamflow went over its channel banks, and an abrupt decrease in energy occurred. Generally the proportion of debris flow deposits will decrease downslope, where channel-bound and overbank sedimentation starts to dominate (Bull, 1972; Nickel, 1985), and the gradual increase of both the thickness and frequency of the streamflow sandstones, may imply that the deposits moved towards the mid fan area (Figure 4.2), suggesting that the alluvial fan retreated. This phenomenon is described in Bull (1972) and Nilsen (1982), where streamflow deposits are found to be more characteristic of mid fan area, while the debris flow is more characteristic of upper fan area (Figure 4.2).

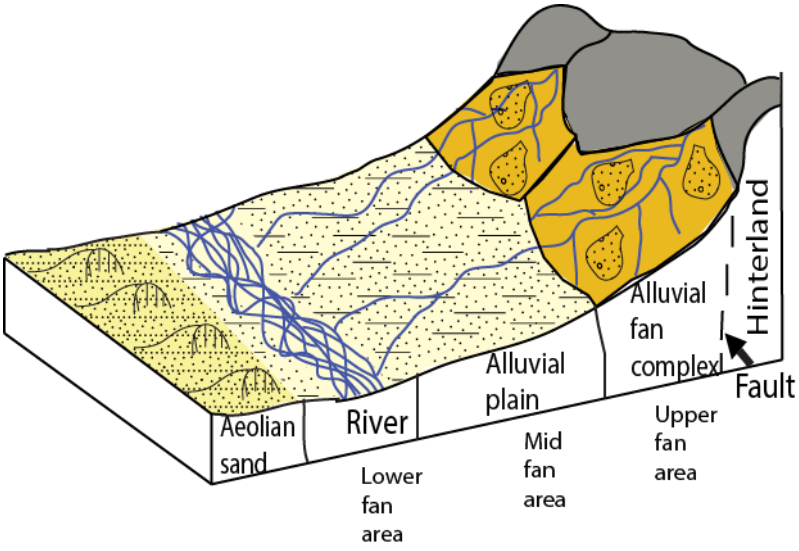

Figure 4.2: A schematic illustration of an alluvial fan depositional model. The aeolian and braided river systems found in facies association 2 are also represented in the lower fan area.

Nilsen (1982) also states that both facies can be found in any part of the fan, and that they typically intermix, as is observed in the core. The observation of a lower abundance of clasts and a decrease in the clast size in the conglomeratic matrix at the top of FA 1, supports the theory of a retreating alluvial fan. The retreating fan system may be linked to termination of rifting and the corresponding decline in sediment supply from the hinterland, as described by Blair and McPherson (2009). This setting is responsible for the change of dominating facies observed at the top of FA 1 from 1979-1967 m (Figure 3.1), where the alluvial fan goes from being a debris flow dominated fan to be a streamflow dominated fan (Figure 4.3).

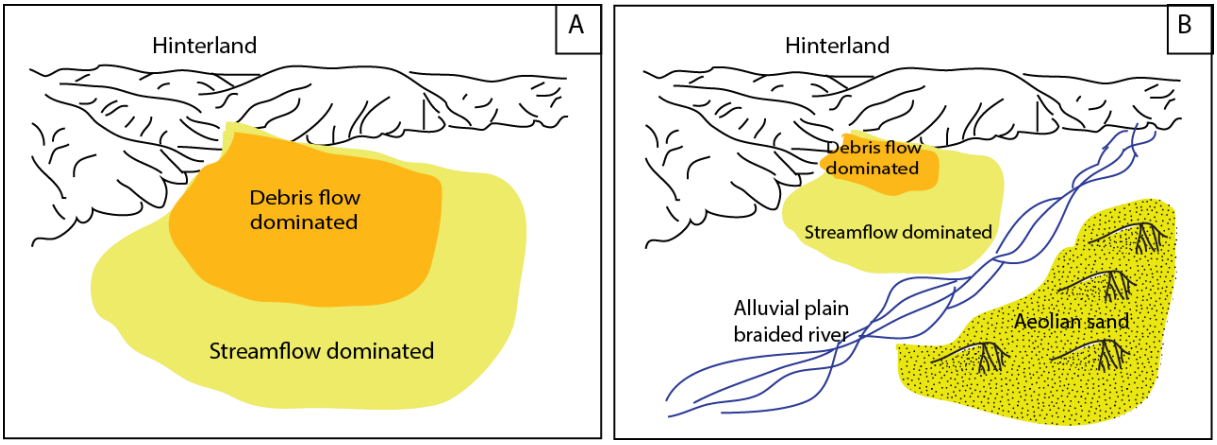

Figure 4.3: A schematic illustration showing the retreat of the alluvial fan. Figure A shows the fan at its maximum, while Figure B shows how the fan retreated and changed from being debris flow dominated to being streamflow dominated. The alluvial plain braided river and the aeolian sand represent depositional systems found in FA 2. Modified from Selvikvåg, 2012.

The sediments found on the alluvial fan may derive from reworked paleo-weathering profiles located on the Utsira High; sediments derived from the saprock part (Velde and Meunier, 2008) of weathering profiles.

4.1.2 Facies association 2

FA 2 represents general aeolian depositional environments. The dominating fine sand grain size, and the occurrence of several meter thick cross-bedded sandstones, indicate that these sediments were deposited in an aeolian environment and not a marine environment. No fossils have been found. The individual beds in the cross-bedded sandstone, were clearly upwards coarsening, which characterises aeolian sediments, where the finer particles may be removed by the wind, leaving the coarse grained particles behind (Mountney, 2006). The depositional systems found in FA 2, and how they are linked to the alluvial fan system can be observed in Figures 4.2 and 4.3.

Cross-bedded sandstones, several meters thick, were observed in the area from 1967-1944.70 m. However, in this depth interval, parallel laminated sandstones containing large grains, up to one mm, are also found. Grains in this size range are normally too large to be of aeolian origin. Generally, aeolian sediments contain sediments in the range of very fine to medium sand (Table 2.1) (Pye, 1987; Nickling, 1994; Mountney, 2006; Nichols, 2009), which makes the coarse, parallel laminated sandstones too heavy to have been transported by wind. The individual beds found in the parallel laminated sandstones, are too small to reveal if the laminations are upwards coarsening or upwards fining. But due to the occurrence of grains in the size range of one mm, the sediments constituting the coarse, parallel laminated sandstones in this depth interval (1967-1944.70 m) are interpreted to be of fluvial origin. The distal fan

and the fluvial area beyond the fan edge (the alluvial plains) (Figure 4.2) are areas of accentuated sorting and reworking of the materials deriving from the fan area. At this site, the meandering or braided rivers often constitute the dominating facies (Rachocki, 1981; Freytet and Plalziat, 1982; Nickel, 1985). It is believed that the coarse, parallel laminated sandstone layers found in FA 2, may constitute braided river deposits, possibly linked to the alluvial plain area (Figures 4.2 and 4.3). These braided river sediments are interacting with aeolian sandstones, which are observed with several meters thick cross bedding, and the aeolian sandstones are found to contain individual upwards coarsening bed sequences. There might have been an aeolian dune field, located further down slope from the alluvial fan, and while the alluvial fan retreated, the dune field migrated and started to interact with the braided river at the alluvial plain (Figures 4.2 and 4.3). The coarse, parallel laminated sandstone and the cross-bedded sandstone interact with each other up to a depth of 1944.70, where the aeolian system starts to be dominant, and the cross-bedded sandstone of facies 6, constitute the dominating facies. After 1944.70 m the parallel laminated sandstone of facies 5 can still be observed, but now the dominating grain size is fine to medium sand (0.125-0.5 mm). The medium-fine grained, parallel laminated sandstones have by thin section analyses been found to have individual lamina showing upwards coarsening sequences, which implies an aeolian origin for these sandstones. The braided river deposits did not become a dominating depositional environment, and for that reason, the depth interval between 1967-1944.70 m are considered as an area of gradual change, and not a separate facies association. The minor laminations found in the individual coarse, parallel laminated sandstone units, are of different grain sizes, indicating a system with multiple flow regimes and changing energy levels of the currents.

The clearly dominating direction of the cross-beds from right to left in the core, reflects a stable wind direction in the area. A few units found with cross-beds in a reversed direction, indicate that the wind may have changed direction for a little period, only to flip back to normal again. The growing cross-beds (Figure 3.8) found several places in the core, are remnants from prograding dunes in the aeolian facies. The calcite cemented sandstone intervals indicate that there has been water flushing through the porous sediments, leading to the precipitation of calcite.

4.1.3 Facies association 3

The transition between facies association 2 and 3 are abrupt. At the top of the cross-bedded aeolian sandstone facies, the core suddenly contains rounded, granitic basement clasts, before

a few centimetres with aeolian sandstone occur. The core is missing 24 centimetres, between 1919.70 to 1919.46 meters, and at level 1919.46 meters, a sudden occurrence of calcareous sandstones, rich in marine, nektonic and benthic fossils can be observed. Severe erosion took place in the area, as seen in the sudden shift of depositional environments, and the lack of shallow coastal regimes. The calcareous marl found in FA 3, is interpreted to be the Åsgard Formation, deposited in the Early Cretaceous (Figure 1.4), while the aeolian sandstone is of Triassic age (NPD, 2015 a), meaning that the Jurassic strata is missing from the area. The Jurassic section may have been eroded when the North Sea region was affected by the Mid-Jurassic doming (Ziegler, 1992; Jackson et al., 2010), which led to an uplift of the North Sea area, causing sub-aerial exposure of the Jurassic sediments. The sediments of FA 3, are clearly marine due to the presence of nektonic, marine fossils, and the presence of carbonates, indicate that the environment must have been well oxygenated and the clastic input to the basin must have been low. The ten cm thick conglomerate between the calcareous sandstone and the green marl, marks a transgression event, and a minor rise in sea level. The rather abrupt change from green marl to calcareous siltstone, might point to a sudden increase in energy. The calcareous siltstone is around 15 cm thick, and the shift to red marl, points to a reduction of the energy level in the area.

4.2 Mineralogical composition and diagenetic history of core 16/1-13

4.2.1 Clay mineral theory

The common clay minerals found in sedimentary rocks include kaolinite, smectite, illite, chlorite, and mixed layer clays as interstratified illite-smectite and chlorite-smectite (Bjørlykke et al., 1989). The composition of clay minerals may reflect different sediment sources, and the origin of clay minerals in sedimentary rocks are a product of e.g. weathering in the provenance area, climate, rate of erosion, physical sorting and chemical modification during transportation and deposition. The clay minerals can also undergo post-depositional changes, which will alter the chemistry during diagenesis (Potter et al., 1980; Galán, 2006; Agha et al., 2013). Authigenic clays are known to form either as a direct precipitate from formation waters (neoformation), or through reactions between precursor material and meteoric water (regeneration) (Wilson and Pittman, 1977). The type and intensity of weathering, is the result of climate, precipitation, lithology and morphological setting. When considering the origin of clay minerals, chemical weathering is considered to be the most important weathering mechanism (Potter et al., 2005). Moisture and temperature are important factors, which will influence chemical weathering (Weaver, 1989). Clay mineral

distribution is often linked to temperature, precipitation and climatic zones (Thiry, 2000). Clay minerals are very useful for paleoclimatic reconstructions, interpretation of the tectonic history of a region, determination of source area, definition of the timing, and nature of diagenetic reactions, due to their sensitivity to changes (Galán and Ferrell, 2013; Agha et al., 2013). Areas of intense precipitation and high temperatures are often associated with intense and rapid weathering, while in arid environments, e.g. deserts, the weathering proceeds more slowly, since there is little rainfall, which is necessary for chemical reactions to occur. According to Nesbitt and Young (1989), weathering reactions mainly involve the transformation of feldspars and phyllosilicates to the secondary mineral groups, kaolin, illites, smectites, vermiculites and/or chlorites. They state that weathering is only restricted to the interactions between waters derived directly from precipitation, and the rocks and their weathering residues. Interactions between groundwater, rocks, and the materials of the weathering profiles are referred to as diagenesis.

Microscopic, SEM, and XRD analyses have all indicated the presence of clay minerals in the samples taken from core 16/1-13, where smectite, illite-smectite, and kaolinite have been the three most dominating and abundant clay minerals. Additionally, chlorite and illite have been observed during SEM analyses. Kaolinite is typically formed as a weathering product in areas with abundant rainfall, good drainage and acid meteoric water (Potter et al., 1980; Galán and Ferrell, 2013). Smectite are frequently formed where there is lower temperature, less water percolation and the removal of potassium or sodium is slower, the groundwater has a high pH and a high silica activity (Weaver, 1989; Galán and Ferrell, 2013). These settings are commonly associated with desert areas, where there is little rainfall. Hence, the weathering will proceed more slowly. Limited flushing and leaching of pre-existing crystalline rocks, like granites, in weakly drained landscapes will favour a smectite rich soil (Agha et al., 2013). Smectite is also favourable in areas with low relief, leading to poor drainage (Weaver, 1989). Randomly mixed-layer illite-smectite clays originate in temperate seasonal climates with pronounced dry seasons, and require K-bearing precursor minerals (Galán, 2006).

4.2.2 Observations and discussion about clay mineral origin

The clastic minerals representing the alluvial fan in core 16/1-13, possibly derive from reworked paleo-weathering profiles located on the Utsira High, which were eroded and transported to the half graben basin. Questions are raised about the origin of the clay minerals found in core 16/1-13. Do they represent clay minerals originated due to the interaction of granites and rain water in the source area, are they derived during transport and deposition, or

are they diagenetic features linked to the interaction of clastic sediments or detrital clays, and meteoric groundwater flow? Another question is; have the basement clasts found in the conglomerates been weathered and then transported, and not been subjected to diagenesis, have they experienced both weathering in the source area and diagenesis, or have they only been exposed to diagenesis?

The clay minerals only constitute a small portion of the bulk composition in the sediments found in the alluvial fan system of core 16/1-13, as suggested by XRD analyses and point counting (Appendices C and D). This may imply that the diagenetic processes have been low, but present. The varying degree of alteration and the presence of both altered and unaltered feldspars are an indication of a low degree of subsurface alteration, the thin section analyses suggest that categories II, III, and IV dominated in plagioclase preservation. Category I is often found to have low percentages, implying that the influence from subsurface alteration is present. For K-feldspar, which is more resistant to weathering (Goldich, 1938), categories I and II dominate. Most of the weathering has probably been located in the source areas, but the appearance (well developed crystal structure) and behaviour (unbroken coatings and clay mineral relations (Figure 4.13)) of the clay minerals, indicate a diagenetic origin, with the identification of the crystalline habits of the clay minerals, as described by Wilson and Pittman (1977). The presence of both unaltered and altered feldspars may point to at least two different source areas, or the feldspars may have derived from different levels in the weathering profile. Clay minerals may not only be derived from the dissolution of feldspars, dissolution of micas also create authigenic clay minerals e.g.:
Feldspar: $2K(Na)AlSi_3O_8 + 2H^+ + 9H_2O \rightarrow Al_2Si_2O_5(OH)_4 + 4H_4 + SiO_4 + 2K^+(Na^+)$ (Bjørlykke, 1998; Lanson et al., 2002).
Muscovite: $2K(Na)Al_2AlSi_3O_{10}(OH)_2 + 2H^+ + 3H_2O \rightarrow 3Al_2Si_2O_5(OH)_4 + 2K^+(Na^+)$ (Stoch and Sikora, 1976)
Biotite: $2K(Mg,Fe)_3AlSi_3O_{10}(OH)_2 + 12H^+ + 2e + O_2 \rightarrow Al_2Si_2O_5(OH)_4 + 4SiO_2 + Fe_2O_3 + 4Mg^{2+} + 6H_2O + 2K^+$ (Stoch and Sikora, 1976).

SEM and optical analyses have revealed the presence of both dissolved feldspars and micas. It is challenging to decide if the weathered feldspars have only been affected in the source area, or if the feldspars have been affected by both weathering before transport and by diagenetic alteration during burial. The author believes that the feldspar grains have experienced both

weathering prior to transport, and alteration during burial. The reason for this statement being that the feldspars show a varying degree of alteration, with the presence of both altered and unaltered grains, pointing to varying weathering in the source area. Further, the percentages of unaltered plagioclase grains are low (Table 4, Appendix C), indicating that post-depositional alteration has occurred, since plagioclase is among the first minerals to dissolve (Goldich, 1938). Further, the micas are among the first minerals to break and dissolve during transport due to their fragile nature, and if these micas were dissolved before transport, the grains would not look as they do, e.g. the altered cleavage planes, would not have survived a transport, indicating that some dissolution are linked to subsurface alteration (Figure 3.20). The behaviour of the micas, also suggest post-depositional influence from adjacent detrital grains, where the micas have been compressed, due to the compaction and deformation of detrital grains (Figure 4.4).

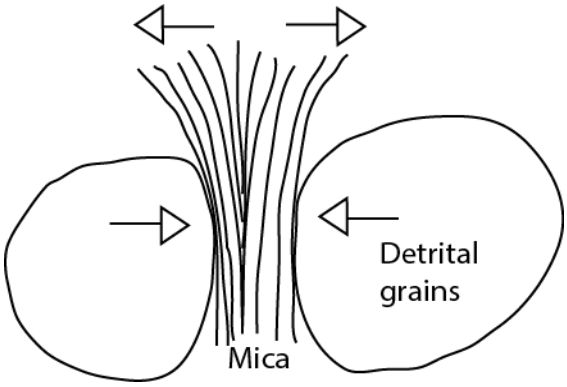

Figure 4.4: An illustration of how the detrital grains are compressing and deforming the micas during burial. The arrows inside the detrital grains illustrate the compressional pressure, while the arrows above the mica illustrate the direction of released pressure. This releasing pressure leads to opening of the mica cleavages, and meteoric water is free to flow into the cleavages and alter the micas, leading to the precipitation of clay minerals.

The presence of authigenic clay minerals, e.g. kaolinite, smectite, chlorite, and illite-smectite, both as pore fill and as coatings, are a sign of a diagenetic origin, either by neoformation or regeneration processes, for the clay minerals. Generally the clay coatings (smectite, illite-smectite and chlorite) are found to coat entire grains, and do not show any signs of breakage. This indicates that these clay minerals most likely are formed by direct precipitation of clay minerals, or by recrystallization of detrital clay minerals, rather than being formed by weathering. The clay coatings are found to be present both along grain contacts and not along grain contacts (Figure 4.5), which mean that there is presence of both directly precipitated clay minerals (neoformation) and recrystallized detrital clay (regeneration). The clay coatings would not appear that perfect if they had been exposed to transportation.

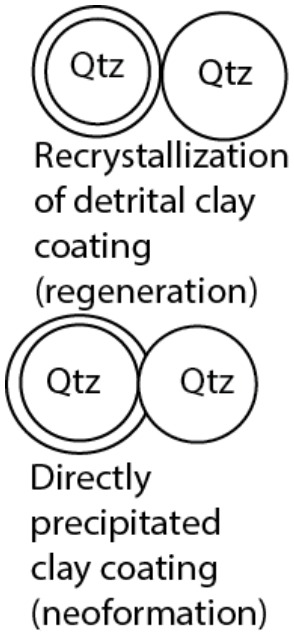

Figure 4.5: A schematic illustration showing the behaviour of the recrystallized detrital clay and the directly precipitated clay.

They would surely have shown signs of dissolution and breakage, due to the fact that clastic grains tend to collide and be subjected to traction during transportation. As described by Wilson and Pittman (1977), the delicacy of the clay flakes exclude extended transportation. They state further that this criterion is particularly applicable for chlorite and kaolinite. Similar arguments can be used for the pore filling clay minerals, often found to be kaolinite and smectite. The kaolinites are most often found to be perfect booklets, and such booklets would have been destroyed during transport. Smectite is formed during several climate conditions, but are commonly found as intermediate stages in the progressive weathering of e.g. biotite and plagioclase (Tardy et al., 1973), indicating that smectite is transformed during progressive weathering and alteration. Further, the sediments found in the conglomerates may be derived from the upper part of a reworked weathering profile, and it is not likely that smectite would have survived that long interaction with rainwater, and might have transformed to another clay mineral (Figure 4.6). The smectite has been observed to form long thread structures (Figure 3.19 E), appearing to be some microns long, and according to Wilson and Pittman (1977), such structures exclude transport of the clay as a detrital grain, meaning that the authigenic smectite might have been formed by direct precipitation or from recrystallized detrital smectite.

The chlorite crystals would have been affected by the transport, but the chlorite crystals appear to be unharmed and perfectly shaped. This argues once again, for a diagenetic origin by either neoformation or recrystallization of detrital chlorite, for the authigenic chlorite observed.

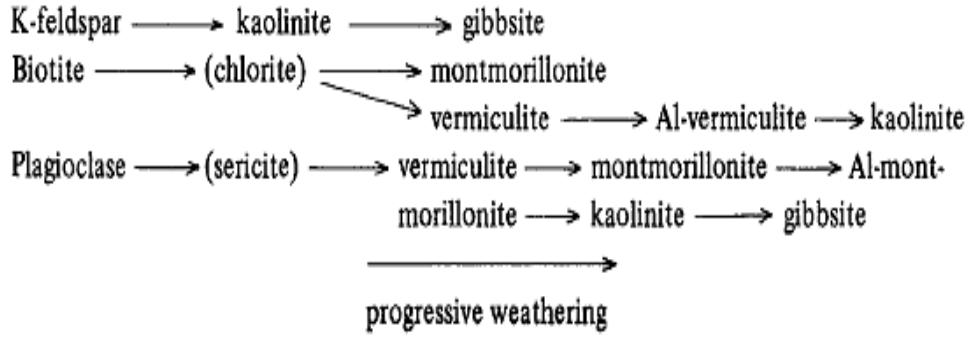

Figure 4.6: Progressive weathering of the primary minerals to the left, leads to sequences of clay mineral formation. The arrows imply that the mineral to the right replaces the mineral to the left (Tardy et al., 1973).

The presence of non-booklet shaped kaolinites and the denser smectite (Figure 3.18 A-B) are more difficult to assign an origin. In the majority of these kaolinites, remnants of earlier, randomly distributed booklet structures can be observed, suggesting that they have once been

authigenic. The interpretation of these kaolinites is that there has been some focused groundwater flow, flushing through specific parts of the sediments, which led to the disturbance and the destruction of the booklet structures (pers. com. H. Dypvik, 2015). If there had been a flushing of water through all the parts of the sediments, no booklet structures would have been found and the kaolinites would appear as a solid mass, creating a possible pattern "flow". The kaolinites would have been oriented, and these arguments support the theory of a focused flow through specific parts of the sediments. The more massive kaolinite appearing like a solid, dense mass (Figure 3.18 A), might have been transported by water. It seems to have an orientation through the pores, and fragments of K-feldspar can be observed inside the kaolinite, indicating that the kaolinite may derive from the dissolution of clastic K-feldspar. Regarding the different smectites, the origin is difficult to decide. The dense smectite is also found in association with fragments of clastic K-feldspar (Figure 3.18 B). These smectites might have been formed by some focused groundwater flow, flushing through specific parts of the sediments, which led to the disturbance and the destruction of the honeycomb-like, authigenic smectitic structures, or the smectites might also derive from recrystallized detrital smectite. The mineralogical differences between the authigenic smectite and the denser smectite are a reduction of the Al and K content in the authigenic, but the reduction is low. This reduction may point to different origin for the authigenic and the denser smectite. The differences in the feldspar content from the XRD and point counting, where XRD has revealed a higher content of feldspar than point counting, can be caused by fragmented feldspar found within the pore filling clays, which have been too small to be observed during point counting, but have been registered during XRD.

Ti-rich minerals, like anatase and brookite, are minerals often found in associations with weathering profiles (Jackson and Sherman, 1953; pers. com. P. Schroeder, 2015). These minerals have not been observed during any analyse, implying again that the majority of clay minerals in 16/1-13 originated by diagenetic processes, and not from the weathering profile or as non-crystallized detrital clay originated from transport and deposition.

The 16/1-13 core section has most likely not been buried deeper than its present depth of burial, which are around 2 km (pers. com. L. Riber, 2015). This depth suggests that these sediments have only experienced early or shallow diagenesis. Reports from the Norwegian Petroleum Directorate (NPD, 2015 a) state that the bottom hole temperature for well 16/1-13 was found to be 92°C. At shallow depths and low temperatures, hydrous clay minerals e.g.

kaolinite and smectite, may form as a result of weathering or early diagenetic processes during meteoric water flow as described by Bjørlykke (1998). The clay minerals formed in this process, are only stable at low temperature, and with increased burial depth and temperature, they become unstable, and a new reaction forms: clay (kaolinite, smectite) + cations (K^+) = aluminosilicate (illite) + quartz + water. It is important to keep in mind that the reaction described above, only occurs if kaolin, smectite or other potentially unstable clay minerals originally precipitated at shallow depth. The reaction can only be driven if reaction products are removed by e.g. flushing of meteoric water, and due to the requirement of new supply of protons, the process can only be present in an open system (Bjørlykke, 1998). The authigenic clay minerals may also have formed by recrystallization of detrital clay.

Kaolinite

The booklet shaped kaolinites present in the sediments, show the stacking of pseudohexagonal plates, pointing to an authigenic origin. Observations by SEM and optical microscopy, show that the kaolinite is pore filling and that they often fill the voids found in the dissolved feldspars. The booklet structure differed in size, and there were evidence of light cracking and bending (Figure 4.7 A). This implies that the kaolinite has been affected by a low degree of compaction, probably linked to the mechanical regime. The different sizes of the hexagonal plates indicate that there were more space to grow in certain sediments, and that the time of growing may have been longer for the larger plates (Figure 4.7 B). The sandstones from the aeolian environment are found to have the largest kaolinite structures. These sediments have the highest porosities, giving the individual kaolinite minerals more space to grow, while the kaolinite structures found in the conglomerates are smaller, indicating reduced space to grow, due to smaller pore sizes. The permeabilities most likely were higher in the sandstones, giving a higher flux of water flushing through the pores. The favourable conditions for the precipitation of kaolinite as described by Potter et al. (1980) and Galán and Ferrell (2013), may indicate that there have been periods with an increase in the humidity, maybe linked to a rain season. This could have increased the groundwater flow, and leaching would have been more intense.

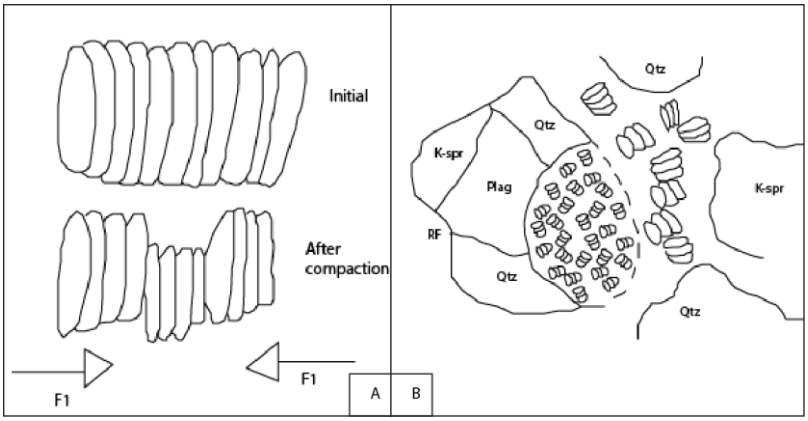

Figure 4.7: A shows how the compaction forces have deformed the kaolinite booklets. B shows how the kaolinite structures differed in size, due to the available space to grow.

Illite and smectite

Authigenic, flaky, illite is often found to be associated with the dissolution of unstable aluminous mineral phases. The unstable aluminous phase may be kaolinite or smectite. The kaolinite→illite reaction occurs, according to Bjørlykke (1998) at depths close to 4 km and at temperatures above 120°C. The other precursor mineral for authigenic illite, is smectite. This reaction is continuous, and illite is formed from smectite via intermediate mixed-layer illite-smectite (Lanson et al., 2002). The reaction process is as follows: smectite + K^+ = illite + silica (via mixed-layer minerals) (Bjørlykke, 1998). The smectite to illite reaction occur at temperatures around 70-100°C, which in the North Sea correspond to a burial depth of 2-3 km (Bjørlykke, 1998). The latter reaction may probably be the main cause for the authigenic illite found in the samples from core 16/1-13, due to the fact that the bottom hole temperature has been measured to 92°C. The sediments have not been buried deep enough for the kaolinite to become unstable, and start to dissolve, implying that the illite originated from the smectite. SEM analyses revealed presence of both smectite and illite-smectite, thus, the precursor minerals are present for the reaction to occur. The smectite found in the sediments, has by SEM analyses, been found to have a diagenetic origin, due to the presence of nicely, honeycomb-like authigenic structures, and is most likely formed at shallow depths as a result of early diagenetic processes caused by meteoric water flow (Bjørlykke, 1998), or by recrystallization of detrital smectite. The smectite has possibly been precipitated when the pore water has had a high silica concentration (Aagaard and Helgeson, 1982). An increase of the silica concentration will decrease the stability of kaolinite, and smectite will precipitate instead, due to the fact that smectite is more stable in systems saturated with respect to quartz (Galán and Ferrell, 2013). The smectite could have been formed in times when rainfall was at a low level (Potter et al., 1980; Weaver, 1989).

Chlorite

Chlorite was identified on SEM and by XRD analyses. The SEM showed the presence of authigenic chlorite, where the crystal (rosette-like) structure was clearly visible. The precipitation of chlorite, as described by Bjørlykke (1998), requires a source of Mg and Fe, where possible sources are linked to clastic biotite, basic rock fragments, and volcanic rock fragments. Clastic chlorite can also act as a precursor. The presence of clastic biotite, clastic chlorite, and rock fragments containing biotite, were confirmed during optical microscopy and during SEM analyses. Biotite grains were found to be both unaltered and altered. The altered grains showed signs of dissolving along the cleavages, and the microscope showed clay minerals e.g. kaolinite and chlorite, forming inside the renewed pore space between the cleavages (Figure 3.20). SEM analyses confirmed the presence of both chlorite and kaolinite, between the biotite cleavages. As shown in Figure 4.6, kaolinite and chlorite are both secondary products of biotite, but they appear at different stages of the biotite alteration. Hence, the biotite grains of core 16/1-13 are found to be at different stages in their alteration process. The authigenic chlorite might also derive from the recrystallization of detrital chlorite.

4.2.3 The basement clasts

The clasts found in the conglomerates of FA 1 are granites, granodiorites and quartz monzonite in origin (Figure 3.9), and are eroded material derived from basement. These different clasts, indicate at least two different provenance areas. Similar plots in the Q-P-A diagram, have been found by Riber et al. (in prep.). Optical and SEM analyses of basement clasts reveal varying degrees of feldspar alteration. Most of the clasts classify as a type two (slightly altered) or type three (moderately altered) (Table 2, Appendix B). The degree of weathering is relatively low in the basement clasts, indicating that they derive from rather deep in a reworked weathering profile, possibly linked to the altered coherent rock stage as described by Velde and Meunier (2008). The altered coherent rock still has the same structures as the fresh rock, but the onset of weathering has led to an accumulation of clay minerals in the newly formed secondary porosity areas (Velde and Meunier, 2008). Thus, the uppermost part of the weathered basement profile must have been removed, before the clasts were eroded, and transported out to the depositional site. The upper part of the weathering profile may have been transported to the alluvial fan area, and may constitute a large part of the conglomeratic matrix.

There is one sample (1991.55) that stands out from the others, representing a higher degree of weathering. It can be classified as a weathering type 4 (highly altered), meaning that more than half of the rock material is decomposed. The varying degree of weathering may point to the basement clasts as being derived from different provenance areas or at least from different parts of the weathering profiles, which is also confirmed by the mineralogical difference. The different degrees of weathering are a direct indication of pre-erosional weathering, meaning that the clasts have been altered, and clay minerals were probably produced at that time. Further, the difference in the degree of feldspar alteration in the individual samples, indicate that most of the weathering occurred in the source area, where chemical weathering has affected the parent rock, before transportation and deposition.

In most of the basement clasts, clay minerals constitute a rather low percentage, implying again a low degree of weathering, as is supported by SEM, XRD and optical microscopy. These clasts may derive from a low part of the original weathering profile. The clast found at depths of 1991.55 m, has not surprisingly, been found to have the highest clay content, due to the higher degree of weathering, possibly deriving from a higher position in the original weathering profile. The minor porosity found in the basement clasts, are all derived by the dissolution of feldspar, possibly linked to dissolution by acidic water or hydrothermal water, giving it a secondary origin. The hematite content is low in these samples, but during SEM and optical microscopy, Fe-oxides are observed in micro cracks. These Fe-oxides are possibly linked to the last of the three Fe-oxide phases observed in the sediments of core 16/1-13, and the third Fe-oxide phase is found to have a diagenetic origin, since the Fe-oxides is located in cracks associated with compaction during burial (a fully description of the third Fe-oxide phase can be found in section 4.2.4). The carbonate cement found in the basement clasts, is found in association with dissolved feldspars, where the carbonate cement is filling the pores found in the altered feldspars. This observation is direct evidence of carbonate cementation postdating the dissolution of feldspars (Figure 4.8). The pore filling carbonate has euhedral shape, and is also found to postdate the authigenic clay minerals, since fragments of clays can be found at the carbonate crystal edges. The muscovite/illite content found in these samples is associated with sericitization of feldspar grains.

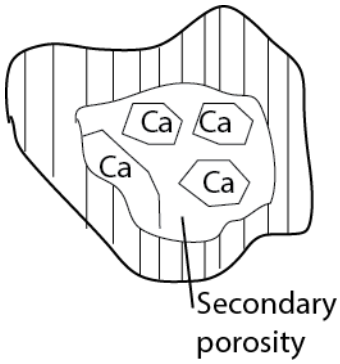

Figure 4.8: An illustration showing the relationship between the dissolved feldspar, here represented by a plagioclase, and the calcite cement (Ca). Notice how the calcite is growing inside the secondary porosity created by the dissolution of the feldspar grain.

SEM analyses displayed that the secondary porosity, originating from dissolved feldspar, was, in some of the samples, filled with kaolinite, forming excellent booklet structures. The kaolinite found, not appearing like booklet structures, was probably formed due to the dissolution of K-feldspar and water transport, as described above. Kaolinite was not observed in all of the samples, and the pore space in these samples did not contain any clay minerals at all. The clasts observed by SEM analyses, have been found to contain smectite, illite-smectite, and chlorite as well. Authigenic clays are the dominating form of clay minerals in these samples, but the question is; have these clays originated during weathering, and survived transportation to the basin, or did they form by diagenesis, by regeneration or neoformation? This is a challenging question, due to the fact that similar clay minerals are formed during chemical weathering at the surface, and during subsurface alteration linked to diagenesis, and they will in both cases reflect an authigenic crystal structure. The author argues for a diagenetic influence as well as a weathering influence on the clasts. During SEM one clast (clast 4 (1995.45)) was found to carry rhombic dolomite crystals (Figure 3.17) in the pores. Dolomite is often found to be a late diagenetic product requiring high temperatures to form (Machel and Mountjoy, 1986), and is normally not associated with weathering profiles. Dolomite has been observed in the conglomeratic matrixes as well, indicating that the clasts have been exposed to diagenetic processes during burial. Fragments of clay were observed along the dolomite crystal edges, predating the clay minerals before the dolomite precipitation. Thus, the basement clasts have experienced both weathering in the source area, and alteration linked to burial. The low porosity values found in the clasts would have inhibited a large influence from diagenesis, because low permeability values would have severely reduced the flow of meteoric water through the clasts. The content of clay minerals and carbonate cement are quite low in the clasts compared to the matrix and sandstone samples, and if the clay minerals were actually formed by diagenetic processes, one can argue for a lower diagenetic influence on the basement clasts, compared to the other sediments found in the core. This is probably linked to the lower porosity and permeability values.

4.2.4 Fe-oxides found in FA 1

Various Fe-oxides are responsible for the red colour present in the sediments, and these types of red beds may form in several environments e.g. arid, desert conditions or seasonal climates. The red colour forms, when iron is taken into solution through the decomposition of ferromagnesian minerals, and oxidises to Fe^{3+} (Morton and Hallsworth, 1999). Fe-oxides are often found as hematite (Fe_2O_3), which is confirmed by SEM analyses of the 16/1-13 samples.

The Fe-oxides appear as coatings, pore fill, pore linining/rim, and within micro cracks, and are believed to have formed during three separate phases. The pore filling and pore lining/rim Fe-oxides are commonly not found in clay rich parts of the conglomeratic matrixes, indicating that clay minerals, predates the Fe-oxides. Overgrowths of either K-feldspar or quartz have not been observed in the Fe-oxides rich areas, postdating the overgrowths after the Fe-oxide precipitation. The first phase is linked to oxidation during deposition, creating grain coatings. The sharp boundaries between the matrixes observed during logging, indicate a primary origin for the red matrix, making it a depositional feature (Figures 4.1 and 4.9), which were confirmed by optical analyses. Optical analyses showed that small grains are fully coated, while larger grains are only partly coated (Figures 3.11 A and 4.9). This may suggest that the sediments found in the red matrix, were derived from two different source areas. The smaller grains are well rounded, and the fully coated grains imply that these sediments have experienced long transport in well-oxygenated environments, prior to deposition. The larger grains, which are only partly coated, are less rounded, indicating a shorter transport in a low-oxygenated environment before deposition. During core logging, the red matrix was found to contain a higher abundance of clasts (Figure 3.4 B), compared to the other two matrixes, which has been confirmed by optical analyses and point counting. Optical analyses show that the rock fragments found in the red matrix have a high content of feldspar, while the presence of individual feldspar grains is generally low. For that reason, the quartz/total feldspar found from XRD is not really representative for the red matrix, since this ratio will consider the total feldspar content found, and not separate feldspar deriving from individual detrital grains or from rock fragments. The ratio from XRD does not consider the presence of two source areas, which the ratio from point counting does. The rock fragments disturb the results from XRD, giving a “misleading” result. A new, revised ratio was calculated after point counting, which was substantially higher. This new ratio confirms the reasoning of the smaller grains being exposed to longer transport, and fluvial processes may have been the transport mechanism, before deposition on the alluvial fan.

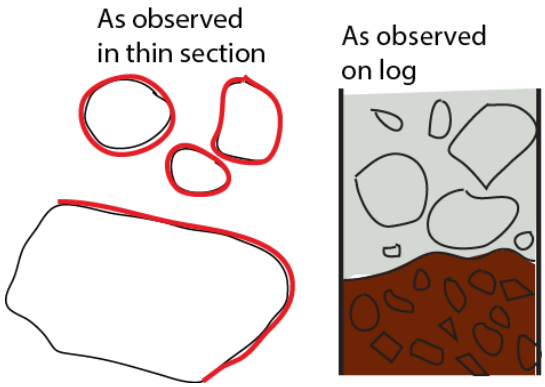

Figure 4.9: A schematic illustration of how the first Fe-oxide phase was observed in thin section and in the sedimentary core.

The second and third Fe-oxide phases are linked to oxidation during burial, making them diagenetic features. The absence of Fe-oxides at grain contacts in certain areas, while Fe-oxides were found around the same grains (Figure 3.11 B), points to a diagenetic origin for this phase (Figure 4.10). The diagenetic red matrix was also observed during logging (Figure 4.1). There were areas where no clear separation could be found between the different matrixes, and the red matrix cross cut both green and grey matrix, suggesting a diagenetic origin for the second Fe-oxide phase. During the second phase the Fe-oxides starts to act as both pore fill and as pore linings/rims.

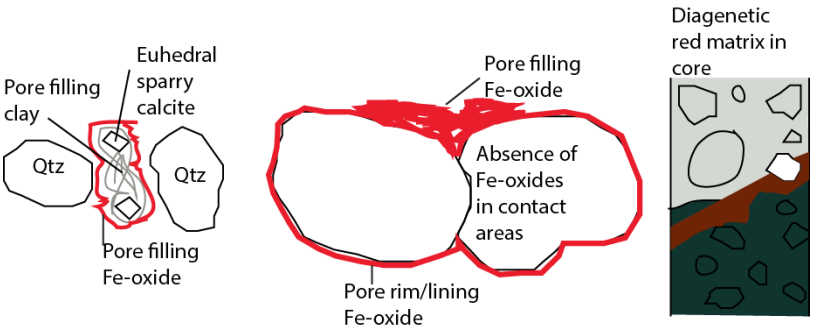

Figure 4.10: A schematic illustration of how the second Fe-oxide phase was observed in thin section and in the sedimentary core.

A third Fe-oxide phase is recognised within the basement clasts, where it occurs within micro cracks in individual phenocrystals and in crystal contact zones (Figure 3.10). Uplift of the area may have been the source of the diagenetic Fe-oxide phases, where sediments with low clay content had the required porosity values needed, for the oxidising reaction to occur. The second Fe-oxide phase was observed to coat a few clay minerals (Figure 4.11), and the second and third phase is not commonly observed in the clay rich area, implying that the diagenetic Fe-oxides postdate the authigenic clays, making them late diagenetic features.

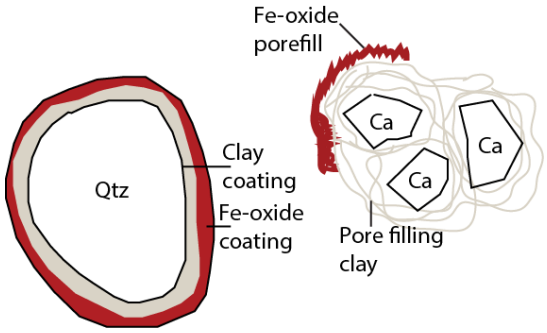

Figure 4.11: An illustration showing the relationship between Fe-oxides and clay minerals in the red matrix. The Fe-oxides are clearly formed after the authigenic clay minerals.

4.2.5 The conglomeratic matrixes

The analysed samples from the conglomeratic matrixes show dominant clastic composition of quartz, plagioclase and K-feldspar. The presence of clastic micas, both in the form of muscovite and biotite, are together with the high content of feldspar, an indirect evidence of the immature nature of the conglomeratic sediments found on the alluvial fan. Micas and plagioclase are according to Goldich (1938) (Figure 4.12) among the first minerals to dissolve

or break up, from weathering and during transportation, suggesting that these sediments have experienced rapid erosion and short transportation. This is to be expected in a fault-controlled basin, e.g. a half graben. The low quartz/total feldspar in the conglomeratic samples, confirm this reasoning. The content of the quartz and the feldspar minerals are quite stable throughout the conglomerates in 16/1-13, indicating little change in the length of transportation from the hinterlands. The red matrix is an exception to the reasoning described above, as the new quartz/total feldspar from point counting points to finer sediments being exposed to longer transport. Since most of the feldspar content in the red matrix derives from rock fragments, the quartz/total feldspar calculated from XRD is "misleading"; the rock fragments disturbs the quartz/total feldspar obtained from XRD. That said, the degree of sorting is very poor due to the high amount of rock fragments, implying that the red matrix also can be considered as immature sediments.

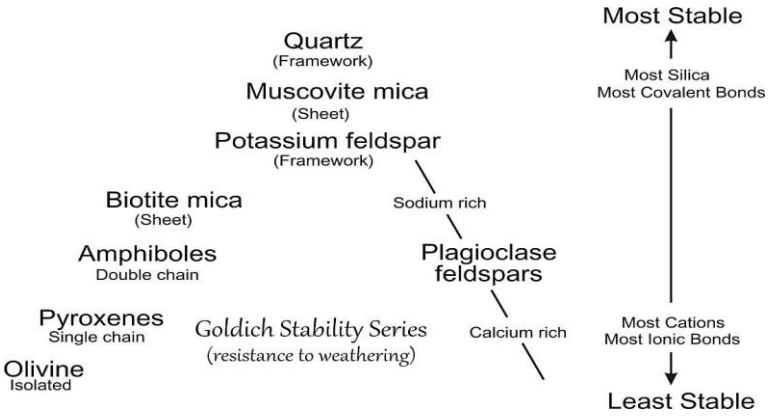

Figure 4.12: The Goldich stability series, showing different mineral groups and their resistance to weathering. (Goldich, 1938).

The results obtained from XRD, SEM, and optical microscopy reveal more similarities than differences when considering the mineralogy of the three matrixes from core 16/1-13. The mineralogy is not completely similar, but the differences between the matrixes are so small, indicating that the parent rock composition, the depositional conditions, and burial history may have been quite similar for the three matrixes.

The largest difference between the three matrixes seems to be the issue of the colours, and the size and abundance of basement clasts, which suggests differences regarding the depositional environment and supply from the provenance area. Further studies may be needed for absolutely determine if there are some differences when considering the mineralogy of the matrixes. More samples should be tested, and more data from adjacent cores can be used. The red matrix has clearly been deposited during a time of oxidising conditions, leading to the

development of ferric (Fe^{3+}) oxides. The green matrix may contain ferrous (Fe^{2+}) oxides and chlorite clay, which may be responsible for the green colour. The green matrix has probably been deposited during periods of lower oxidising conditions. The grey matrix may be poor in iron, and the grey colour may point to less or no oxidation. The observation of red matrix not occurring above 1980.20 m depth, means that the conditions changed, and that the favourable oxidising conditions stopped. The observation of an increased amount of green matrix towards the top of FA 1, implies more favourable conditions linked to these deposits, and reveals a ferrous and possibly a more intermediate oxidation at the site of deposition.

Authigenic clay mineral relations in the conglomeratic matrixes

The same clay minerals and clay mineral relations are observed in the three different conglomeratic matrixes. Chlorite is found to act as one of the coating minerals in the matrixes, as revealed by SEM, showing rosette-like structures. Where multiple layers of coating occur, chlorite is found to be the first of two layers, whereas smectite and illite-smectite is found to form the second layer, indicating that chlorite precipitation predates the smectite and illite-smectite (Figure 4.13 A). An illite crystal was found to drape around a kaolinite booklet, postdating the illite after the kaolinite (Figures 3.19 C-D and 4.13 B). The kaolinite was found to be pore filling and SEM analyses revealed smectite crystals being effected by the precipitation of kaolinite booklets, where the kaolinite booklets appear to bend the smectite structures, both indicating that the kaolinite postdate the smectite precipitation (Figures 3.18 C-D, 3.19 E and 4.13 C). The clay minerals are found along the edges of sparry calcite crystals, predating the clays before the calcite cement precipitation (Figure 4.14).

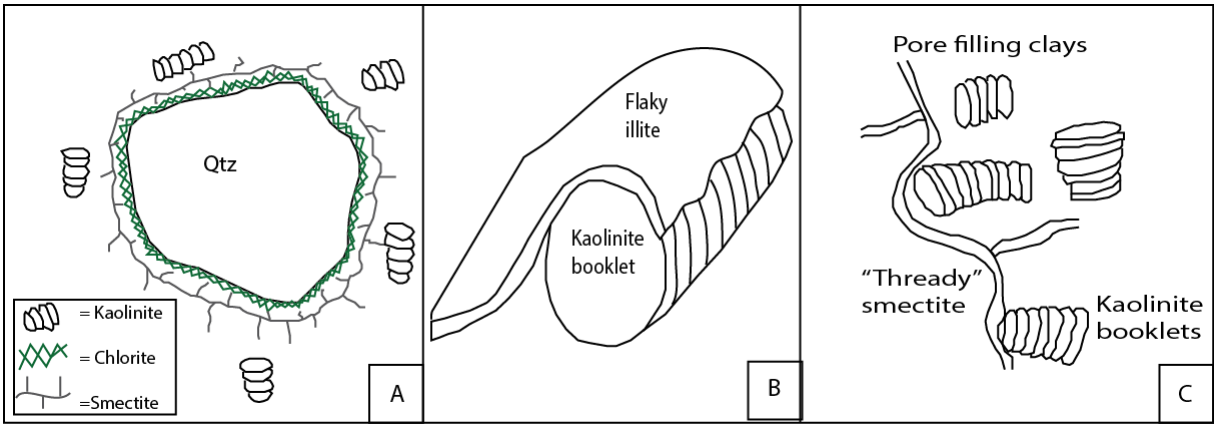

Figure 4.13: A shows the relationship between chlorite, smectite and kaolinite. Since the chlorite is found as the inner coating layer, it must have formed first, followed by the smectite. Pore filling kaolinite was formed last. B shows how the flaky illite is draped around the kaolinite booklet, postdating the illite after the kaolinite. C shows the kaolinite-smectite relationship. Notice how the growth of kaolinite booklets has displaced the thready smectite, postdating the kaolinite booklets after the smectite.

4.2.6 Streamflow and aeolian sandstones

Quantitative analyses of the samples deriving from a streamflow deposit of Permo-Triassic age or from the aeolian system (Triassic age), reveal a higher quartz/total feldspar than the ratios found for the debris flow sediments, suggesting that the sandstones have been subjected to longer transport. Thus, the sediments deposited by stream or wind, are more mature. Weathering may also have contributed to the higher ratios, where the feldspars have been dissolved and the content reduced. SEM, XRD, point counting, and optical microscopy all points to quartz being the dominating mineral in these samples. The optical analyses reveal grain size from fine to medium sand, and the grain shape range from sub-angular to sub-rounded. The different shapes of the grains may imply differences in transport length, but they have been transported longer than the sediments found in the conglomerates. The content of clastic micas and feldspars are also reduced in these samples, which supports the conclusion of a longer transportation for these sediments. Further, the sandstone samples display improved sorting, which suggests a longer transportation. The porosity found in these sediments is mostly primary porosity, but there has been observed secondary porosity linked to the dissolution of feldspars.

The feldspar content is reduced in the sandstone samples compared to the feldspar content found in the conglomeratic matrixes. In the sandstone samples, K-feldspar has the highest contribution to the total feldspar content, and seems to be more stable than the plagioclase. Thus, the K-feldspar is more resistant to dissolution during transportation. The stable K-feldspar content may indicate that the transport and deposition have been favourable of K-feldspar rich sand. Transportation is not the only mechanism that reduces the feldspar content, also weathering and dissolution needs to be considered. As during transportation, the K-feldspar is more stable than the plagioclase during weathering (Goldich, 1938) (Figure 4.12).

The high content of authigenic kaolinite booklets in sandstones from FA 2, points to subsurface alteration of feldspars and micas, leading to the precipitation of the diagenetic kaolinites. The streamflow sandstone sample has a low kaolinite content, which implies that, the subsurface alteration of micas and feldspars has been minimal, and the initiation of the chemical reaction leading to the precipitation of kaolinite did not occur. XRD, SEM, and thin section analyses reveal that the medium grained sandstone layers found in the aeolian part of FA 2, are more clay rich than the layers consisting of fine grained sandstones (compare Figure 3.13 B-C). XRD analyses display a relatively high content of kaolinite, which SEM analysis

and point counting confirm. The kaolinites are found to be fully developed booklets, indicating a diagenetic origin (Figure 3.21). A high rate of meteoric water flushing may have resulted in intense leaching of feldspars and micas in the sandstones of FA 2. The dissolved feldspars and micas may have led to the precipitation of kaolinites, in the chemical processes described in section 4.2.2. A higher kaolinite content in the medium sandstones, compared to the fine sandstones, may imply a higher rate of leaching of the precursor minerals due to meteoric pore water flow through the medium sandstone layers, due to a higher porosity and permeability at the time of deposition and at shallow burial. Heterogeneity in the sediments, may have led to different permeabilities, and meteoric flow usually tends to be focused in the more permeable sediments, as described by Bjørlykke et al. (1989). Porosity measurements provided from thin sections, display that the fine sandstone layers contain higher porosity values at present time, while the pore filling kaolinite found in the medium sandstone layers has reduced the porosity (Figure 3.13 C), and may be the reason why the medium grained sandstones display lower porosities than the fine grained sandstones.

Clay minerals in the form of chlorite, smectite, illite, and illite-smectite are also found in the sandstone layers, as seen in SEM analyses. Although the sandstones contain the same clay minerals, the content of chlorite, smectite, and illite-smectite are reduced compared to the content found in the matrixes. But the same mineral/mineral relations are found in the aeolian sandstones (Figure 4.13), as in the conglomeratic matrixes, pointing to a similar diagenetic history for the FA 1 and 2 sediments in core 16/1-13. Also in the aeolian sandstones, the clay minerals act as coating and pore fill. The decrease in chlorite and mica content observed in the XRD analysis, may be linked with the increase in distance of transportation. If muscovite and biotite have a low presence as clastic grains, little transformation can occur during burial, e.g. the biotite to chlorite transformation. SEM, XRD, and thin section analyses indicate a higher content of kaolinite and calcite in the aeolian sandstones compared to the matrix samples, meaning that the pore water would have had the necessary ions in solution, and the pH and silica content have been favourable of kaolinite.

The chlorite content is reduced in the sandstone samples, compared to the matrix samples, which is expected due to the reduction in clastic chlorite, clastic biotite and rock fragments. Compared to the matrix samples, the kaolinite content is increased in the sandstone samples deriving from the aeolian environment. This is to be expected, due to the fact that the porosity values were much higher in the sandstones, giving the meteoric pore water more room to

flush, leading to more intense leaching of feldspars and micas, resulting in the precipitation of diagenetic kaolinite. The calcite content is also increased in the sandstone samples, also supporting the theory with a higher porosity, giving the pore water more ease to flow. The calcite cement is found to grow in the pores not filled with clays in the aeolian sandstones and fragments of clay minerals can be observed along the edges of the calcite crystals, indicating that the calcite postdates the clay mineral precipitation (Figure 4.14). No hematite is present in the XRD analyses for the stream and aeolian sediments, indicating that oxidising reactions did not occur or were not frequent during the deposition of these sediments, but Fe-oxides has been observed during optical analyses (Figure 3.13 A-B). Fe-oxides are also found as grain coatings and as Fe-oxide overgrowths in the aeolian sandstones (Figure 3.13 A-B), where the grain coating may derive from oxidising conditions linked to deposition, while the overgrowth may be diagenetic. The Fe-oxide overgrowth observed in the aeolian fine sandstone (Figure 3.13 A), may have been precipitated at a time of oxidising conditions, linked to uplift, or it may originate from recrystallization of Fe-oxides during burial. The Fe-oxide features found in the aeolian sandstones are visually different than the Fe-oxides found in the alluvial fan system of 16/1-13. The aeolian Fe-oxides coatings are yellow and not red, and the overgrowth has different texture than the Fe-oxides found in the conglomeratic matrixes (compare Figures 3.11 and 3.13). These differences may point to different origins of the Fe-oxides found in the matrixes and the Fe-oxide found in the aeolian sandstones. The amount of Fe-oxides is low, and the reason for hematite not being recognized during XRD, may have been that the amount was under the detection limit. The presence of halite and sylvite in the samples, are probably not a depositional or diagenetic effect, they have most likely derived during drilling, as contaminants from the drilling mud (Dypvik, 1981).

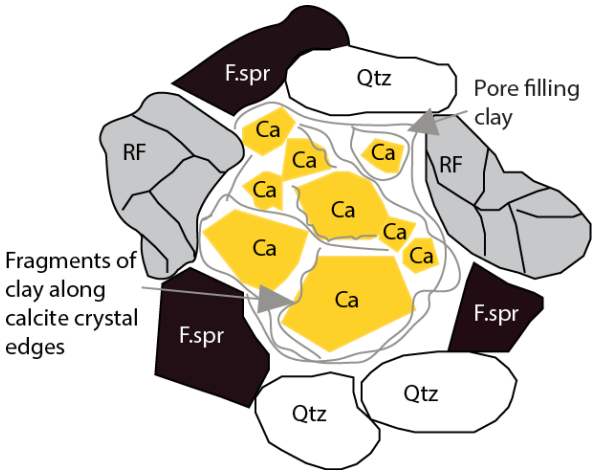

Figure 4.14: An illustrative sketch showing the relationship between the framework minerals (Qtz, F.spr, RF), the euhedral, sparry calcite (Ca) and the pore filling clays found in both the aeolian sandstones and the conglomeratic matrixes. Notice the clay fragments along the calcite crystal edges.

4.2.7 Polycrystalline quartz fragments

The presence of both granitic rock fragments and polycrystalline quartz fragments of a more gneissic origin reflects the presence of at least two different provenance areas. The difference in size and degree of rounding between the polycrystalline quartz fragments and the other

grains found in the matrixes and the aeolian sandstones, indicate that the polycrystalline quartz have had a longer transport period. The polycrystalline quartz fragments have a higher abundance in the aeolian sandstones, suggesting that the source for these fragments was more active during the deposition of the aeolian sandstones, than during the deposition of the alluvial fan sediments. The polycrystalline quartz fragments are found to have a high abundance in the red matrix as well, which may point to similar source areas for the red matrix sediments and the aeolian sandstones.

4.2.8 Overgrowths

Authigenic K-feldspar demands a supply of potassium, aluminium and silicon ions to be formed in the diagenetic environment (Waugh, 1978). The source of these ions may come from the more unstable minerals e.g. plagioclase, ferromagnesian silicates, and rock fragments composed of these minerals, (see the stability series of Goldich, 1938, Figure 4.12). As observed by optical microscopy and SEM, these unstable minerals tend to be dissolved and have been replaced by clay minerals. Dissolution and replacement of silicate minerals, will lead to the release of some, or all of their constituent elements into the circulating water. The fate of the released elements depends on the chemical conditions found in the pore solution. The elements may remain in solution and circulate with the groundwater, or they may precipitate as authigenic minerals that are in equilibrium with the existing diagenetic environment (Waugh, 1978). The latter case is considered to have caused the authigenic K-feldspar overgrowths found in FA 1 and 2 in core 16/1-13. Fe-oxide overgrowth and K-feldspar overgrowth are found to predate the calcite cement in both FA 1 and 2, as the calcite cement is found to grow onto both types of overgrowths and not the clastic grains (Figures 3.12 C-D, 3.13 A, 4.15 and 4.16). Both types of overgrowths are interpreted to postdate the precipitation of clay minerals, because the overgrowths are found to not grow in areas where clay minerals are in contact with the clastic grains (Figure 4.16).

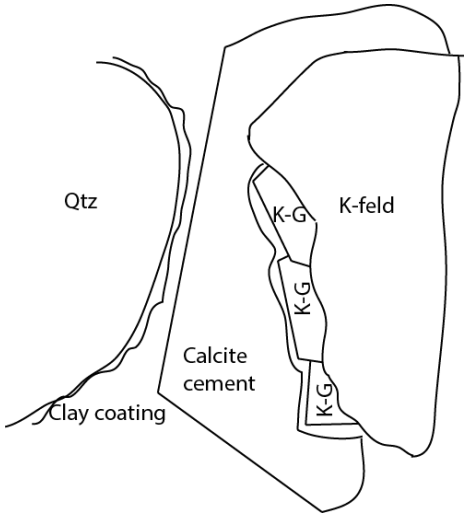

Figure 4.15: A sketch showing the relationship between calcite cement and authigenic K-feldspar overgrowth (K-G). The calcite cement is found to grow onto the authigenic K-feldspar, pointing to calcite postdating the authigenic K-feldspar.

Quartz overgrowth has been observed during SEM, EMP and optical microscopy, in sediments from FA 1 and 2, but they do not appear to occur frequently. According to Waugh

(1978), precipitation of authigenic illite and feldspar will enrich the groundwater with regards to minerals like calcium, silicon and bicarbonate ions. These ions may eventually precipitate as quartz overgrowths (Waugh, 1978). The overgrowths of quartz may have been formed as a result of the precipitation of the authigenic illite and feldspar found in both FA 1 and 2, where the groundwater may have been enriched with the necessary ions.

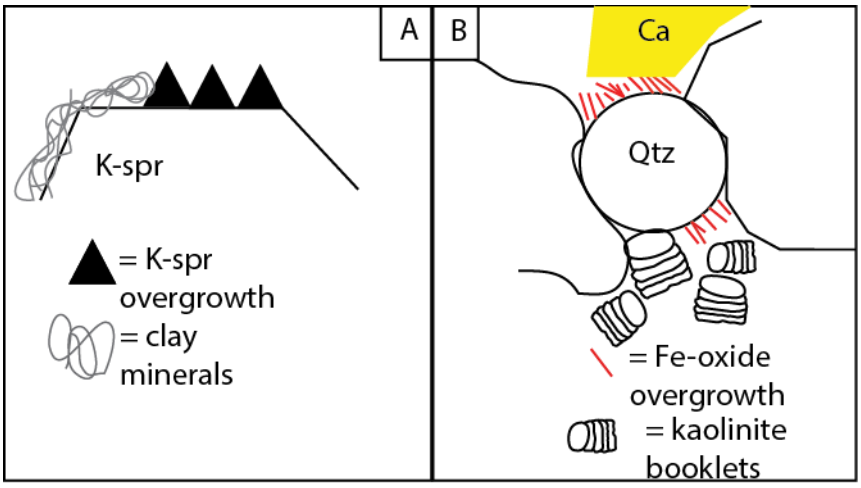

Figure 4.16: The relationship between the K-feldspar overgrowth and clay minerals found in both the conglomeratic matrixes and the aeolian sandstones are displayed in Figure A. The K-feldspar overgrowth has been found to not grow, or have severely reduced capacity to grow in areas with clay coating, indicating that the authigenic K-feldspar overgrowth postdates the clay mineral formation. Figure B displays the relationship between the Fe-oxide overgrowth found in the aeolian sandstones, clay minerals and calcite cement. The Fe-oxides are found to not grow in areas where clay minerals are found, pointing to Fe-oxide overgrowth postdating the clay mineral formation. The relation between the Fe-oxide overgrowth and calcite cement is also displayed, pointing to calcite postdating the Fe-oxide overgrowth.

4.2.9 Carbonate cement

The precipitation of K-feldspar and quartz overgrowths is often followed by calcite cementation (Waugh, 1978). Observations encountered during optical microscopy of sediments from both FA 1 and 2, show sparry calcite cement growing onto K-feldspar overgrowths (Figures 3.12 C-D and 4.15). SEM analyses of the sparry calcite cement reveal a very low Mg content, indicating that the calcite is low-magnesium sparry calcite, the most stable calcite structure. The carbonate cement was found to have euhedral crystal shape, indicating a diagenetic origin, and they were found to postdate the clay mineral precipitation and the formation of all types of overgrowths observed in the samples from both FA 1 and 2 in core 16/1-13 (Figures 4.14, 4.15 and 4.16). Clay minerals fragments could be observed along some of the calcite crystal edges, and most importantly, carbonate cement were found to grow onto clay mineral coatings and overgrowths. Carbonate cement and quartz overgrowth has not been observed together, but based on comparable observations by Waugh (1978), on Permo-Triassic British sandstones, quartz overgrowth most likely predates the carbonate cement found in sediments from the alluvial fan and aeolian systems.

The rhombic dolomite cement found in two of the samples (basement clast and conglomeratic matrix, Figure 3.17), may indicate that the groundwater had a favourable composition of dolomitisation at the expense of calcite cement precipitation. Dolomite is found to precipitate during times of high Mg^{2+}/Ca^{2+} rations, low Ca^{2+}/CO_3^{2-}, high temperature, low salinities, and where fluids release CO_2 (Machel and Mountjoy, 1986), meaning that the groundwater must have been Mg rich at the time of the precipitation of the dolomite cement.

4.2.10 Summary of the diagenetic history

To sum up, the following diagenetic history can be found in core 16/1-13 (Table 4.1).

Table 4.1: A summary of the diagenetic features found in core 16/1-13. X points to the diagenetic feature being present in the respective facies association, while – points to absence of the diagenetic feature in the facies associations.

Diagenetic features	FA 1	FA 2
Mechanical compaction	X	X
Dissolution of feldspar and mica	X	X
Authigenic chlorite	X	X
Authigenic smectite and illite-smectite	X	X
Authigenic kaolinite	X	X
Smectite-illite transformation leading to the formation of illite	X	X
Second and third Fe-oxide phases	X	-
Fe-oxide overgrowth	-	X
K-feldspar overgrowth	X	X
Quartz overgrowth	X	X
Sparry, euhedral calcite cement	X	X
Rhomib, dolomite cement	X	-

4.2.11 Comments

Grains in core 16/1-13 are found to show little signs of compaction, indicating that the mechanical compaction has been minimal, even though the sediments have been buried to a depth of around 2 km. The light cracking and bending of the kaolinite booklets and biotite grains, indicate that there has been weak compaction in the area (Figures 4.4 and 4.7 A).

The use of EMP on K-feldspar for provenance studies illustrated small differences in the K-feldspars composition. If a sample from onshore Norway were tested, the results would probably be similar (pers.com. M. Erambert, 2015). Hence, K-feldspar mineralogy has not been proven useful for provenance studies. Isotope analysis and heavy mineral analysis would probably have given more information, and is worth considering in later analyses. Even though EMP analyses did not give any answer to the question regarding provenance area, it

did show a mineralogical difference between the detrital K-feldspar grains and the K-feldspar overgrowths. The detrital grains had a varying content of sodium, due to the exsolution of albite found in the K-feldspar. The perthite lamellae displayed varying extent and sizes, leading to the differences in sodium content during the analyses. Differences in barium and calcium content were also observed. When testing the overgrowths, a mineralogical composition close to pure potassium feldspar was found. This indicates that the overgrowth formed at low temperatures, when the mineral phases could not blend (Winter, 2010).

The Cretaceous carbonates have not been studied in any detail in this thesis. The carbonates are only a part of the generated log.

5. Conclusion

The Edvard Grieg Field is located in a half-graben rift basin, where sediments from the Permo-Triassic and Early Cretaceous make up the stratigraphy found in core 16/1-13. Three different depositional environments have been recognised, and they represent alluvial fan, aeolian sandstones and marine carbonates. The alluvial fan is represented by alternating layers of a grain supported debris flows and streamflow deposits. The alluvial fan developed from being debris flow dominated, to being streamflow dominated, which implies that the alluvial fan retreated, possibly linked to the termination of rifting and the corresponding decline in sediment supply from the hinterlands. In a depth interval from 1967-1944.70 m, the aeolian sandstones is interfingering with coarse grained sandstones, possibly originating from a braided river, linked to the alluvial plain area. After 1944.70 m, the Triassic aeolian sandstone dominates. The marine carbonates found in the upper most part of the core represent the Åsgard Formation, and is of Early Cretaceous age. The sudden shift from aeolian sandstone of Triassic age to marine carbonates of Cretaceous age, indicate that the Jurassic strata is missing from the area, and may have been eroded during the Mid-Jurassic doming.

Eroded basement clasts are found to represent varying degrees of weathering, and observations have confirmed the presence of authigenic clay minerals and carbonate cement. The origin of these clays and carbonates, have been challenging to answer, and no absolute answer has been found. The presence of rhombic dolomite, may point to the clast being subjected to alteration linked to diagenesis. The varying degrees of weathering of the individual basement clasts, may point to weathering in the source area. These observations may point to the clasts being subjected to both sub-aerial weathering and diagenesis.

The conglomeratic matrixes, which may be reworked products of paleo-weathering profiles, contain clay minerals, which constitute only a small fraction of the bulk composition. The presence of well-developed structures of the clay minerals, point to an authigenic appearance of the clay minerals. The delicacy of these clay mineral structures, demonstrates a diagenetic origin, and not originating from the weathering profiles, followed by transportation and reworking. The matrixes have further been subject to alteration during burial, possibly linked to the dissolution of feldspars and micas by meteoric water flushing or by recrystallization of detrital clay minerals. Multiple layers of coating and pore filling clay have been found, and their relationship has been used to interpret the evolution of the diagenetic history.

Results from XRD, SEM and optical microscopy analyses, reveal nearly similar mineralogy for the matrix samples from the alluvial fan facies in core 16/1-13. The differences between the matrixes are minor, indicating that the parent rock composition, the depositional conditions and burial history may have been quite similar for the three matrixes. The matrixes are found to display the same diagenetic history, since they contain the same diagenetic features and the same mineral/mineral relations. The results obtained here, only derive from the data available during this study, and further studies should be conducted to see if similar results are found and to quality check the findings. The variation in the abundance of clasts and their respective sizes, may point to changing conditions during deposition, possibly linked to changes in transport and supply from the provenance areas. The colour difference implies deposition in environments with varying iron content, qualities of iron and oxygenising conditions. The high content of unstable minerals, relatively low quartz/total feldspar, and the poorly sorting indicate that the matrixes are fairly immature sediments.

The aeolian sediments have a lower abundance of unstable minerals, relatively high quartz/total feldspar, and good sorting. This point to more mature sediment, which has experienced longer transport, compared to the conglomeratic matrix sediments. The same clay minerals, and the same mineral/mineral relations observed in the conglomeratic matrixes, are identified in the sandstones as well. This suggests that the sediments in core 16/1-13 have been subjected to the same diagenetic history. Higher kaolinite content in the aeolian sandstones, compared to the conglomeratic matrixes, may be linked to the original higher porosity and permeability values found in these sediments. The pore water has also been favourable for kaolinite precipitation, at the expense of the other clay minerals observed. The kaolinite has been found to reduce the porosity in the medium grained sandstone layers of the aeolian sandstones.

The feldspar minerals display varying degrees of alteration and dissolution, and carry indications of at least two provenance areas. This is also confirmed by the basement clasts. The distribution of polycrystalline quartz fragments of both gneissic and igneous origin also suggests multiple source areas. The feldspar minerals may have been exposed to alteration in both the source area and during burial. Most of the weathering has probably been located in the source areas, but the appearance and behaviour of the clay minerals, indicate a diagenetic origin, meaning that subsurface alteration must have been present. Micas are also capable of creating clays, and they show signs of dissolution and alteration to kaolinite and chlorite.

References

Aagaard, P. and Helgeson, H.C. 1982. Thermodynamic and kinetic constraints on reaction rates among minerals and aqueous solutions, I, Theoretical considerations. *American Journal of Science* 282, 237-285.

Agha, M.A., Ferrell, R.E., Hart, G.F., Abu El Ghar, M.S. and Abdel-Motelib, A. Mineralogy of Egyptian Bentonic Clays II: Geologic Origin. *Clays and Clay Minerals* 61(6), 551-565.

Badley, M.E., Price, J.D., Rambech, D.C. and Agdestein, T. 1988. The structural evolution of the northern Viking Graben and its bearing upon extensional modes of basin formation. *Journal of the Geological Society of London* 145(3), 455-472. DOI: 10.1144/gsjgs.145.3.0455

Bjørlykke, K., Ramm, M. and Saigal, G.C. 1989. Sandstone diagenesis and porosity modification during basin evolution. *Geologische Rundschau* 78(1), 243-268.

Bjørlykke, K. 1998. Clay mineral diagenesis in sedimentary basins – a key to the prediction of rock properties. Examples form the North Sea Basin. *Clay Minerals* 33, 15-34.

Blair, T.C. and McPherson, G. 2009. Processes and Forms on Alluvial fans. *In*: Parsons, A.J. and Abrahams, A.D. (eds.): *Geomorphology of Desert Environments, Second Edition.* Springer Science+Business Media B.V., 413-467. DOI: 10.1007/978-1-4020-5719-9

Boggs, S. J. 2011. *Principles of Sedimentology and Stratigraphy, fifth edition.* Upper Saddel River, New Jersey: Pearson Education, Inc. 585 p.

Brekke, H., Sjulstad, H.I., Magnus, C. and Williams, R.W. 2001. Sedimentary environments offshore Norway – an overview. *In:* Martinsen, O.J. and Dreyer, T. (eds): *Sedimentary Environments Offshore Norway – Palaeozoic to Resent.* NPF Special Publications 10. Elsevier Science B.V, 7-37. DOI:10.1016/S0928-8937(01)80006-0

Bruker. 2011. *Diffrac.Suite. User Manual. Original Instructions.* Bruker AXS GmbH. 162 p.

Bull, W. 1972. Recognition of alluvial-fan deposits in the stratigraphic record. *In:* Rigby, J.K. and Hamblin, W.K. (eds.): *Recognition of Ancient Sedimentary Environments* 16, 63-83. Society of Economic Paleontologists and Mineralogists (SEPM).

Collinson, J. D, Mountney, N. P. and Thompson, D. B. 2006. *Sedimentary Structures, third edition*. Harpenden, Hertfordshire, England: Terra Publishing. 292 p.

Compton, R.R. 1962. Manual of Field Geology. In *Soil Science*. New York: Wiley. 295 p.

Coward, M.P. 1993. The effect of Late Caledonian and Variscan continental escape tectonics in basement structure, Palaeozoic basin kinematics and subsequent Mesozoic basin development in NW Europe. *In:* Parker, J.R (ed): *Petroleum Geology of Northwest Europe: Proceedings of the 4th Conference.* London: The Geological Society of London, 1095-1108. DOI: 10.1144/0041095

Coward, M.P., Dewey, J., Mange, M.A., Hempton, M. and Holroyd, J. 2003. Tectonic evolution. *In*: Evans. D., Graham, C., Armour, A. and Bathurst, P. (eds): *The Millennium Atlas: Petroleum Geology of the Central and Northern North Sea*. London: The Geological Society of London, 17-33.

Dalland, A., Worsley, D. and Ofstad, K. 1988. *A lithostratigraphic scheme for the Mesozoic and Cenozoic succession offshore mid- and northern Norway*. Oljedirektoratet, 65 p.

Deegan, C. E. and Scull, B. J. 1977. *A standard lithostratigraphic nomenclature for the Central and Northern North Sea. UK Institute of Geological Sciences, Report 77/25*. Oljedirektoratet, 36 p.

Doré, A.G. 1991. The structural foundation and evolution of Mesozoic seaways between Europe and the Artic. *Palaeogeography, Palaeoclimatology, Palaeooceanography* 87, 441-492. DOI: http://dx.doi.org/10.1016/0031-0182(91)90144-G

Downie, R. 1998. Devonian. *In:* Glennie, K.W. (ed.): *Petroleum Geology of the North Sea: Basic Concepts and Recent Advances, Fourth Edition.* Blackwell Science Ltd, 85-103. DOI: 10.1002/9781444313413.ch3

Dypvik, H. 1981. Drilling Mud Contamination of Samples in X-Ray Diffraction and Atomic Absorption Analyses. *The American Association of Petroleum Geologists* 65(4), 744-748.

Fisher, M.J. and Mudge, D.C. 1998. Triassic. *In*: Glennie, K.W. (ed): *Petroleum Geology of the North Sea: Basic Concepts and Resent Advances, Fourth Edition*. Blackwell Science Ltd, 212-244. DOI: 10.1002/9781444313413.ch7

Fossen, H. and Hurich, C.A. 2005. The Hardangerfjord Shear zone in SW Norway and the North Sea: a large-scale low-angle shear zone in the Caledonian crust. *Journal of the Geological Society, London* 162, 675-687.

Freytet, P. and Plalziat, J.C. 1982. Continental carbonate sedimentation and pedogenesis-Late Cretaceous and Early Tertiary of southern France. *In:* Purser, B.H. (ed.):*Contributions to Sedimentology, 12.* Stuttgart: Schweizerbart, 110 p.

Færseth, R.B. 1996. Interaction of Permo-Triassic and Jurassic extensional fault-blocks during the development of the northern North Sea. *Journal of the Geological Society* 153(6), 931-944. DOI: 10.1144/gsjgs.153.6.0931

Galán, E. 2006. Genesis of clay minerals. *In:* Bergaya, F., Theng, B.K.G. and Lagaly, G. (eds.): *Handbook of Clay Science.* Oxford: Elsevier Ltd, 1129-1162.

Galán, E. and Ferrell, R.E. 2013. Genesis of Clay Minerals. *In:* Bergaya, F. and Lagaly, G. (eds.): *Handbook of Clay Science, 2nd edition, Part A.* Oxford: Elsevier Ltd, 83-126.

Gee, D.G., Fossen. H., Henriksen, N. and Higgins, A. 2008. From the Early Paleozoic Platforms of Baltica and Laurentia to the Caledonide Orogen of Scandinavia and Greenland. *Epiodes* 31(1), 44-51.

Glennie, K.W. and Underhill, J.R. 1998. Origin, Development and Evolution of Structural Styles. *In*: Glennie, K.W. (ed): *Petroleum Geology of the North Sea: Basic Concepts and Resent Advances, Fourth Edition*. Blackwell Science Ltd, 42-84. DOI: 10.1002/9781444313413.ch2

Glennie, K.W. 1998. Lower Permian- Rotliegend. *In*: Glennie, K.W. (ed): *Petroleum Geology of the North Sea: Basic Concepts and Resent Advances, Fourth Edition*. Blackwell Science Ltd, 137-211. DOI: 10.1002/9781444313413.ch5

Goldich, S. S. 1938. A Study in Rock-Weathering. *The Journal of Geology* 46(1), 17–58. DOI: 10.2307/30079586

Goldsmith, P. J., Hudson, G. and Van Veen, P. 2003. Triassic. *In*: Evans. D., Graham, C., Armour, A. and Bathurst, P. (eds): *The Millennium Atlas: Petroleum Geology of the Central and Northern North Sea*. London: The Geological Society of London, 105-127.

Gregersen, U. 1997. Stratigraphy and facies distribution of the Utsira Formation and the Pliocene sequences in the northern North Sea. *Marine and Petroleum Geology* 14(7–8), 893–914.

ISRM. 1978. Methods for the quantitative description of rock masses and discontinuities. *International Journal of Rock Mechanics, Mining, Science and Geomechanics* 15, 319-368.

Isaksen, D. and Tonstad, K. 1989. *A revised Cretaceous and Tertiary lithostratigraphic nomenclature for the Norwegain North Sea.* Oljedirektoratet, 59 p.

Isaksen, G.H. and Ledje, K.H.I. 2001. Source rock quality and hydrocarbon migration pathways within the greater Utsira High area, Viking Graben, Norwegian North Sea. *AAPG Bulletin* 85(5), 861-883.

Jackson, M.L. and Sherman, G.D. 1953. Chemical weathering of Minerals in Soils. *Advances in Agronomy* 5(22), 219-318. DOI:10.1016/S0065-2113(08)60231-X

Jackson, C.A.L., Kane, K.E. and Larsen, E. 2010. Structural evolution of minibasins on the Utsira High, northern North Sea; implications for Jurassic sediment dispersal and reservoir distribution. *Petroleum Geoscience* 16, 105-120. DOI: 10.1144/1354-079309-011

Lanson, B., Beaufort, D., Berger, G., Bauer, A., Cassagnabère, A. and Meunier, A. 2002. Authigenic kaolin and illitic minerals during burial diagenesis of sandstones: a review. *Clay Minerals* 33, 1-22. DOI: 10.1180/0009855023710014

Lervik, K.S. 2006. Triassic lithostratigraphy of the Northern North Sea Basin. *Norwegian Journal of Geology* 86, 93-116.

Lobb, G.L. 1949. Red Bed Coloration. *Journal of Sedimentary Petrology* 19(3), 99-103.

Lundin Norway. 2015. *Edvard Grieg*. Available at: http://www.lundin-norway.no/en/project/edvard-grieg/. Accessed: 12.03.2015.

Machel, H.G. and Mountjoy, E.W. 1986. Chemistry and Environments of Dolomitiztion – A Reappraisal. *Earth-Science Reviews* 23, 175-222.

McClay, K.R., Norton, M.G., Coney, P. and Davis, G.H. 1986. Collapse of the Caledonide Orogen and the Old Red Sandstone. *Nature* 323, 147-149. DOI: 10.1038/323147a0

McKie, T. and Williams, B. 2009. Triassic palaeogeography and fluvial dispersal across the northwest European Basins. *Geological Journal* 44, 711-741. DOI: 10.1002/gj.1201

Miall, A. 2010. Alluvial Deposits. *In:* James, N.P and Dalrymple, R.W. (eds): *Facies Models 4.* Newfoundland and Labrador, Canada: Geological Association of Canada, 105-137.

Moore, D.M. and Reynolds, R.C. 1997. *X-Ray Diffraction and the Identification and Analysis of Clay Minerals*. Oxford: Oxford University Press, 378 p.

Morton, A.C. and Hallsworth, C.R. 1999. Processes controlling the composition of heavy mineral assemblages in sandstones. *Sedimentary Geology* 124, 3-29. DOI:10.1016/S0037-0738(98)00118-3

Mountney, N.P. 2006. Eolian Facies Models. *SEPM Special Publications* 84, 19-83. DOI: 10.2110/pec.06.84.0019

Nemec, W. and Steel, R.J. 1984. Alluvial and coastal conglomerates: their significant features and some comments on gravelly mass-flow deposits. *In:* Koster, E.H. and Steel, R.J. (eds.): *Sedimentology of Gravels and Conglomerates, Memoir 10.* Canadian Society of Petroleum Geologists, 1-31

Nesbitt, H.W. and Young, G.M. 1989. Formation and Diagenesis of Weathering Profiles. *The Journal of Geology* 97(2), 129-147.

Nichols, G. 2009. *Sedimentology and Stratigraphy.* Wiley-Blackwell, 419 p.

Nickel, E. 1985. Carbonates in alluvial fan systems. An approach to physiography, sedimentology and diagenesis. *Sedimentary Geology* 42, 83-104.

Nickling, W.G. 1994. Aeolian sediment transport and deposition. *In*: Pye, K. (ed): *Sediment Transport and Depositional Processes.* Oxford: Blackwell Science, 293-350.

Nilsen, T.H. 1982. Alluvial Fan Deposits. *In*: Scholle, P.A and Spearing, D. (eds): *Sandstone Depositional Environments*. American Association of Petroleum Geologists Memoir 31, 49-86.

NPD, 2015, a. *Factpages*. Available at: http://factpages.npd.no/factpages/Default.aspx?culture=no. Accessed: 27.04.2015.

NPD, 2015, b. *Geology of the North Sea.* Available at: http://www.npd.no/Global/Norsk/3-Publikasjoner/Rapporter/Samleatlas/Figurer-Figures/Chapter-4/Fig-4-002.pdf. Accessed: 20.03.2015.

Nystuen, J.P., Kjemperud, A.V., Müller, R., Adestål, V. and Schomacker, E.R. 2014. Late Triassic to Early Jurassic climatic change, northern North Sea region: impact on alluvial architecture, palaeosoils and clay mineralogy. *IAS Special Publications* 46, 59-100. DOI: 10.1002/9781118920435.ch3

Nøttvedt, A., Johannessen, E.P., and Surlyk, F. 2008. The Mesozoic of Western Scandinavia and East Greenland. *Episodes* 31(1), 59-65.

Potter, P.E., Maynard, J.B. and Pryor, W.A. 1980. *Sedimentology of shale: study guide and reference source*. New York: Springer, 306 p.

Potter, P.E., Maynard, J.B. and Depetris, P.J. 2005. *Mud and Mudstones: Introduction and Overview.* Berlin, Heidelberg: Springer-Verlag Berlin Heidelberg, 297 p.

Powers, M.C. 1953. A New Roundness Scale for Sedimentary Particles. *Journal of Sedimentary Petrology* 23(2), 117-119.

Profex. 2015. *Lecture Handouts: Lesson 1: XRD and Rietveld Refinement*. Available at: http://profex.doebelin.org/?page_id=68. Accessed: 12.03.2015.

Pye, K. 1987. *Aeolian Dust and Dust Deposits.* London: Academic Press, 334 p.

Rachocki, A. 1981. *Alluvial Fans: an attempt at an empirical approach.* Chichester: Wiley, 161 p.

Selvikvåg, B. 2012. *Sedimentology and facies analysis of the Late Triassic Luno Conglomerate Member of the Skagerrak Formation, southern Viking Graben, North Sea.* Masters, Bergen: Department of earth science, University of Bergen, 140 p.

Spencer, A. and Larsen, V.B. 1990. Fault traps in the Northern North Sea. *In*: Hardman, R. F. P. and Brooks, J. (eds.): *Tectonic Events Responsible for Britain's Oil and Gas Reserves, 1990*. Geological Society of London. Geological Society Special Publication 55, 281-298. DOI: 10.1144/gsl.sp.1990.055.01.13

Stoch, L. and Sikora, W. 1976. Transformation of micas in the process of kaolinitization of granites and gneisses. *Clays and Clay Minerals* 24, 156-162.

Streckeisen, A. L., 1967. Classification and nomenclature of igneous rocks. Final report of an inquiry. *Neues Jahrbuch fur Mineralogie, Abhandlungen* 107, 144-240.

Tardy, Y., Bocquier, G., Paquet, H. and Millot, G. 1973. Formation of clay from granite and its distribution in relation to climate and topography. *Geoderma* 10(4), 271-284.

Thiry, M. 2000. Palaeoclimatic interpretation of clay minerals in marine deposits: an outlook from the continental origin. *Earth-Science Reviews* 49, 201-221.

Tomlinson, C.W. 1916. The origin of red beds. *American Journal of Science* 24, 153-179.

Velde, B. and Meunier, A. 2008. *The Origin of Clay Minerals in Soils and Weathered Rocks.* Berlin Heidelberg: Springer-Verlag, 406 p.

Vollset, J. and Doré, A.G. 1984. *A revised Triassic and Jurassic lithostratigraphic nomenclature for the Norwegian North Sea*. Oljedirektoratet, 53 p.

Waugh, B. 1978. Authigenic K-feldspar in British Permo-Triassic sandstones. *Journal of the Geological Society* 135(1), 51-56.

Weaver, C.E. 1989. Clays, Muds, and Shales. *Developments in Sedimentology 44*. Amsterdam: Elsevier, 819 p.

Wentworth, C.K. 1922. A scale of grade and class terms for clastic sediments. *Journal of geology* 27, 377-392.

Wilson, M.D. and Pittman, E.D. 1977. Authigenic clays in sandstones: recognition and influence on reservoir properties and paleoenvironmental analysis. *Journal of Sedimentary Petrology* 47(1), 3-31.

Winter, J. D. 2010. *Principles of Igneous and Metamorphic Petrology.* New Jersey: Pearson Education Inc, 702 p.

Zanella, E. and Coward, M.P. 2003. Structural framework. *In*: Evans. D., Graham, C., Armour, A. and Bathurst, P. (eds.): *The Millennium Atlas: Petroleum Geology of the Central and Northern North Sea*. London: The Geological Society of London, 45-59.

Ziegler, P.A. 1992. North Sea rift system. *Tectonophysics* 208(1-3), 55-75. DOI:10.1016/0040-1951(92)90336-5.

Appendix A –Sedimentological log

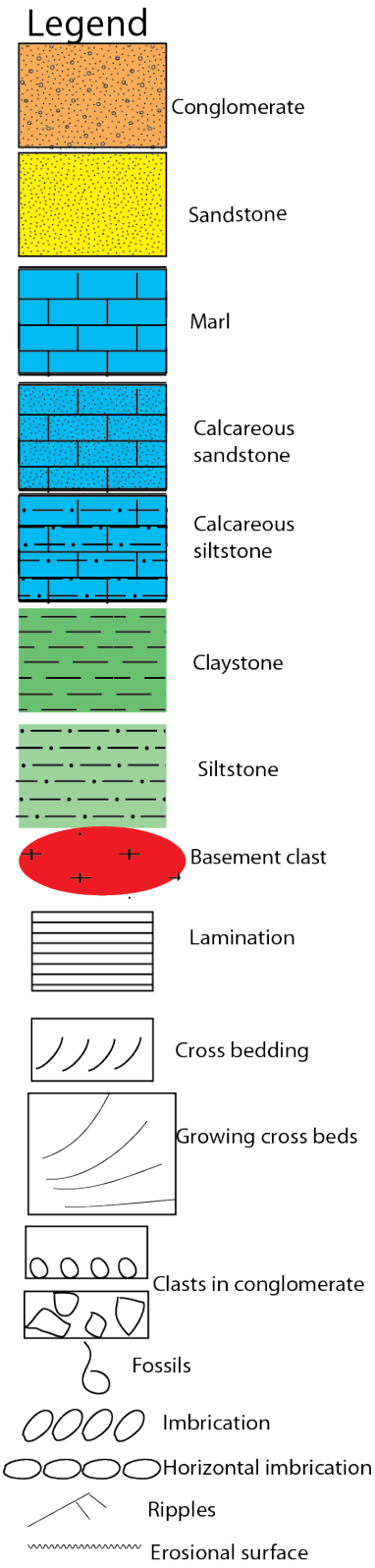

Figure 1: The legend used during logging. The legend is used in the following sedimentological logs.

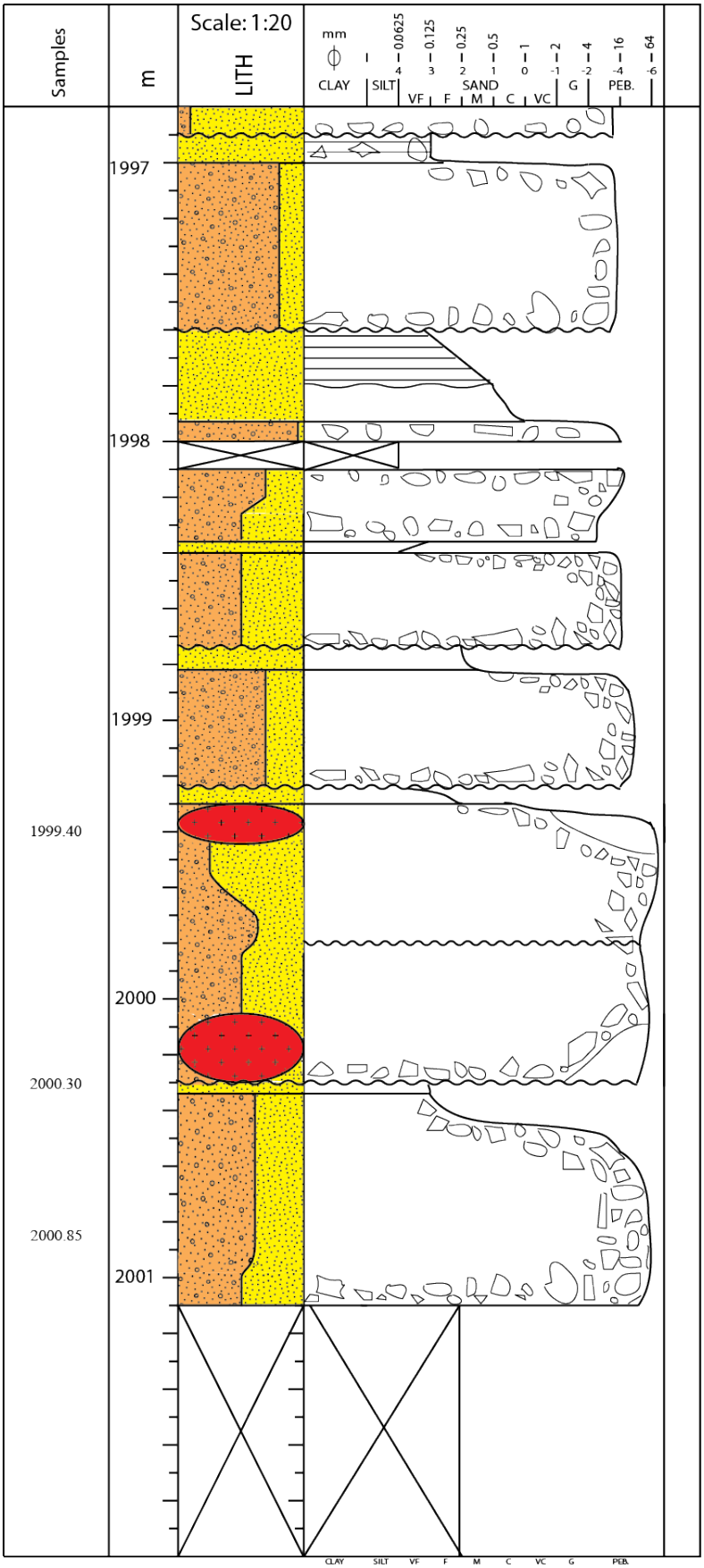

16/1-13 - page 1

Figure 2: The sedimentological log displays the alternating layers of conglomerates and sandstones from FA 1. The log section represents depth levels 2001.10-1996.80 m. The scale is 1:20. Samples are marked to the left.

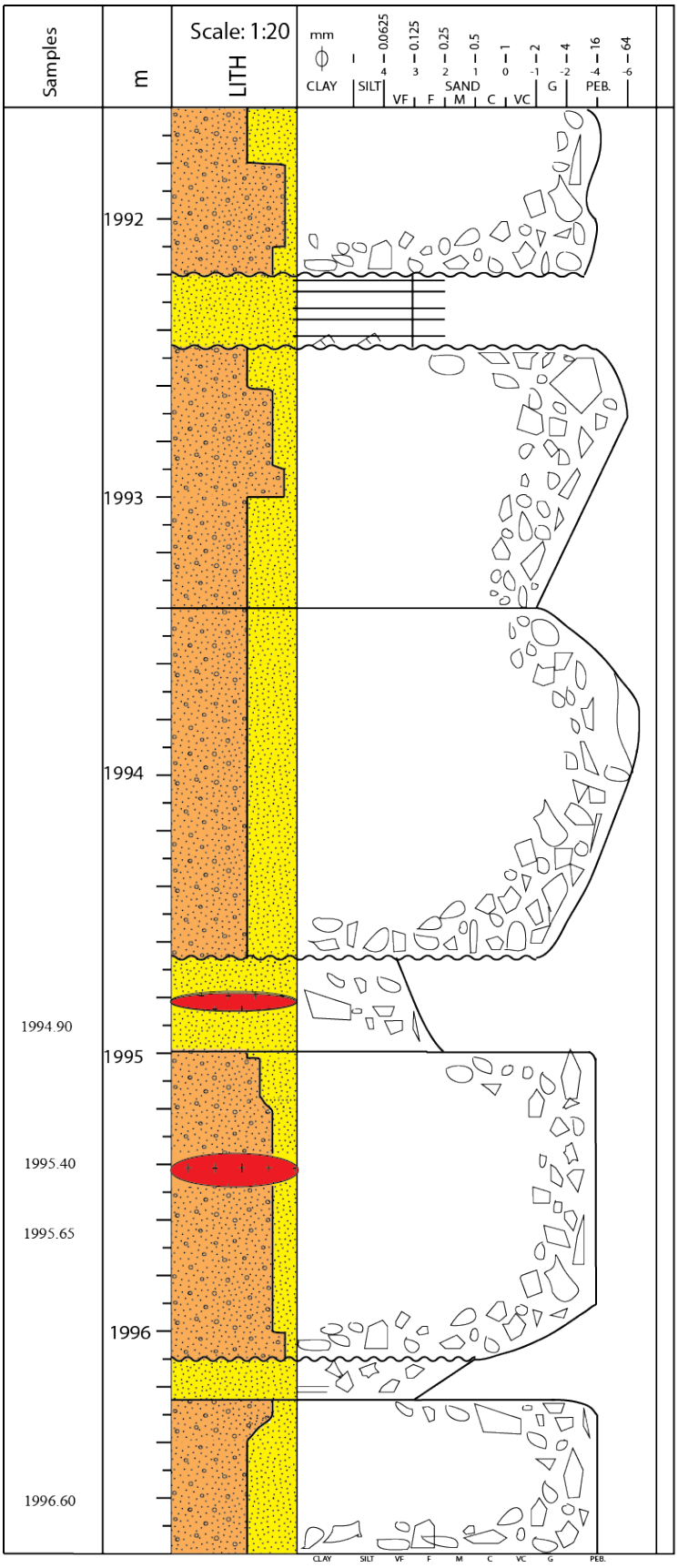

Figure 3: The sedimentological log displays the alternating layers of conglomerates and sandstones from FA 1. The log section represents depth levels 1996.80-1991.60 m. The scale is 1:20. Samples are marked to the left.

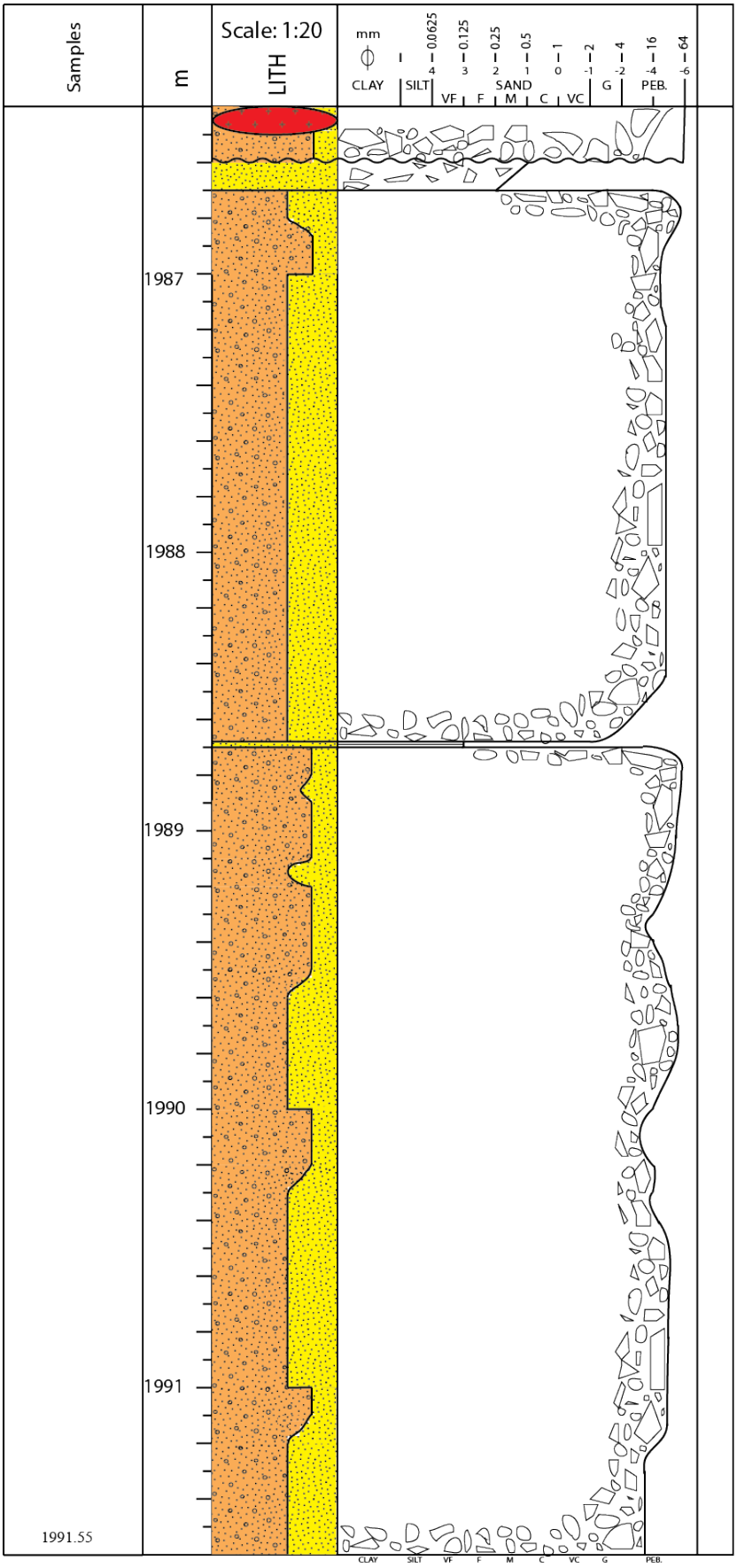

16/1-13 - page 3

Figure 4: The sedimentological log displays the alternating layers of conglomerates and sandstones from FA 1. The log section represents depth levels 1991.60-1986.40 m. The scale is 1:20. Samples are marked to the left.

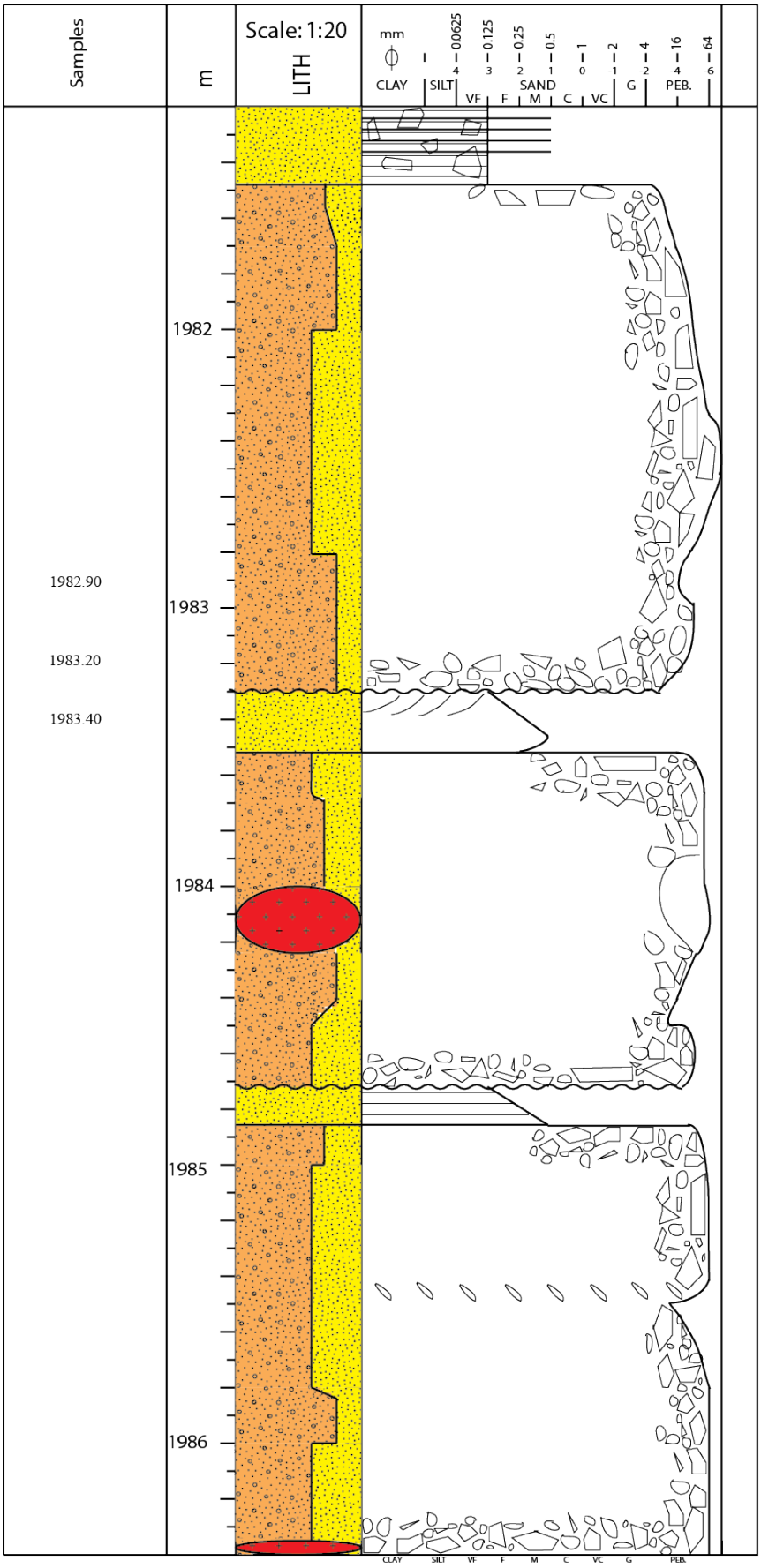

Figure 5: The sedimentological log displays the alternating layers of conglomerates and sandstones from FA 1. The log section represents depth levels 1986.40-1981.20 m. The scale is 1:20. Samples are marked to the left.

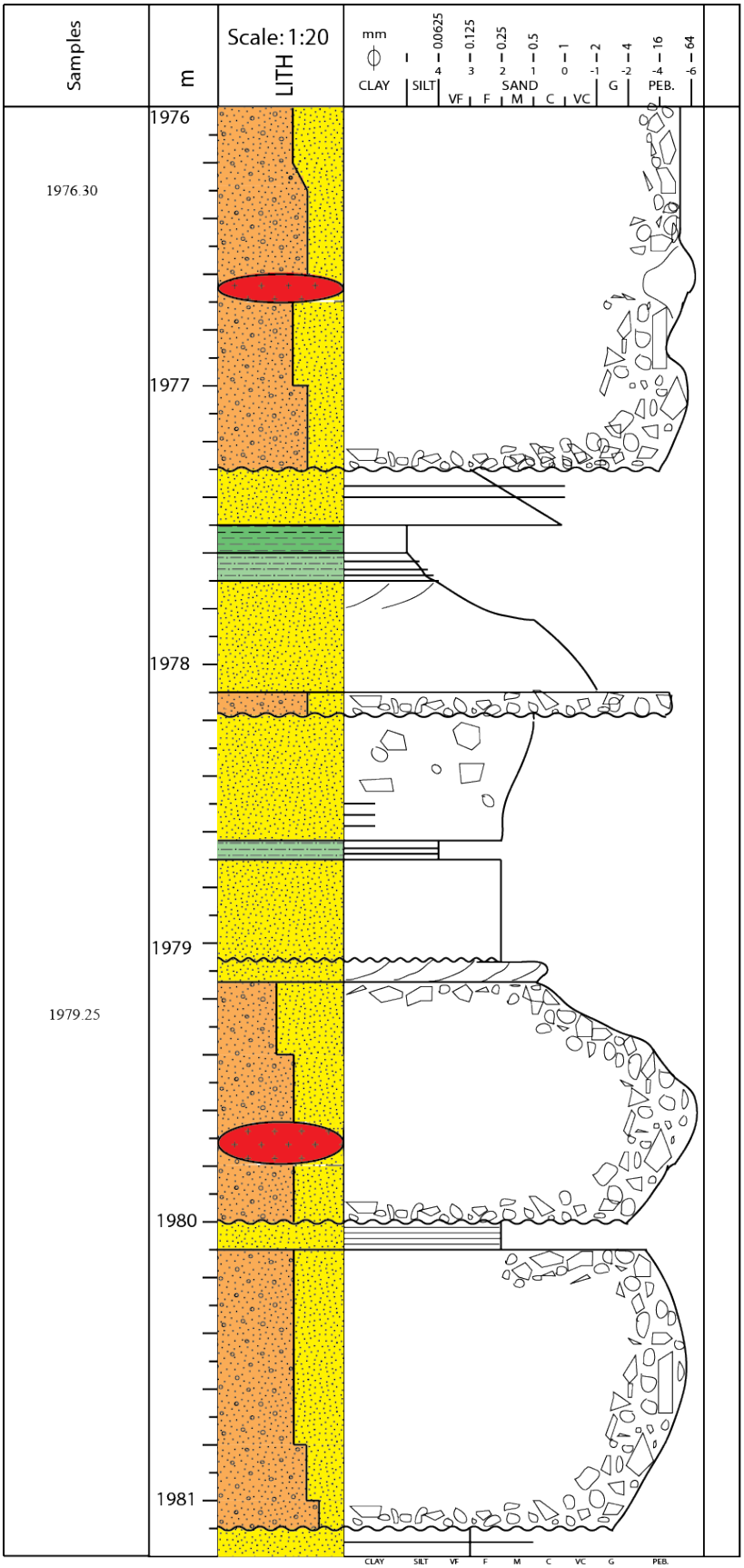

Figure 6: The sedimentological log displays the alternating layers of conglomerates, sandstones, siltstones, and claystone from FA 1. The log section represents depth level 1981.20-1976.00 m. Scale is 1:20. Samples are marked to the left.

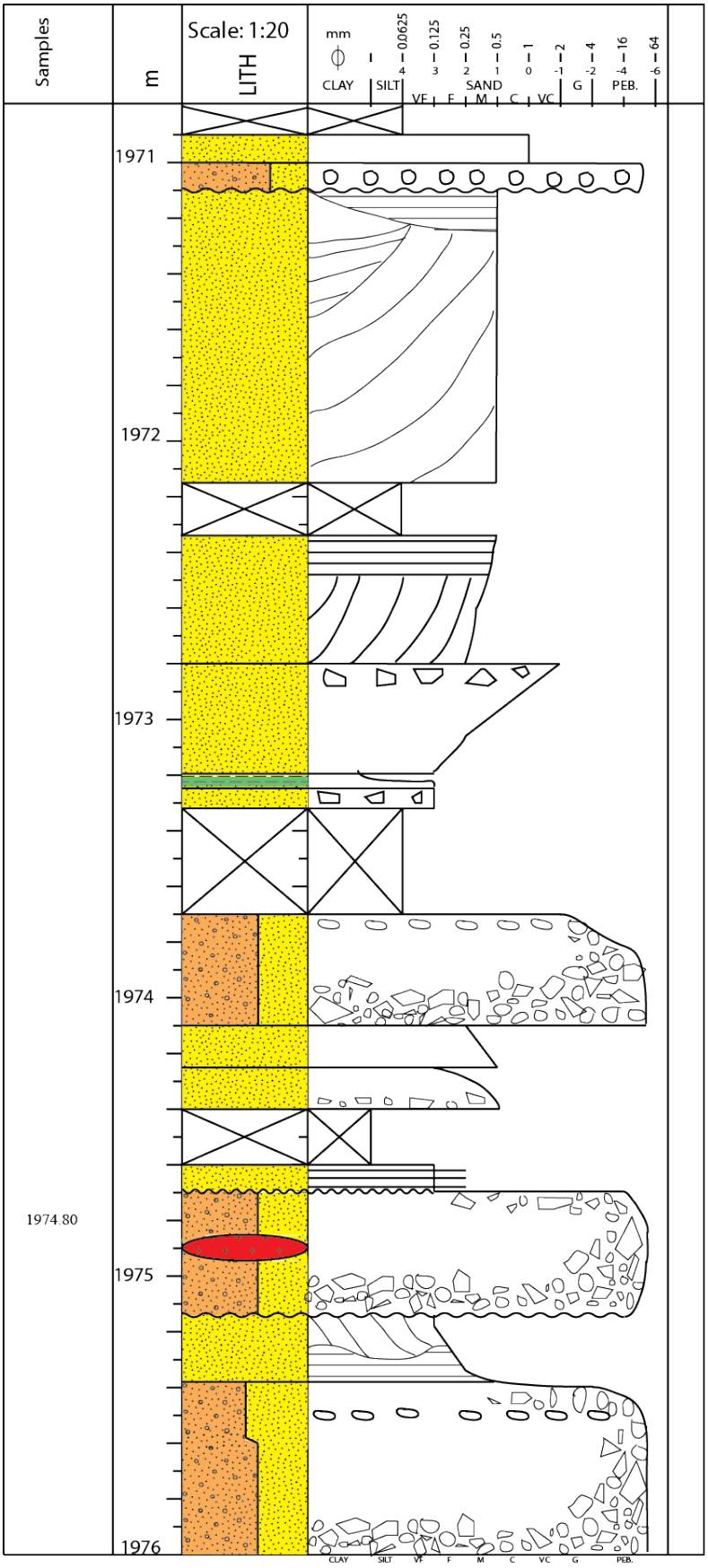

Figure 7: The sedimentological log displays the alternating layers of conglomerates, sandstones, and claystone from FA 1. The log section represents depth level 1976.00-1970.80 m. Scale is 1:20. Samples are marked to the left.

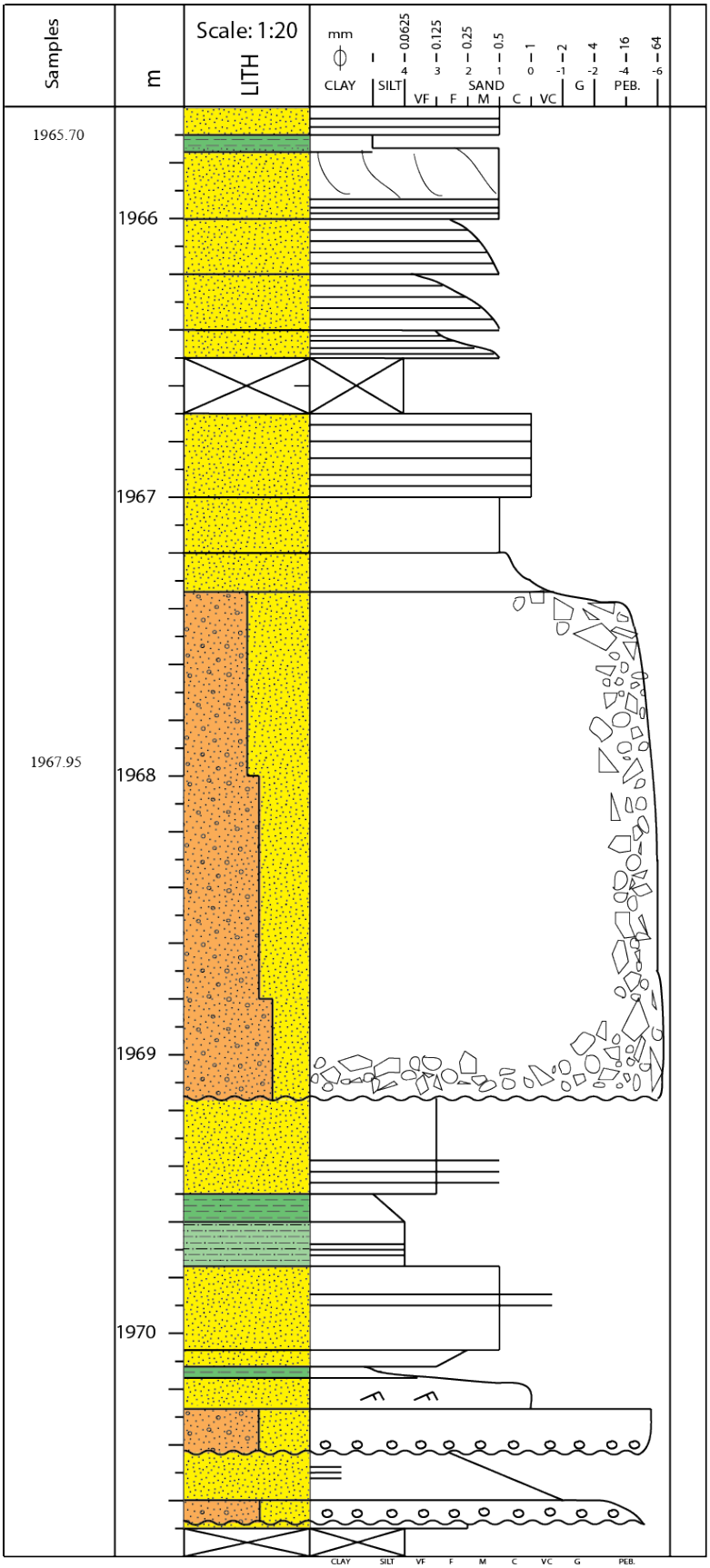

Figure 8: The sedimentological log displays the alternating layers of conglomerates, sandstones, siltstone, and claystones from FA 1. After 1967.00 m, the sandstones derive from FA 2. The log section represents depth level 1970.80-1965.60 m. Scale is 1:20. Samples are marked to the left.

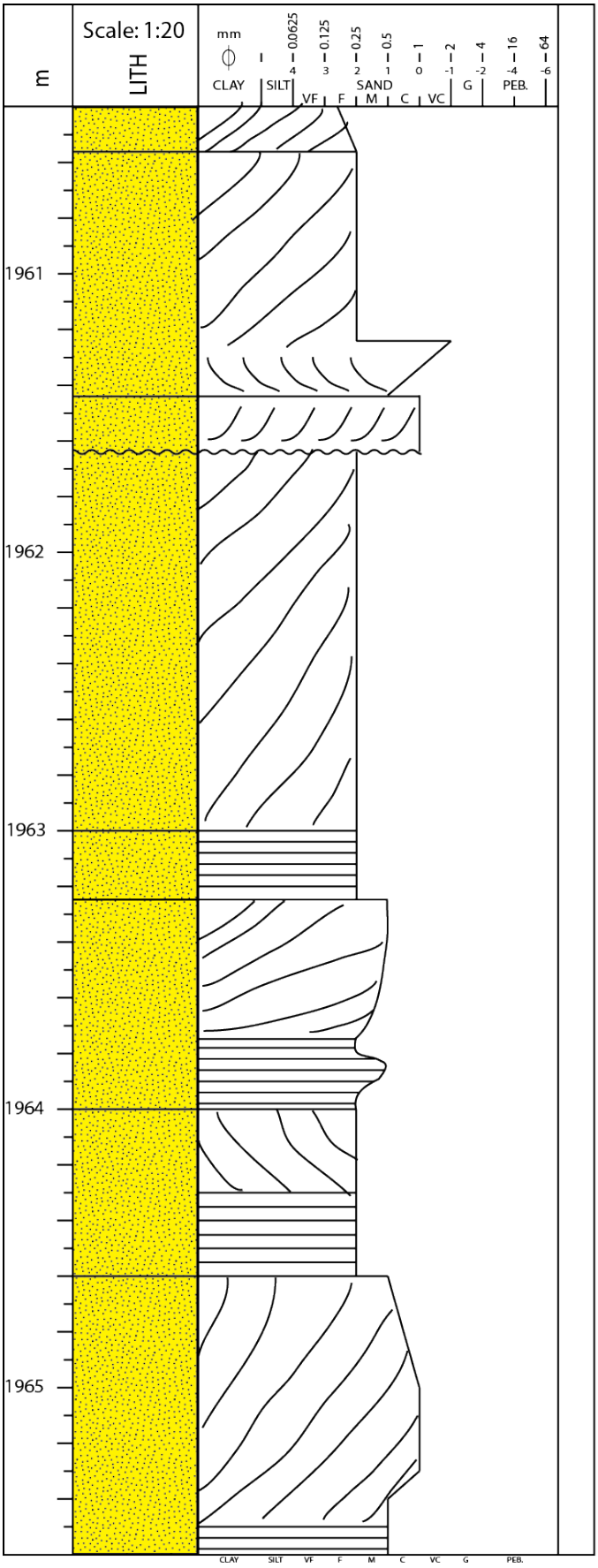

16/1-13 - page 8

Figure 9: The sedimentological log displays the sandstones from FA 2. The log section represents depth level 1965.60-1960.40 m. The scale is 1:20.

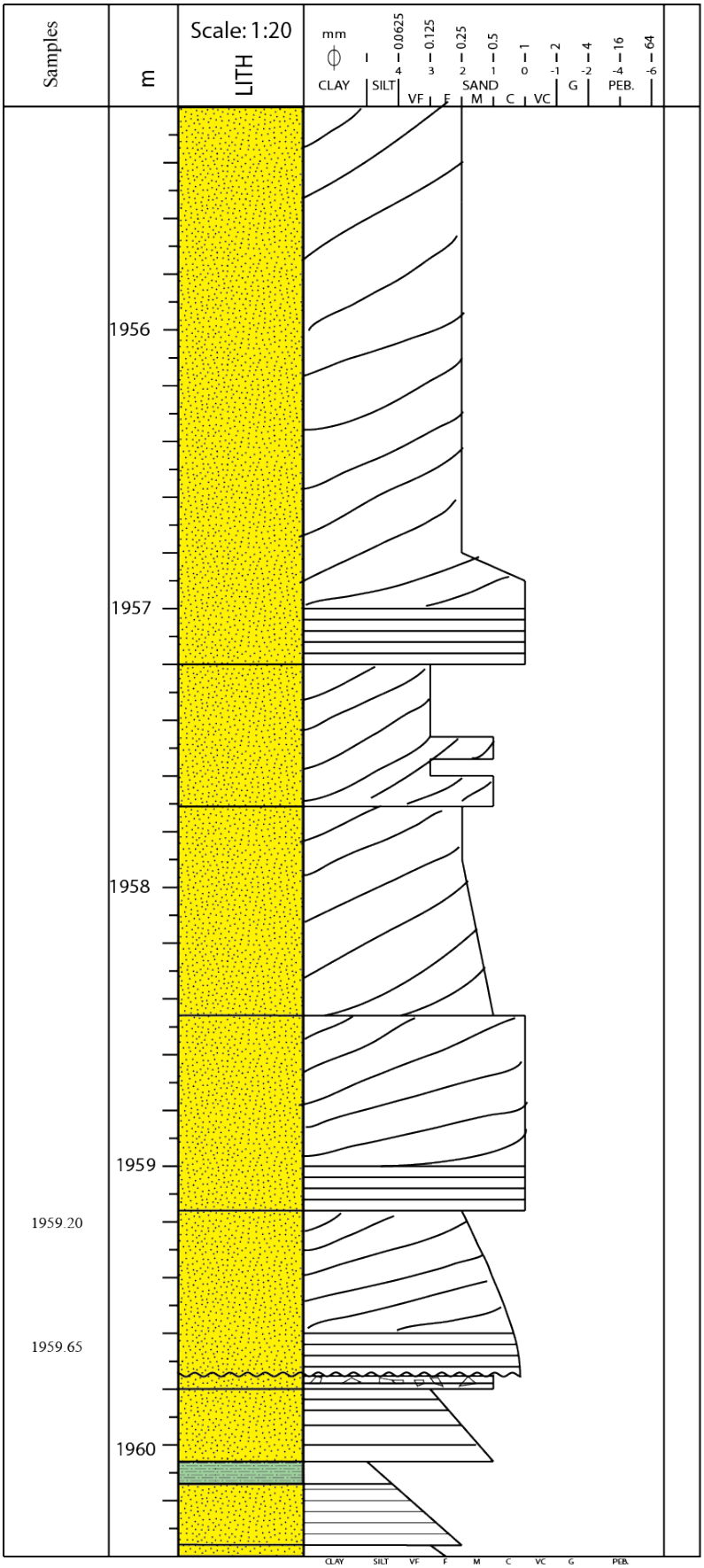

Figure 10: The sedimentological log displays the sandstones from FA 2 and a siltstone similar to facies 3. The log section represents depth level 1960.40-1955.20 m. The scale is 1:20. Samples are marked to the left.

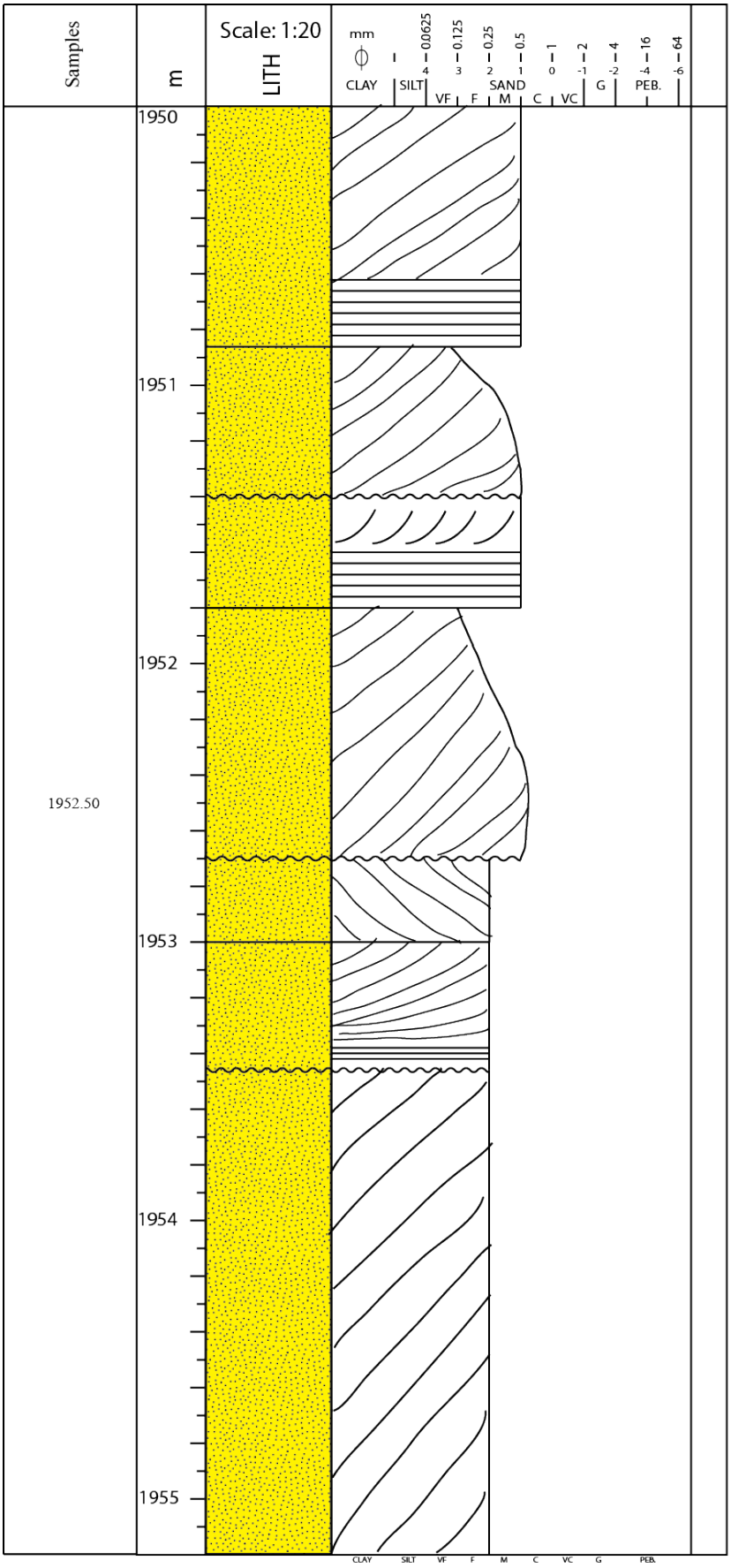

Figure 11: The sedimentological log displays the sandstones from FA 2. The log section represents depth level 1955.20-1950.00 m. The scale is 1:20. Samples are marked to the left.

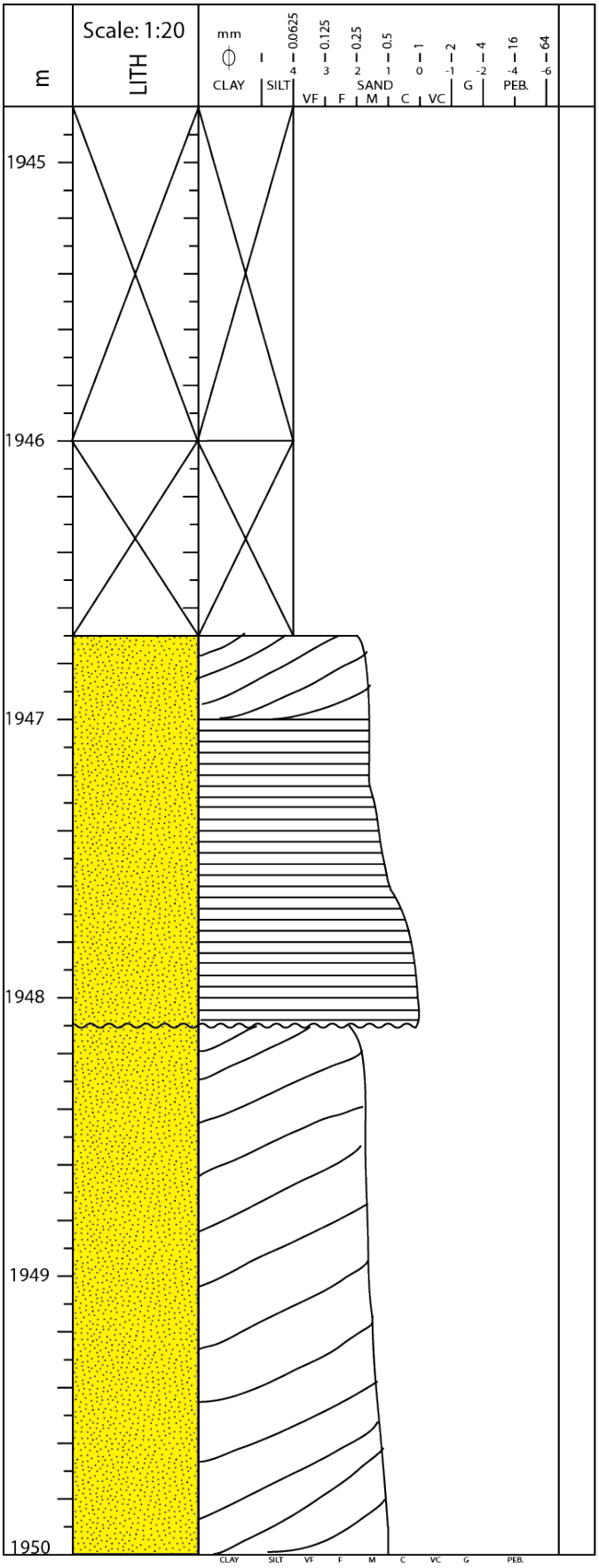

16/1-13 - page 11

Figure 12: The sedimentological log displays the sandstones from FA 2. The log section represents depth level 1950.00-1944.80 m. The scale is 1:20.

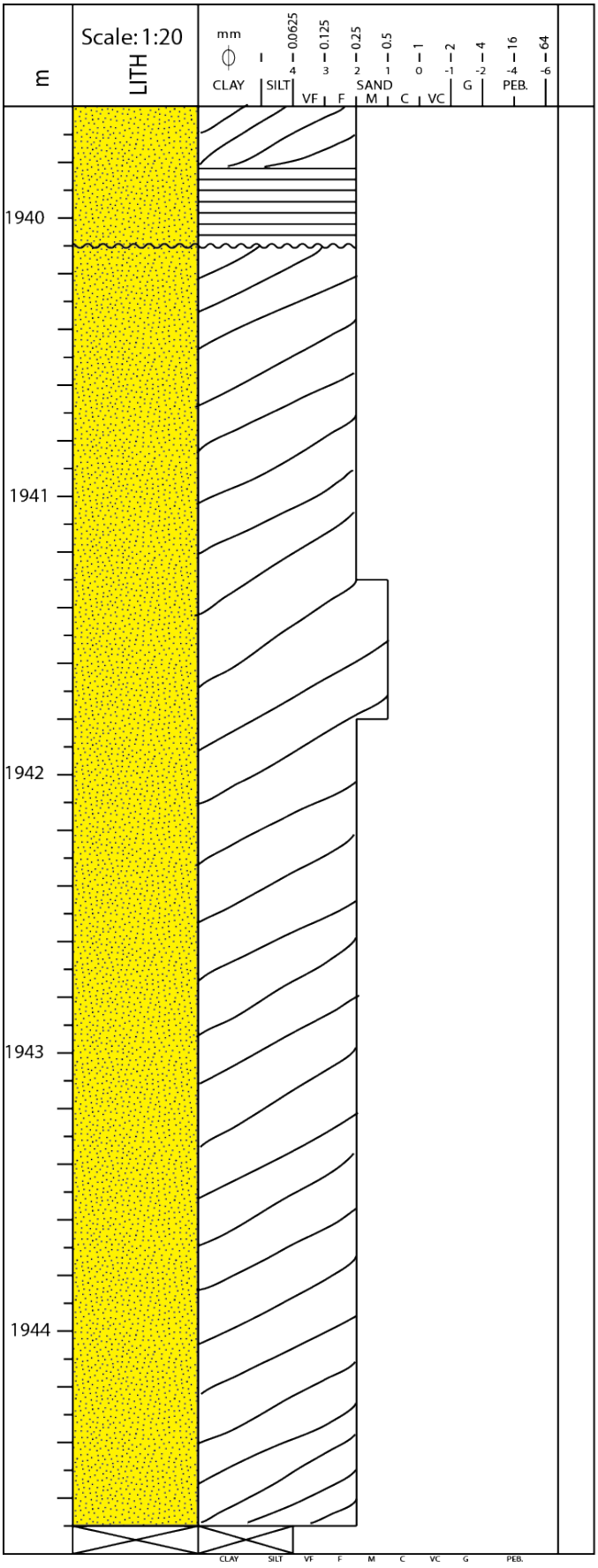

Figure 13: The sedimentological log displays the sandstones from FA 2. The log section represents depth level 1944.80-1939.60 m. The scale is 1:20.

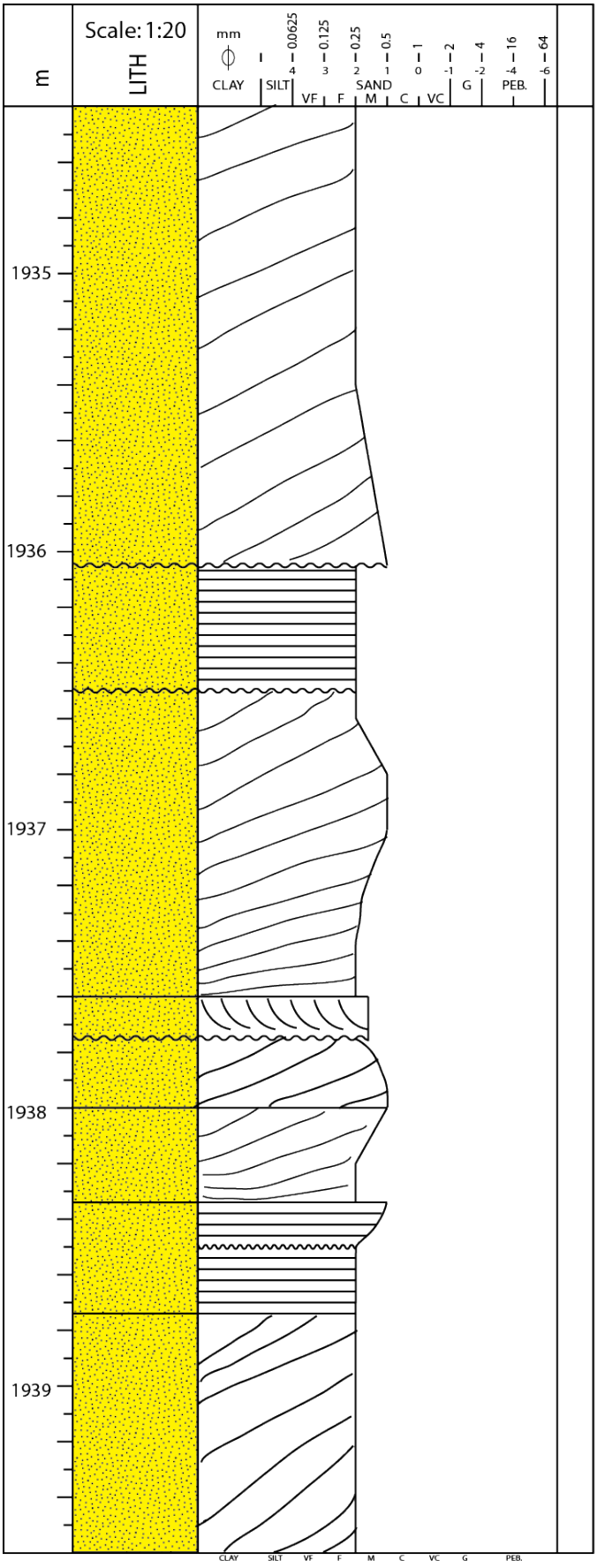

16/1-13 - page 13

Figure 14: The sedimentological log displays the sandstones from FA 2. The log section represents depth level 1939.60-1934.40 m. The scale is 1:20.

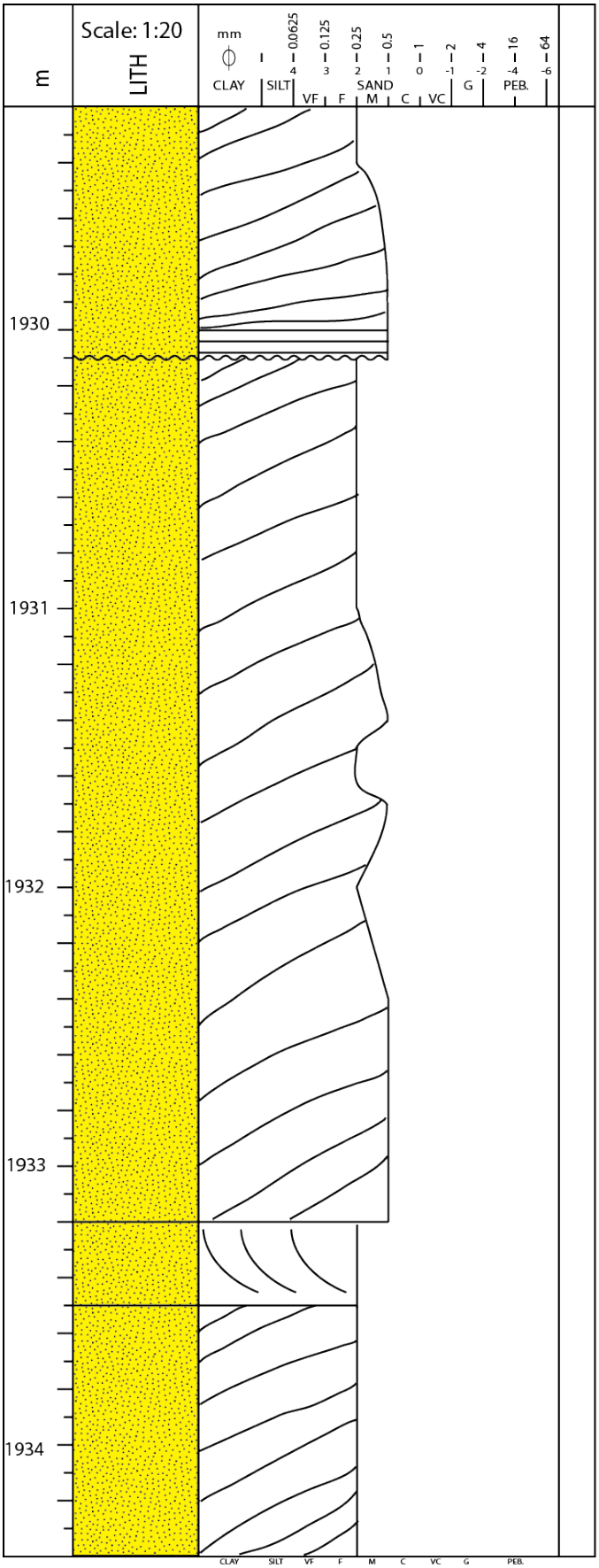

16/1-13 - page 14

Figure 15: The sedimentological log displays the sandstones from FA 2. The log section represents depth level 1934.40-1929.20 m. The scale is 1:20.

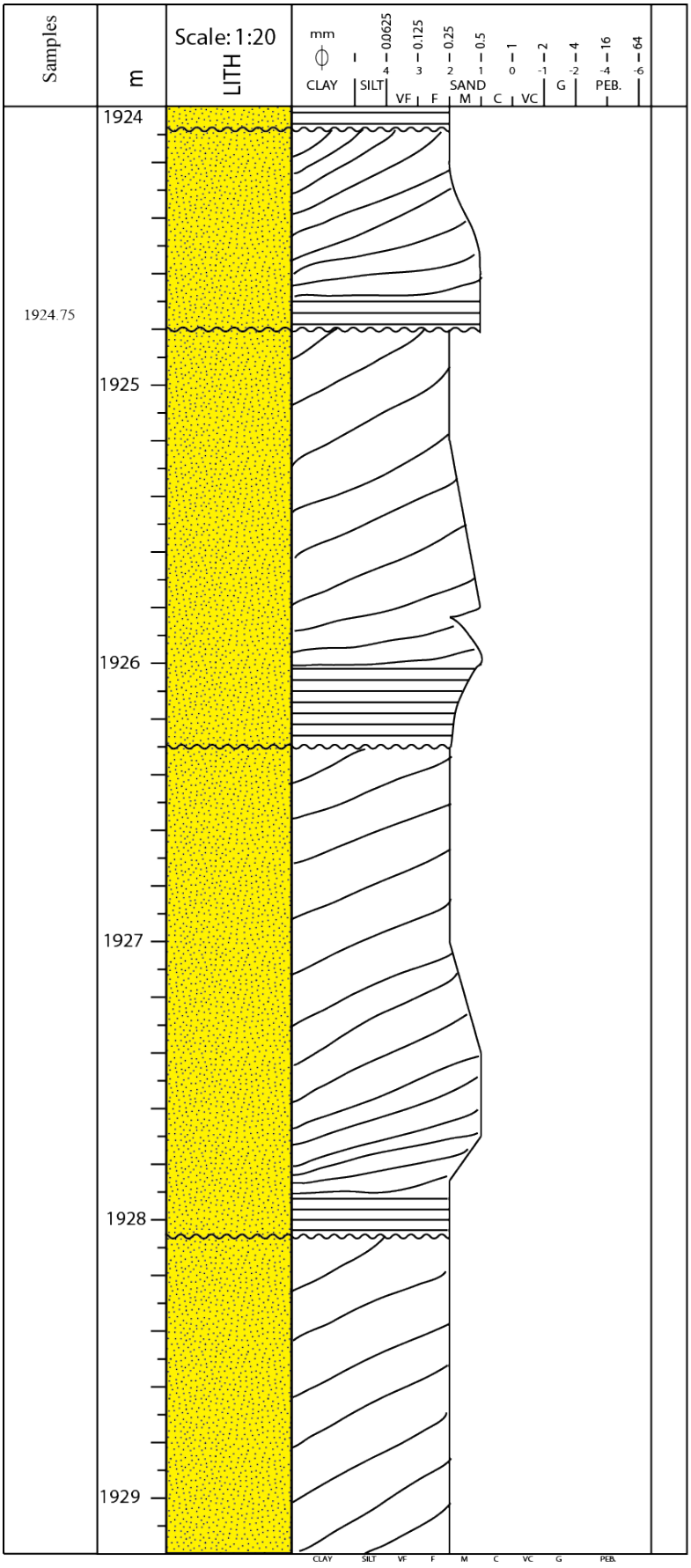

16/1-13 - page 15

Figure 16: The sedimentological log displays the sandstones from FA 2. The log section represents depth level 1929.20-1924.00 m. The scale is 1:20. Samples are marked to the left.

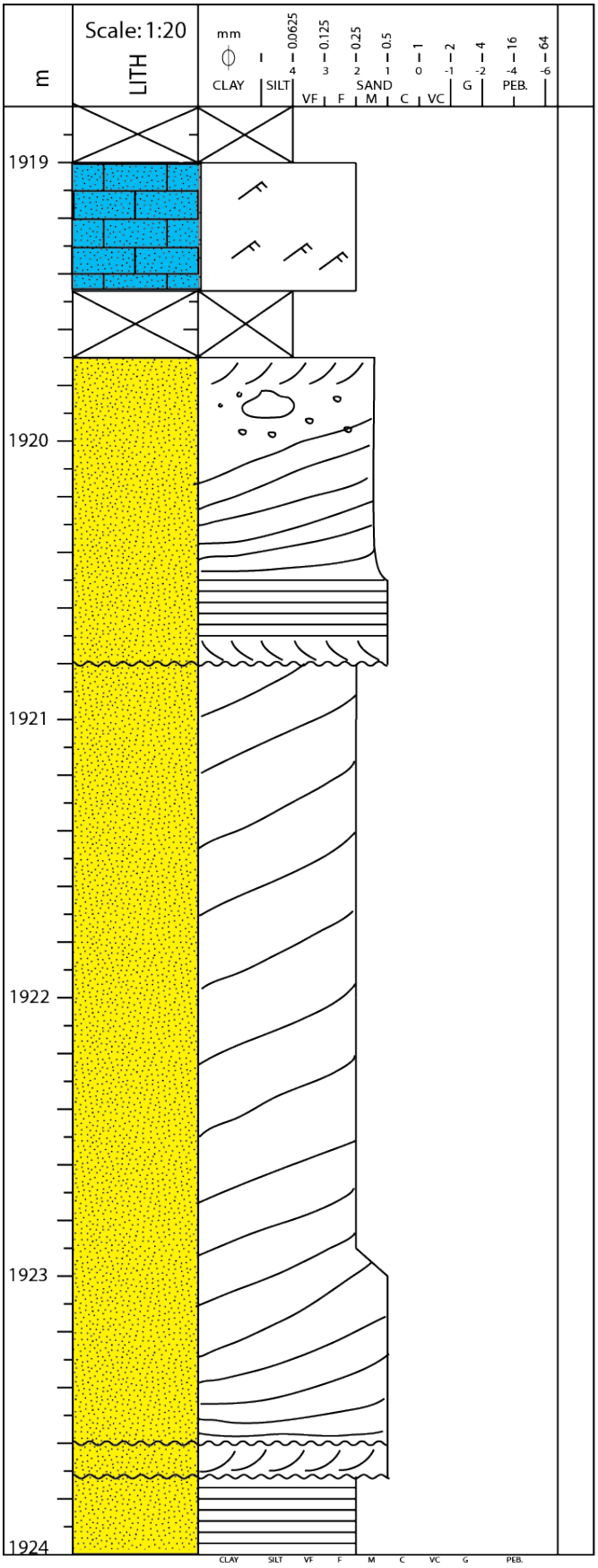

16/1-13 - page 16

Figure 17: The sedimentological log displays the sandstones from FA 2 and the calcareous sandstone from FA 3. After 1919.43 m the calcareous sandstone of FA 3 takes over. The log section represents depth level 1924.00-1918.80 m. Scale is 1:20.

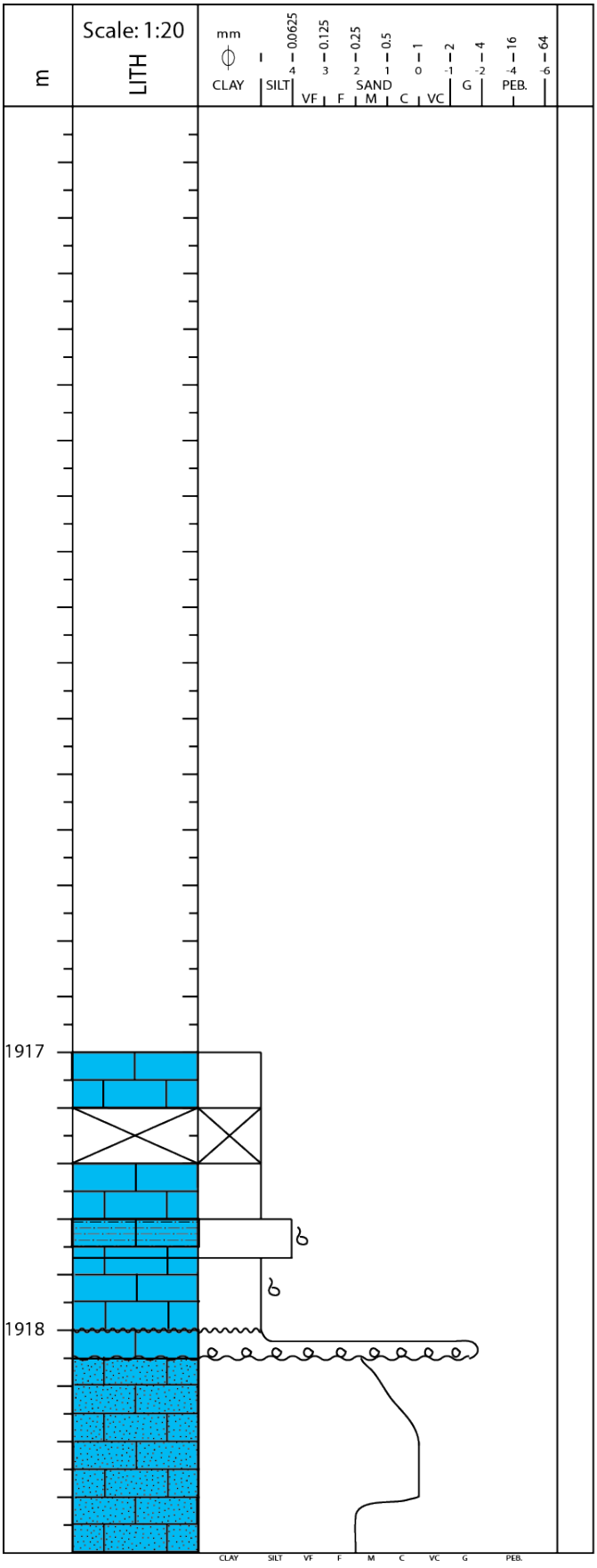

16/1-13 - page 17

Figure 18: The sedimentological log displays the calcareous sandstone, green marl, calcareous siltstone, and red marl from FA 3. The log represents depth level 1918.80-1917.00 m. Scale is 1:20.

Appendix B – Thin section description

Table 1: Thin section description of the 13 silisiclastic samples, where the most important features are described.

Facies association	Depth	Lithology	Dominating framework configuration	Predominant structures	Average grain size (mm)	Most common grain shape	Sorting	Remarks
FA1	1998.30	Conglomerate	Grain supported	Heterogenic	Very coarse → coarse sand	Angular → sub-rounded	Poor	Better sorted in areas of Fe-oxides. Phase 2 Fe-oxides. Large rock fragments, reduces sorting and increase grain size.
FA 1	1994.90	Sandstone	Grain Supported	No structure	Medium sand	Angular → sub-rounded	Moderate	Varied degree of feldspar preservation. Plagioclase highest alteration. Clastic micas observed. Clay minerals reduce poro/perm.
FA1	1995.65	Conglomerate	Grain supported	Heterogenic	Coarse sand	Angular → sub-angular	Poor	Clay and carbonate cement decreases poro/perm.
FA1	1983.40	Sandstone	Grain supported	No structure	Medium → fine sand	Sub-angular	Very good → good	Zones of higher clay content. Good poro/perm.
FA1	1983.20	Conglomerate	Grain supported	Heterogenic	Very coarse → coarse sand	Angular → sub-rounded	Poor	High abundance of rock fragments. Presence of clastic mica. 2 Fe-oxide phases.
FA1	1982.90	Conglomerate	Grain supported	Heterogenic	Very coarse → coarse sand	Angular → sub-rounded	Very poor	Large amount of rock fragments, increases grain size.
FA1	1979.25	Conglomerate	Grain supported	Heterogenic	Coarse →	Sub-	Poor	High content of clay and

					medium sand	angular → sub-rounded		carbonate cement, reduces poro/perm.
FA1	1974.80	Conglomerate	Grain supported	Heterogenic	Coarse sand	Angular → Sub-rounded	Poor	Clay and carbonate cement reduces poro/perm.
FA1	1967.95	Conglomerate	Grain supported	Heterogenic	Medium sand	Angular → sub-rounded	Poor	Largest grains are rock fragments. Pore filling clay reduces poro/perm.
FA 2	1959.65	Sandstone	Grain supported	UC units	Medium → fine sand	Sub-angular → sub-rounded	Moderate	High content of clay, reduces poro/perm
FA 2	1959.20	Sandstone	Grain supported	No structure	Fine sand	Sub-angular → sub-rounded	Very good	Good poro/perm. Low clay content. Highest content of carbonate cement, considering the sandstones. High amount of polycrystalline quartz fragments.
FA 2	1952.50	Sandstone	Grain supported	UC units	Medium → fine sand	Sub-angular	Moderate → good	High content of clay, reduces poro/perm. Low plagioclase content.
FA 2	1924.75	Sandstone	Grain supported	UC units	Medium sand	Sub-angular → sub-rounded	Moderate	High amount of polycrystalline quartz fragments

Table 2: Thin section description of the eight basement samples. The most important features are described.

Basement clast	Depth	Classification	Weathering class	Remarks
Clast 1	2000.85	Granite	2	Secondary porosity due to dissolved feldspars. Feldspar preservation: category II for both. Myrmekite. Phenocrystals ranging between 0.25-2.0 mm.
Clast 2	2000.30	Granite	3	Secondary porosity due to dissolved feldspar and fracture. Degraded biotite. Feldspar preservation: category II for plagioclase and I for K-feldspar. Phenocrystals ranging between 0.25-1 mm.
Clast 4	1999.45	Quartz monzonite	2	High content of chlorite. Feldspar preservation: category IV for plagioclase and II for K-feldspar. Secondary porosity. Myrmekite. Phenocrystals ranging between 0.25-2.0 mm.
Clast 5	1996.60	Granite	2	Secondary porosity. Feldspar preservation: category II for both. Dissolved muscovite. Phenocrystals have an average size of 1 mm.
Clast 6	1995.40	Granodiorite	2	Low K-feldspar content. Feldspar preservation: category III for plagioclase and category I for K-feldspar. Very low porosity, secondary origin due to dissolved feldspar. Myrmekite. Phenocrystals ranging between 0.25-2 mm.
Clast 9b	1994.90	Granite	3	Visual signs of weathering. Nearly all phenocrystals show sign of alteration. All plagioclase crystals altered. Increased clay content towards the edge of clast. Phenocrystals ranging between 2-3 mm.
Clast 8	1991.55	Granodiorite	4	Biotite and clay rich, heavily weathered. Secondary porosity, linked to dissolved feldspar. Feldspar preservation: category V for both. Phenocrystals ranging between 1.1-1.3 mm.
Clast 9a	1976.30	Granite	3	No visible signs of weathering. Feldspar preservation: category II for both, but high in III and IV as well. Sericitzation. Low porosity. Relative high clay content. Phenocrystals ranging between 2.53-4.39 mm.

Appendix C – Point counting results

Table 3: Results obtained from point counting for the chosen samples from core 16/1-13. Mono q= monocrystalline quartz. Poly q = polycrystalline quartz. RF = rock fragments. Overg = overgrowth. Carb. cement = carbonate cement.

Sample	Depth	Mono q	Poly q	K-spar	Plag.	Poro.	RF	Overgr.	Carb. cement	Clay	Fe-oxide	Chlorite	Biotite	Muscovite/illite
Clast 1	2000.85	20 %	12 %	30 %	30 %	1 %	0 %	0 %	2 %	0 %	1 %	2 %	2 %	0 %
Clast 2	2000.30	19 %	10 %	17 %	34 %	2 %	0 %	0 %	5 %	2 %	1 %	1 %	9 %	1 %
Clast 4	1999.45	3 %	2 %	38 %	33 %	1 %	0 %	0 %	0 %	1 %	0 %	17 %	0 %	5 %
Clast 5	1996.60	19 %	17 %	23 %	35 %	2 %	0 %	0 %	3 %	0 %	1 %	0 %	0 %	1 %
Grey matrix	1995.65	19 %	14 %	11 %	11 %	2 %	18 %	0 %	9 %	15 %	0 %	0 %	2 %	1 %
Clast 6	1995.40	17 %	25 %	8 %	31 %	0 %	0 %	0 %	2 %	0 %	1 %	0 %	2 %	16 %
Clast 8	1991.55	15 %	13 %	3 %	17 %	2 %	0 %	0 %	1 %	30 %	0 %	0 %	19 %	0 %
Sandstone	1983.40	41 %	22 %	5 %	7 %	10 %	0 %	0 %	7 %	6 %	0 %	0 %	2 %	0 %
Red matrix	1982.90	14 %	17 %	6 %	8 %	4 %	23 %	0 %	7 %	13 %	7 %	0 %	1 %	1 %
Green matrix	1979.25	23 %	16 %	12 %	11 %	4 %	9 %	1 %	6 %	15 %	0 %	0 %	2 %	1 %
Clast 9	1976.30	26 %	9 %	20 %	29 %	0 %	0 %	0 %	3 %	11 %	0 %	1 %	3 %	0 %
Medium sandstone	1959.65	23 %	26 %	9 %	5 %	9 %	0 %	0 %	9 %	16 %	0 %	0 %	1 %	2 %
Fine sandstone	1959.20	33 %	26 %	5 %	3 %	19 %	0 %	1 %	11 %	3 %	1 %	0 %	0 %	0 %

Table 4: The Table presents the percentage distribution of plagioclase preservation in the in the representative categories from Table 2.3. The results were obtained during point counting on samples from core 16/1-13.

Plagioclase preservation	I	II	III	IV	V
2000.85	6 %	42 %	40 %	13 %	0 %
2000.30	3 %	44 %	24 %	27 %	2 %
1999.45	4 %	35 %	32 %	29 %	0 %
1996.60	9 %	64 %	23 %	4 %	0 %
1995.65	18 %	30 %	18 %	25 %	9 %
1995.40	0 %	44 %	49 %	7 %	0 %
1991.55	0 %	4 %	15 %	22 %	58 %
1983.40	20 %	40 %	40 %	0 %	0 %
1982.90	12 %	15 %	27 %	27 %	18 %
1979.25	11 %	20 %	11 %	16 %	41 %
1976.30	0 %	41 %	27 %	33 %	0 %
1959.65	5 %	37 %	11 %	5 %	42 %
1959.20	0 %	90 %	10 %	0 %	0 %

Table 5: The Table presents the percentage distribution of K-feldspar preservation in the in the representative categories from Table 2.3. The results were obtained during point counting on samples from core 16/1-13.

K-feldspar preservation	I	II	III	IV	V
2000.85	32 %	45 %	22 %	0 %	0 %
2000.30	44 %	29 %	12 %	15 %	0 %
1999.45	38 %	56 %	5 %	0 %	0 %
1996.60	30 %	57 %	12 %	0 %	0 %
1995.65	62 %	27 %	11 %	0 %	0 %
1995.40	37 %	27 %	33 %	3 %	0 %
1991.55	23 %	0 %	0 %	38 %	38 %
1983.40	69 %	28 %	3 %	0 %	0 %
1982.90	24 %	52 %	16 %	0 %	8 %
1979.25	56 %	25 %	8 %	6 %	4 %
1976.30	22 %	56 %	8 %	15 %	0 %
1959.65	49 %	27 %	24 %	0 %	0 %
1959.20	37 %	63 %	0 %	0 %	0 %

Table 6: The percentage distribution of of primary and secondary porosity observed during point counting on samples from core 16/1-13.

Porosity	Primary	Secondary
2000.85	0 %	100 %
2000.30	0 %	100 %
1999.45	0 %	100 %
1996.60	0 %	100 %
1995.65	89 %	11 %
1995.40	N/A	
1991.55	0 %	100 %
1983.40	100 %	0 %
1982.90	86 %	14 %
1979.25	100 %	0 %
1976.30	N/A	
1959.65	94 %	6 %
1959.20	97 %	3 %

Table 7: The percentage distribution of minerals found in the rock fragments during point counting on samples from core 16/1-13.

Rock fragments	Plagioclase	K-feldspar	Mono-quartz	Poly-quartz	Mica
1995.65	29 %	21 %	17 %	31 %	0 %
1983.40	N/A				
1982.90	34 %	29 %	14 %	19 %	3 %
1979.25	22 %	24 %	16 %	19 %	19 %
1959.65			100 %		
1959.20				100 %	

Table 8: The percentage distribution of overgrowth types observed during point counting on samples from core 16/1-13.

Overgrowth	Quartz	Feldspar	Fe-oxides
1995.65	100 %		
1983.40	100 %		
1982.90		100 %	
1979.25	50 %	50 %	
1959.65		100 %	
1959.20			100 %

Table 9: The percentage distribution of polycrystalline rock fragments observed in the sediments from core 16/1-13 during point counting.

Poly-quartz fragments	Percentage
1995.65	1 %
1983.40	N/A
1982.90	11 %
1979.25	2 %
1959.65	12 %
1959.20	13 %

Appendix D: XRD bulk results

Table 10: Bulk XRD results from the samples from core 16/1-13.

Sample	% Quartz	% Plagioclase	% K-feldspar	% Chlorite	% Kaolinite	% Biotite	% Muscovite/illite	% Hematite	% Calcite	% Sylvite	% Halite	Quartz/total feldspar
2000.85	28,67	38,54	21,02	2,586	2,72	1,57	2,85	0,15	1,88	0,00	0,00	
2000.30	20,10	54,73	11,71	2,64	1,90	6,22	2,45	0,14	0,11	0,00	0,00	
1999.45	6,66	52,13	29,70	5,43	0,00	1,57	2,92	1,06	0,53	0,00	0,00	
1996.60	30,24	33,75	30,03	0,00	0,00	0,60	5,02	0,13	0,24	0,00	0,00	
1995.65	30,37	31,49	23,96	0,00	4,39	4,13	3,62	0,37	1,67	0,00	0,00	0,55
1995.40	22,22	54,81	10,26	2,51	3,29	2,57	4,06	0,29	0,00	0,00	0,00	
1991.55	30,79	16,00	26,49	5,58	6,08	8,15	1,97	0,09	4,67	0,00	0,00	
1983.40	64,57	6,16	15,58	1,57	1,29	0,62	2,16	0,00	7,91	0,13	0,00	2,97
1982.90	31,04	27,23	24,17	3,16	4,05	1,39	4,86	0,56	3,46	0,00	0,09	0,60
1979.25	34,16	21,66	26,73	2,18	3,89	1,96	5,28	0,82	3,32	0,00	0,00	0,71
1974.80	30,23	16,67	28,78	2,22	4,89	2,24	5,47	0,41	9,09	0,00	0,00	0,67
1967.95	37,00	24,95	20,01	2,18	7,28	2,42	2,82	0,00	3,34	0,00	0,00	0,82
1965.70	42,35	2,00	25,95	1,58	5,05	2,51	16,09	0,00	3,41	0,00	1,06	1.52
1959.65	50,35	2,72	24,25	1,18	10,81	1,53	2,50	0,00	6,09	0,18	0,40	1,87
1959.20	69,67	1,46	13,70	0,00	4,18	0,65	1,75	0,00	8,18	0,21	0,20	4,60
1952.50	70,16	2,59	11,88	1,93	6,42	1,05	2,87	0,00	2,88	0,24	0,00	4,85
1924.75	70,23	1,18	17,23	1,21	5,01	0,85	1,44	0,00	2,48	0,37	0,00	3,81

Table 11: The average XRD% values found for the three matrix samples individually from the alluvial fan, and an average XRD% value found for the matrixes combined. Qtz = quartz. Plag = plagioclase. K-spr = K-feldspar. Chl = chlorite. Kao = kaolinite. Bio = biotite. Musco/ill = muscovite/illite. Hema = hematite. Cal = calcite.

Average XRD% values for the matrix samples	Qtz	Plag	K-spr	Chl	Kao	Bio	Musco/ill	Hema	Cal
Grey	34	28	22	1	6	3	3	0	3
Red	31	27	24	3	4	1	5	0	3
Green	32	19	28	2	9	2	5	0	6
Average matrix	32	25	25	2	6	2	4	0	4

Appendix E: EMP results

Table 12: EMP results from selected samples from core 16/1-13 and 16/1-15. Samples 1967.95, 1995.65, 1924.75 and 1983.40 represent samples from 16/1-13, while sample 1974.35 represent basement from core 16/1-15.

DataSet/Point	Sample	SiO2	Na2O	Al2O3	K2O	CaO	FeO	MnO	BaO	Total
1 / 1 .	1967.95	62,50	0,55	18,67	16,43	-0,13	-0,33	0,01	0,46	98,15
2 / 1 .	1967.95	64,62	0,85	18,64	15,68	-0,13	0,01	-0,04	0,42	100,04
3 / 1 .	1967.95	64,17	0,90	18,61	15,58	-0,08	0,04	0,01	0,41	99,65
4 / 1 .	1967.95	65,03	1,07	18,77	15,60	-0,04	0,10	0,00	0,39	100,91
5 / 1 .	1967.95	64,75	0,02	18,51	16,99	-0,02	-0,01	-0,01	0,08	100,31
6 / 1 .	1967.95	65,15	0,07	18,93	16,95	-0,07	0,02	0,03	0,02	101,10
7 / 1 .	1967.95	64,57	0,92	18,66	15,95	-0,04	0,02	0,05	0,04	100,17
8 / 1 .	1967.95	64,86	0,99	18,76	15,69	0,02	0,06	-0,02	0,41	100,77
9 / 1 .	1967.95	64,79	0,03	18,53	17,40	-0,10	0,04	-0,06	0,01	100,65
10 / 1 .	1967.95	64,14	1,05	18,40	15,10	-0,04	0,03	0,01	0,65	99,35
11 / 1 .	1967.95	64,23	1,37	18,68	14,96	-0,01	0,03	0,00	0,38	99,63
12 / 1 .	1967.95	65,45	0,69	18,50	16,21	-0,01	-0,01	0,07	-0,04	100,86
13 / 1 .	1967.95	64,73	0,92	18,61	15,74	-0,07	0,02	-0,01	0,25	100,20
14 / 1 .	1967.95	64,78	0,88	18,61	15,90	0,01	0,04	-0,03	-0,04	100,16
15 / 1 .	1967.95	64,35	1,15	18,73	14,89	-0,09	0,04	0,00	1,40	100,46
16 / 1 .	1967.95	63,73	1,07	18,79	14,73	-0,05	0,01	0,01	1,71	100,00
17 / 1 .	1967.95	64,86	0,74	18,48	16,10	-0,05	0,11	-0,02	0,31	100,53
18 / 1 .	1995.65	65,38	0,85	18,70	15,89	-0,11	0,06	-0,03	0,15	100,90
19 / 1 .	1995.65	64,90	0,82	19,01	15,66	0,01	0,02	0,00	0,57	101,00
20 / 1 .	1995.65	63,94	0,93	18,55	15,31	-0,03	0,02	-0,03	0,87	99,56
21 / 1 .	1995.65	64,47	0,81	18,76	15,53	-0,06	0,08	0,01	0,93	100,54
22 / 1 .	1995.65	65,25	0,80	18,70	15,91	-0,05	0,09	0,00	0,24	100,94
23 / 1 .	1995.65	65,48	1,17	19,11	15,10	-0,03	0,11	-0,02	0,78	101,70
24 / 1 .	1995.65	65,09	0,04	18,65	17,13	-0,08	0,05	0,01	-0,03	100,86
25 / 1 .	1995.65	64,23	0,62	18,76	15,92	-0,05	0,02	-0,05	0,81	100,25
26 / 1 .	1995.65	65,12	0,78	18,49	16,04	-0,08	0,05	0,04	0,12	100,56
27 / 1 .	1995.65	64,17	0,90	18,22	15,67	0,06	0,01	-0,01	0,30	99,33

28 / 1 .	1995.65	64,52	1,27	18,74	14,94	-0,03	0,06	0,00	1,07	100,56
29 / 1 .	1995.65	65,11	1,09	18,68	15,66	-0,02	0,04	0,04	0,20	100,80
30 / 1 .	1995.65	64,56	1,24	18,92	15,03	-0,01	0,03	-0,01	0,82	100,56
31 / 1 .	1995.65	65,06	0,91	18,84	15,72	-0,01	0,07	-0,02	0,27	100,84
32 / 1 .	1995.65	64,14	1,19	18,68	14,86	-0,03	0,08	-0,07	0,74	99,59
33 / 1 .	1995.65	64,33	1,63	18,60	14,70	-0,01	0,08	0,01	0,74	100,09
34 / 1 .	1995.65	64,51	0,09	18,42	16,71	-0,02	-0,03	0,00	-0,03	99,64
35 / 1 .	1924.75	63,99	0,97	18,39	15,31	0,01	0,02	0,01	0,55	99,25
36 / 1 .	1924.75	64,97	0,47	18,65	16,50	-0,12	0,02	0,07	0,12	100,67
37 / 1 .	1924.75	64,70	0,07	18,15	17,13	-0,04	0,08	0,02	0,00	100,10
38 / 1 .	1924.75	64,78	1,04	18,30	15,31	-0,06	0,03	0,02	0,16	99,58
39 / 1 .	1924.75	64,91	0,70	18,55	16,02	-0,09	0,03	-0,02	0,35	100,46
40 / 1 .	1924.75	64,86	0,02	18,25	17,01	-0,08	0,04	0,03	-0,04	100,08
41 / 1 .	1924.75	64,18	0,83	18,23	15,82	-0,04	0,06	-0,01	0,22	99,29
42 / 1 .	1924.75	65,20	0,36	18,34	16,69	-0,12	0,10	0,02	0,08	100,68
43 / 1 .	1924.75	64,76	1,08	18,96	15,65	-0,09	0,02	-0,06	0,25	100,58
44 / 1 .	1924.75	65,25	0,44	18,62	16,59	-0,04	0,00	0,01	0,60	101,48
45 / 1 .	1924.75	65,25	0,92	18,80	15,82	-0,07	-0,01	-0,01	0,36	101,06
46 / 1 .	1983.40	64,21	0,84	18,40	15,58	0,03	0,06	0,01	0,68	99,81
47 / 1 .	1983.40	64,64	0,05	17,98	16,95	-0,03	0,00	-0,01	0,01	99,59
48 / 1 .	1983.40	64,47	1,56	18,52	14,63	-0,02	0,00	-0,04	0,42	99,54
49 / 1 .	1983.40	64,96	0,75	18,26	15,63	-0,06	0,08	-0,02	0,28	99,89
50 / 1 .	1983.40	63,10	0,99	19,11	14,58	-0,05	0,00	0,02	2,16	99,89
51 / 1 .	1983.40	64,76	0,50	18,27	16,19	-0,15	0,07	0,04	0,21	99,90
52 / 1 .	1983.40	64,31	1,30	18,50	14,95	-0,06	0,04	-0,03	0,27	99,27
53 / 1 .	1974.35	65,15	1,08	18,56	15,32	0,00	0,11	0,03	0,44	100,69
54 / 1 .	1974.35	65,45	0,77	18,33	16,09	-0,05	0,10	0,02	0,08	100,77
55 / 1 .	1974.35	63,06	0,73	19,24	14,92	-0,08	0,19	-0,03	2,66	100,70
56 / 1 .	1974.35	64,20	1,02	18,38	15,31	-0,04	0,08	0,04	0,37	99,36